Lars Erik Walle

Surface science studies of TiO_2 single crystal systems

Thesis for the degree of Philosophiae Doctor

Trondheim, December 2009

Norwegian University of Science and Technology
Faculty of Natural Sciences and Technology
Department of Physics

NTNU
Norwegian University of
Science and Technology

NTNU
Norwegian University of Science and Technology

Thesis for the degree of Philosophiae Doctor

Faculty of Natural Sciences and Technology
Department of Physics

ISBN 978-82-471-1887-0 (printed ver.)
ISBN 978-82-471-1888-7 (electronic ver.)
ISSN 1503-8181

Doctoral theses at NTNU, 2009:239

Printed by NTNU-trykk

Abstract

Titanium dioxide is a material finding applications in variety of areas, including catalysis, photocatalysis, photovoltaics, energy storage, gas sensors and biocompatible materials. As a consequence, this material has been the target of numerous scientific studies over the last years. Due to its availability the rutile polymorph of TiO_2 has become the benchmark surface for fundamental studies of metal oxide surface chemistry and the majority of experimental studies have been performed on this phase. The emergence of nanoscience has shifted the focus towards the anatase polymorph since this phase is preferred when forming TiO_2 nanoparticles and applied systems almost exclusively comprise anatase TiO_2 nanostructures. In this thesis synchrotron based high resolution photoelectron spectroscopy (PES) in combination with X-ray absorption spectroscopy (XAS) has been utilized to study how clean TiO_2 single crystal surfaces interact with molecular and metallic adsorbates and formation of TiO_2 films on a metal surface.

O 1s XAS in conjunction with PES was used to explore the conduction-band edge of single crystalline and nanostructured anatase TiO_2. In the O 1s XAS process pure Ti *d* states cannot be probed due to selection rules. By appropriate energy referencing, the separation between the Ti *d* derived conduction-band edge and the threshold of the unoccupied Ti *d*-O *p* states was revealed. Also, 4% of an electronic charge per Ti ion was found to be sufficient to change the character of the empty states at threshold from pure Ti *d* to Ti *d*-O *p*, in good agreement with theoretical values.

By using highly surface sensitive PES, water adsorption on the rutile $TiO_2(110)$ and anatase $TiO_2(101)$ and (001) surfaces was investigated. For all three surfaces the formation of a water monolayer involving both associative and dissociative adsorption was demonstrated. Reducing the coverage by heating the monolayer resulted in an increased OH:H_2O ratio. For the rutile $TiO_2(110)$ surface, without oxygen vacancies, neither OH nor H_2O originating from the monolayer could be detected at room temperature, indicating that OH in the mixed monolayer is much less stable than OH formed at oxygen vacancies. The detailed nature of OH in the mixed layer was consistent with the notion of pseudo-dissociated water. For the anatase $TiO_2(001)$ surface dissociation occurred on the ridges of the (4×1) reconstruction, while a mixture of molecular and dissociated water was formed either in connection to the ridges or on the terraces. The exact composition of the monolayer on the anatase $TiO_2(101)$ was difficult to deduce due to simultaneous desorption of first and second layer water.

Submonolayer growth of Au on the anatase $TiO_2(101)$ surface resulted in two different Au particle types forming, one defect related minority type, which was only discerned up to an Au coverage of 0.14 ML. It appeared to be size-limited and had a constant relative CO uptake. A second particle type was first observed at 0.14 ML Au and continued to grow at higher Au coverages. It exhibited a decreasing relative CO uptake with increasing Au dose. The first particle type was attributed to oxidized gold, nucleating at oxygen adatoms on the terraces, while the second type was believed to be neutral gold particles growing at steps.

High resolution PES and XAS were used to study the formation of an ultrathin TiO_x film on the Pt(110)-(1×2) reconstructed surface. A structural change from a rutile-like structure when TiO_x coexisted with PtO_2 to an anatase-like structure upon completion of the TiO_x bilayer on the Pt surface was observed. A band bending of about 0.8 eV, induced by the PtO_2 structures, was seen for the TiO_x bilayer islands, an effect that disappeared upon completion of the bilayer. The full TiO_x bilayer displayed a band gap 0.2 eV lower than that observed for bulk anatase.

Acknowledgements

First of all, I like to thank my two supervisors, Anne Borg from NTNU and Anders Sandell from Uppsala University. Anne boldly accepted me as her PhD student even though I had no prior experience in experimental research, and she patiently introduced me to the exciting world of surface science, vacuum technology and synchrotron based research. My collaboration with Anders started during my 6 months stay in Uppsala in the spring of 2007. During this period he got me interested in titanium dioxide, which turned out to be the topic of my thesis. Anders amazed me with his extensive knowledge of photoemission spectroscopy and his ability to find interesting physics in almost every single spectrum. I am truly grateful to you both for all your patience, motivation and support during these years.

Doing experimental research at a synchrotron facility, with long working hours and lots of problems and frustrations, would have been almost impossible without the company of good colleagues. I like to thank Ingeborg-Helene, Amutha and Trine from Trondheim, Stefan, Erik and Haakan from Uppsala, and Jacob and Per from Lund, for sharing this experience with me. Also, the help from the MAX-lab staff, especially beam line managers Karina and Alexei, has been indispensable.

I am thankful to the Department of Physics for allowing me to do a PhD there, and to the Strategic Area Materials, NTNU, for the funding.

Doing a PhD is more than just research, teaching is also a major part. I therefore want to thank Knut Arne Strand for close collaboration over the years and interesting discussions about teaching physics and life in general.

Hilde, Henning, Ingeborg-Helene and Øyvind, your friendship has really meant a lot to me. I hope we still can find time to keep in touch even though our student period is over and we probably will end up in different places.

Finally, I like to express my gratitude to my parents, Svein Erik and Anne Torild, and my sister, Marianne, for always being there for me and supporting me through rough times. I really appreciate it.

List of papers

I. Probing and modifying the empty-state threshold of anatase TiO_2: Experiments and ab initio theory.
A. Sandell, B. Sanyal, L. E. Walle, J. H. Richter, S. Plogmaker, P. G. Karlsson, A. Borg and P. Uvdal.
Physical Review B **78**, 075113 (2008).

II. Water Dissociation on Single Crystalline Anatase TiO_2(001) Studied by Photoelectron Spectroscopy.
J. Blomquist, L. E. Walle, P. Uvdal, A. Borg and A. Sandell.
Journal of Physical Chemistry C **112**, 16616 (2008).

III. Experimental evidence for mixed dissociative and molecular adsorption of water on a rutile TiO_2(110) surface without oxygen vacancies.
L. E. Walle, A. Borg, P. Uvdal and A. Sandell.
Submitted to Physical Review Letters (2009).

IV. Mixed dissociative and molecular water adsorption on single crystal anatase TiO_2 surfaces studied by core level photoemission spectroscopy.
L. E. Walle, A. Borg, E. M. J. Johansson, S. Plogmaker, H. Rensmo, P. Uvdal and A. Sandell.
In manuscript.

V. Growth of Au on Single Crystalline Anatase TiO_2(101): Formation of oxidized gold.
L. E. Walle, S. Plogmaker, A. Borg and A. Sandell.
In manuscript.

VI. Growth of ultrathin TiO_x films on Pt(110) studied by high resolution photoemission and X-ray absorption spectroscopy.
L. E. Walle, I.-H. Svenum, A. Borg and A. Sandell.
In manuscript.

Comments on my contribution to the included papers

Scientific work, especially experimental research at a synchrotron facility, requires teamwork. I had the main responsibility for experiments, data analysis and manuscripts in Paper III, IV, V and VI. In Paper I and II, I participated in the experimental work (in Paper I, only for the single crystal experiments) and the following discussions of the results. The DFT calculations in Paper I were performed by Biplab Sanyal at Department of Physics and Materials Science, Uppsala University.

Papers not included in this thesis

- Growth of praseodymium oxide on Si(111) under oxygen-deficient conditions.
  A. Schaefer, V. Zielasek, Th. Schmidt, A. Sandell, M. Schowalter, O. Seifarth, L. E. Walle, Ch. Schulz, J. Wollschläger, T. Schroeder, A. Rosenauer, J. Falta and M. Bäumer.
  Physical Review B **80**, 045414 (2009).

- Adsorption of methanol on Ni_3Al(111) and NiAl(110): A high resolution PES study.
  I.-H. Svenum, Ø. Borck, K. Schulte, L. E. Walle and A. Borg.
  Surface Science **603**, 2370 (2009).

- Methanol Adsorption on Pd(110) and Ag/Pd(110) studied by High Resolution Photoelectron Spectroscopy.
  A. Ramachandran, Ø. Borck, T. H. Andersen, I.-H. Svenum, L. E. Walle and A. Borg.
  Surface Science (2009), doi:10.1016/j.susc.2009.10.015.

- Wealth and income distributions in Norway: A case study.
  H. F. Hansen, L. E. Walle and A. Hansen.
  Submitted to Dynamics of Socio-Economic Systems (2009).

- Adsorption of CO on Ni_3Al(111) and NiAl(110).
  I.-H. Svenum, Ø. Borck, L. E. Walle, K. Schulte and A. Borg.
  Manuscript in preparation.

- Adsorption of methylamine on Ni_3Al(111) and NiAl(110) - a high resolution photoelectron spectroscopy and density functional theory study.

I.-H. Svenum, Ø. Borck, L. E. Walle, K. Schulte and A. Borg.
Manuscript in preparation.

- Adsorption and decomposition of methylamine on Pd(110) studied by high resolution photoelectron spectroscopy and density functional theory.
  T. H. Andersen, A. Ramachandran, Ø. Borck, I.-H. Svenum, L. E. Walle and A. Borg.
  Manuscript in preparation.

- Heterogeneous storage of Li in anatase TiO_2 particles in ultra-high vacuum.
  A. Sandell, L. E. Walle, J. Blomquist, A. Borg and P. Uvdal.
  Manuscript in preparation.

- Comparing surface binding of the maleic anhydride anchor group on single crystalline anatase TiO_2(101), (100) and (001) surfaces.
  E. M. J. Johansson, S. Plogmaker, L. E. Walle, R. Schölin, A. Borg, A. Sandell and H. Rensmo.
  Manuscript in preparation.

Contents

Part I

Introduction

Chapter 1

Introduction

In 1959 Richard P. Feynman stated that there is "plenty of room at the bottom" [1]. By this he meant that there are plenty of new exciting phenomena to be found if we are able to gain control of matter down to the atomic level. During the last decades we have witnessed numerous examples of atomically controlled preparations of systems with amazing properties. Many of these have been prepared and characterized using surface science methodology, which provides information on the characteristic physical and chemical properties in the surface region of a solid and the interaction of surfaces with adsorbed atoms and molecules. The interest in studying surfaces has since the 1960's resulted in a number of surface sensitive experimental techniques using photon, electron, molecule and ion scattering, as well as scanning probe methods [2]. Currently, this field has reached a high level of maturity and systems with increasing complexity are targeted.

A surface represents an abrupt change in the symmetry compared to the bulk of a material, leading to a lower coordination of the atoms in the topmost surface layer. The reduced coordination means higher energy, resulting in a high reactivity [3]. The changed properties in the surface region give rise to other phenomena compared to the bulk, for instance surface reconstructions, where the surface atoms rearrange to reduce the energy of the surface, and surface states that are forbidden in the bulk [3,4]. Moreover, surface behaviour is important for understanding fundamental processes in real-world applications, including heterogeneous catalysis, corrosion, fabrication of semiconductor devices and development of nanomaterials and nanotechnology [5].

Surface science investigations are commonly associated with studies of single crystal surfaces, offering a well-ordered array of atoms, under ultra-high vacuum

(UHV) conditions [2]. Links to applications can be obtained through selecting simple systems that can model certain aspects of a more complex behaviour. In this context, single crystals serve as well-defined model systems where it is possible to experimentally study surface processes while the number of unknowns can be kept to a minimum. The usefulness of this approach was underscored in 2007 when the Nobel Prize in chemistry was awarded Prof. Gerhard Ertl for his studies of chemical processes on solid surfaces.

1.1 Motivation for studying TiO_2 systems

Titanium dioxide, commonly referred to as titania, is a non-toxic, wide band gap semiconductor which has become one of the most-commonly investigated metal oxide systems in surface science. Polished crystals with a high surface quality are readily available. TiO_2 crystallizes in three major different structures: rutile, anatase and brookite. Only the rutile and anatase phases play a role in applications [6].

The main reason for studying TiO_2 is to gain a detailed understanding of fundamental aspects of its surfaces and interfaces. Such knowledge can potentially have a positive impact on several technological applications, including heterogeneous catalysis, photocatalysis, solar cells for production of hydrogen and electric energy, gas sensors, white pigment, corrosion-protective coatings, optical coatings, ceramics, electric devices, biomedical implants, Li-based batteries and electrochromic devices. TiO_2 is also being discussed as a possible material for the gate insulator for the next generation of MOSFETS. The hope is that insight into the surface properties on the fundamental level can help improve materials and device performance in many of these fields. Furthermore, an important question concerning the future of nanotechnology is how one should manufacture nanodevices outside the laboratory while maintaining the desired functionality on the atomic scale. The functionality of these devices requires control over molecular adsorption, deposition of metal particles and insertion of alkali ions, which are questions that can be tackled by surface science [7].

As an example, a well-known molecular modification of TiO_2 is the dye-sensitized solar cell electrode [8]. Here light is harvested by a dye molecule and electrons are injected into the TiO_2 conduction band before regeneration of the dye is accomplished by a hole-conductor closing the circuit. Most important for the success of this application is the use of a nanoporous TiO_2 film, providing a huge internal area of the film onto which large dye molecules are anchored. The role of the dye

molecule anchor group and its interaction with the TiO_2 substrate are key issues for the solar cell performance.

Already in the 70's photocatalytic production of hydrogen from water on a rutile TiO_2 single crystal was observed [9]. The prospect of converting solar energy to chemical energy for hydrogen production has therefore been a strong motivation for studies of water interaction with TiO_2 [10]. However, since pure TiO_2 has a rather low activity towards photocatalytic water splitting under band gap radiation, carefully designed systems are required in order to effectively separate the photogenerated electrons and holes. A well-known example is the TiO_2-Pt photoelectrochemical cell, where oxygen evolves from the TiO_2 anode whereas hydrogen is produced at the Pt cathode [11].

In this thesis synchrotron based photoelectron spectroscopy and X-ray absorption spectroscopy have been used to study adsorption behaviour of technological important single crystal TiO_2 systems and the growth of thin TiO_2 films on metal substrates. In Paper I the conduction-band edge, which is an important aspect for all processes involving electrons populating the conduction band, of single crystalline and nanostructured anatase TiO_2 is explored. Paper II, III and IV are directed towards photochemical water splitting by dealing with adsorption of water on the rutile $TiO_2(110)$ and the anatase $TiO_2(101)$ and (001) surfaces. Gold nanoparticles, functioning as an effective catalyst for several process, on an anatase $TiO_2(101)$ support are explored in Paper V. In the last paper ultrathin TiO_x films assembled on a Pt(110) surface are investigated, serving as nanosheet models.

1.2 The structure of titanium dioxide

In the following, the structures of the rutile and anatase phases of TiO_2 are shortly presented. Formally, both anatase and rutile have a tetragonal bulk unit cell which is made up of titanium ions (Ti^{4+}) at the center of an octahedron of six oxygen (O^{2-}) ions, and the two polymorphs mainly differ by distortion inside the octahedron [6]. The unit cells of anatase and rutile are shown in Fig. 1.1. The average distance between the Ti^{4+} ions in anatase is smaller compared to rutile, which makes it thermodynamically less stable in bulk form. However, for grains smaller than 14 nm in diameter anatase becomes thermodynamically more stable than rutile, which explains why anatase often stabilizes in nano structures [13]. By heating to between 700 – 1000°C, depending on crystal size and impurity content, it is possible to convert anatase into rutile [14].

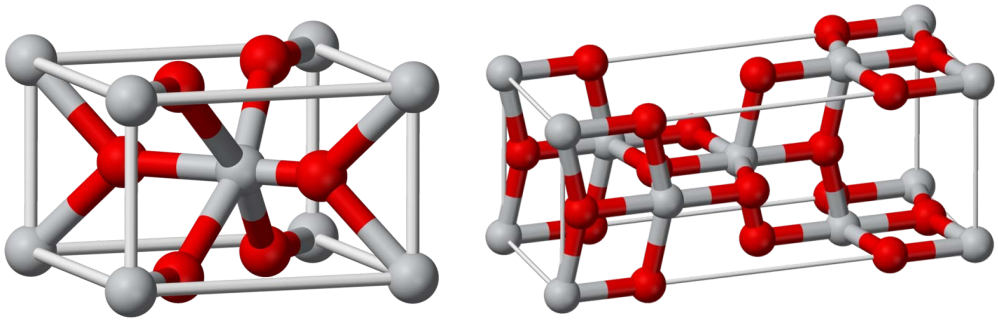

Figure 1.1: Bulk unit cell of (left) rutile (with dimensions $a = b = 4.587$ Å$, c = 2.953$ Å) and (right) anatase (with dimensions $a = b = 3.782$ Å$, c = 9.502$ Å) TiO_2. Oxygen atoms are coloured red while titanium atoms are grey. In both structures, slightly distorted octahedra are the basic building units. The figures are taken from [12].

Despite anatase being the favourable phase in applications, experimental surface studies of TiO_2 have so far been focused on rutile. This is primarily due to the difficulty of obtaining anatase samples of good quality. While rutile samples are easy to manufacture, the metastable nature of anatase complicates the growth of crystals large enough for convenient sample handling. Therefore, investigations of anatase TiO_2 often use natural grown mineral samples cut at the desired orientation. However, these crystals may be brittle and often contain impurities like alkali and alkaline earth elements, complicating the experiments.

In this thesis, we have mainly studied the rutile $TiO_2(110)$-(1×1) surface, and the anatase $TiO_2(101)$-(1×1) and (001)-(4×1) surfaces. The most stable rutile surface, $TiO_2(110)$, has become a benchmark surface for fundamental studies of metal oxides because it is well-characterized, easy accessible and maintains a bulk-like structure. The atoms are arranged in alternating rows of fivefold-coordinated Ti atoms and twofold-coordinated bridging oxygen atoms [6, 7], as shown in Fig. 1.2.

The clean anatase $TiO_2(101)$ surface, illustrated in Fig. 1.3 (a), is also bulk terminated, consisting of twofold coordinated bridging oxygen atoms and fivefold coordinated Ti atoms with a density comparable to the one found on rutile (110) [16]. Whereas, the clean anatase $TiO_2(001)$ surface undergoes a (4×1) reconstruction in UHV [17,18]. A model of this surface structure has been derived from scanning tunneling microscopy (STM) in conjunction with density functional theory (DFT) calculations [19, 20], shown in Fig. 1.3 (b). The surface can be described as con-

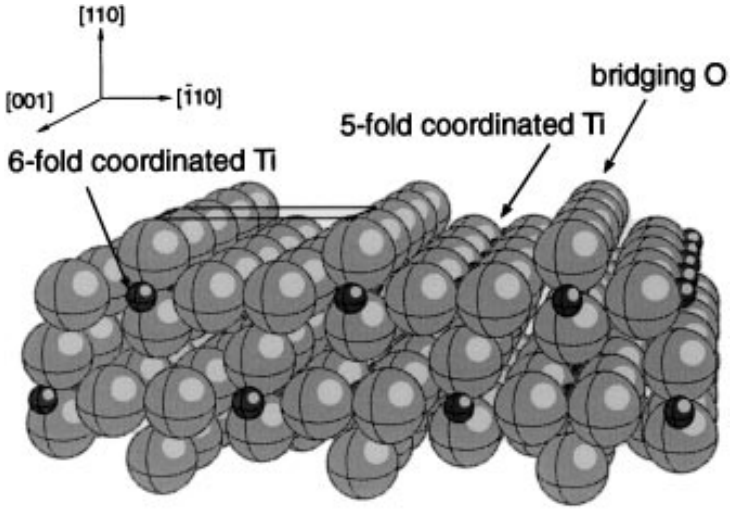

Figure 1.2: The rutile TiO_2(110)-(1 × 1) surface. Small spheres represent Ti and large spheres represent O. The illustration is taken from [15]

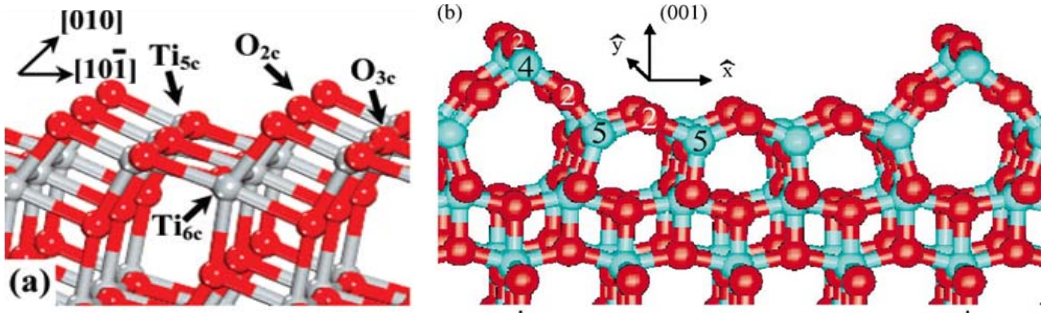

Figure 1.3: Structure model for the (a) (101)-(1 × 1) and (b) (001)-(4 × 1) surfaces of anatase TiO_2. The figures are taken from [6, 21].

sisting of ridges, made up by TiO_3 chains, separated by terraces. The Ti atoms of the ridges are four-fold coordinated only while the terrace Ti atoms are five-fold coordinated. Therefore, the ridges are often more reactive upon adsorption.

Chapter 2

Experimental techniques

This chapter gives a short introduction to the principles of the experimental techniques used to study surfaces in this thesis. First, the need for vacuum and how the samples are prepared are presented, before the basics of the following techniques are explained: low energy electron diffraction (LEED), photoelectron spectroscopy (PES), X-ray absorption spectroscopy (XAS) and synchrotron radiation.

2.1 Vacuum and sample preparation

2.1.1 Vacuum

The topic of this thesis is how clean surfaces of single crystals interact with different adsorbates and thin films of metals or metal oxides. If these studies had been performed at ambient pressure conditions, the surfaces would instantly be covered with contaminants from the air. Such contaminants can seriously alter the system and give uncontrolled results. For instance, if we assume that all the molecules hitting a surface actually stick, it will only take 3 seconds to cover the surface completely at a background pressure of 10^{-6} mbar [2]. Thus, to be able to work with a clean surface for several hours, the experiments presented in this thesis have been performed at ultra-high vacuum (UHV) conditions, typically in the low 10^{-10} mbar pressure range. For comparison, the pressure at the surface of the moon is about 10^{-11} mbar [22].

To achieve such low pressures, a combination of special materials, effective pump-

ing and baking of the system is required. Modern vacuum chambers are usually made of stainless steal and use three different types of pumps: turbo molecular pumps, ion pumps and titanium sublimation pumps [23]. Pumping alone is not enough to reach a pressure in the low 10^{-10} range. The pressure will be limited by the desorption of adsorbed gases, mainly water vapour, from the inner walls of the chamber. By baking the system, which means heating the whole chamber to temperatures above 100°C for approximately 24 hours, the rate of desorption is increased and the coverage of adsorbed gases on the surfaces reduced, resulting in a lower pressure [2].

2.1.2 Sample preparation

In order to obtain atomically clean surfaces, the crystals must be cleaned in UHV. For our TiO_2 and Pt single crystals, this was done by repeated cycles of argon sputtering and annealing. During sputtering the surface is bombarded with high energy (typically between 0.5 and 2 keV) Ar^+ ions that knock out atoms and molecules, including impurities, in the surface region. After sputtering the surface will be in a heavily damaged and disordered state, often with embedded Ar atoms. This can be amended by annealing (i.e. heating) the sample. Annealing results in desorption of weakly bound adsorbed species, as well as reordering of the damaged surface. Annealing temperature and time vary between materials and different surface reconstructions. The cleaning procedure is usually repeated until no contaminations can be detected by photoemission, and a sharp LEED pattern (see section 2.3) is observed. The number of necessary cleaning cycles will depend on the type of sample and its previous history. Further details of the cleaning procedure for the different crystals can be found in the individual papers.

Several of our experiments involve exposing the samples to gases (O_2 and CO) or vapour from liquids (H_2O). The molecules are introduced into the UHV system through a leak valve, while monitoring the pressure with the ion gauge. Gas exposure is measured in Langmuir, where $1\ \mathrm{L} = 1.33 \cdot 10^{-6}$ mbar$\cdot$s [24].

In Paper V and VI, metal is evaporated onto the samples. For gold, this was done from a tungsten crucible heated by electron bombardment in an e-beam evaporator. Titanium, on the other hand, was evaporated by sending direct current through a Ti wire filament. In both cases the evaporation rate was determined by using a quartz crystal microbalance, which measures the deposited mass by monitoring the change in frequency of a quartz crystal resonator [25]. The microbalance was placed at the sample position and therefore gave a direct measure of the deposited material.

2.2 The electron mean free path

All the experimental techniques used in this thesis rely on the detection of electrons emitted from the sample, typically with an energy between 0 and 1500 eV. Electrons at these kinetic energies interact strongly with matter and therefore have a short inelastic mean free path. The inelastic mean free path is the average distance an electron can move before it loses energy [2, 3]. Fig. 2.1 shows the mean free path for electrons in different solids as a function of kinetic energy. The dashed curve shows a calculated mean free path independent of the material. Since the experimental points for many different solids follow this trend line, it is commonly called the universal curve. From the figure we see that the mean free path has a broad minimum centered around a kinetic energy of 70 eV, with a value of less than 10 Å. This means that detected electrons with kinetic energies in this energy range must originate from the surface region, which is the main reason why the electron based techniques have high surface sensitivity. The universality of the mean free path curve is caused by the fact that the density of conduction electrons is more or less the same for all elements, and excitation of these conduction electrons is the main origin of the inelastic scattering in this energy range [3].

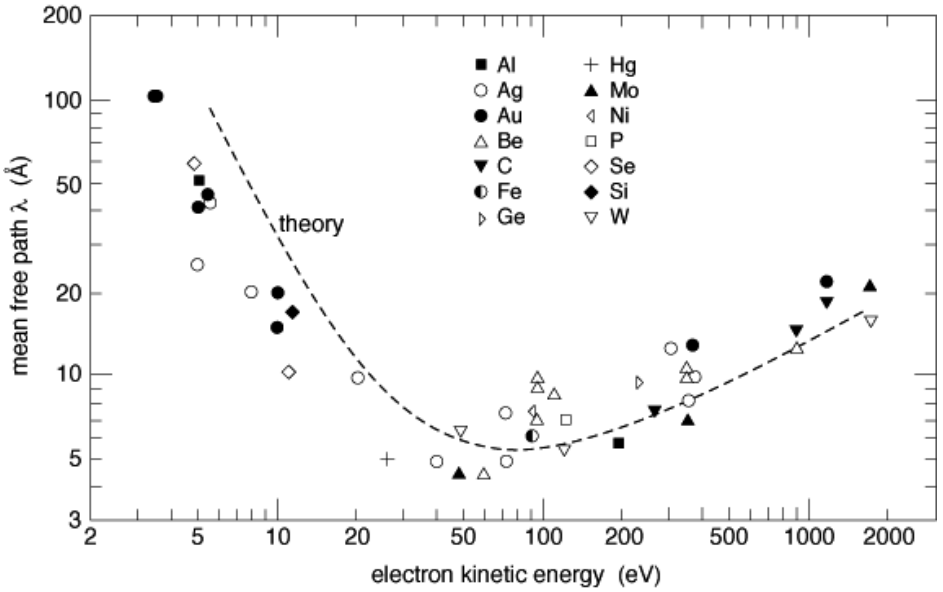

Figure 2.1: The inelastic mean free path for electrons in different solids as a function of kinetic energy. The dashed line is based on theoretical calculations and is called the universal curve. The figure is taken from [26], which is based on [3].

2.3 Low energy electron diffraction (LEED)

Low energy electron diffraction (LEED) is rooted in the fact that electrons have a wave-particle duality. Louis de Broglie suggested in 1924 that electrons could be treated as waves with a wavelength given by $\lambda = \frac{h}{p} = \frac{h}{\sqrt{2mE}}$, where h is Planck's constant, p the linear momentum and E the energy of the electron [27]. This opened up the possibility that electrons could be diffracted by crystalline solids, which was confirmed experimentally by Davisson and Germer in 1927 who observed diffraction effects from a single crystal of nickel [28, 29]. In the 1960's the technique was further developed by Germer and co-workers into today's modern LEED system [30].

In LEED electrons in the kinetic energy range 20–300 eV are applied, yielding wavelengths around 1 Å, which is in the same order of magnitude as the periodicity of the atomic lattice, a requirement for forming diffraction patterns [2,31]. The short mean free path of low energy electrons (see Fig. 2.1), typically around 10 Å for 100 eV electrons, makes LEED a highly surface sensitive method. LEED patterns are therefore due to diffraction from only the few topmost atomic layers of a surface [3], making the technique an important tool for determining surface structure and periodicity. It can provide information on average bond angles, nearest neighbour distances and translational symmetry. In addition, the sharpness of the diffraction pattern reflects the long range order of the surface. LEED is therefore often used to evaluate the cleanness of a surface, and to study surface reconstructions and overlayer structures [31, 32].

A schematic diagram of a typical LEED system is shown in Fig. 2.2. It consists of an electron gun with a variable accelerating potential ($-V_E$) which generates a monoenergetic electron beam. The electrons are accelerated and focused by a series of electrostatic lenses before hitting the grounded sample. A hemispherical retarding-field energy analyzer, consisting of four hemispherical concentric grids and a fluorescent screen, is used for detecting the electrons [2,31]. Electrons scattered from the surface travel to the first spherical sector grid, which is at the same potential as the sample providing a field-free region between the sample and the grid. The next two grids have a potential of $-V_E + \Delta V$. By adjusting ΔV, inelastically scattered electrons, which would otherwise only contribute to a diffuse background in the diffraction pattern, are prevented from entering the acceleration field between the fourth grid and the screen. After being accelerated to about 6 keV, the diffracted electrons hit the fluorescent screen, where the diffraction pattern can be observed.

The LEED pattern can be shown to be in direct correspondence to the reciprocal

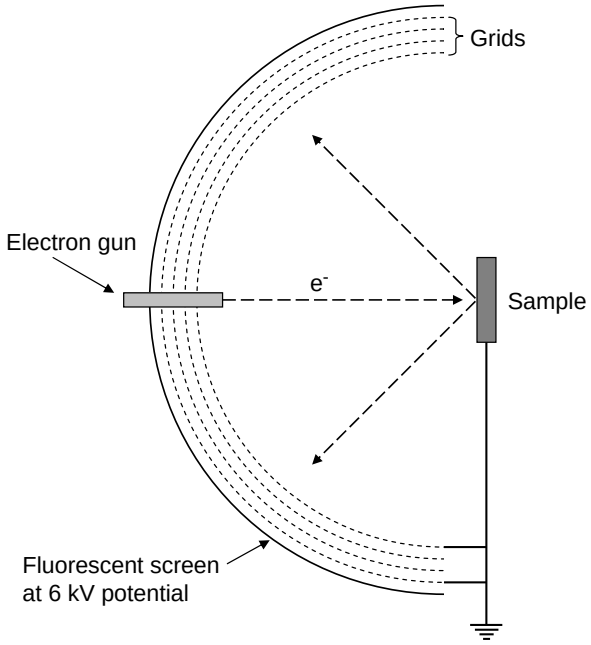

Figure 2.2: A schematic diagram of a typical LEED optics. The sample is grounded and placed in the centre of a hemispherical retarding-field energy analyzer consisting of 4 grids and a fluorescent screen. An electron gun, inserted through a central hole in the screen, emits electrons that are diffracted at the sample surface and backscattered towards the analyzer [2, 31].

lattice of the surface. If $\mathbf{a}_1$ and $\mathbf{a}_2$ are two lattice vectors of a two dimensional real space lattice, and $\mathbf{a}_1^*$ and $\mathbf{a}_2^*$ are lattice vectors for the corresponding reciprocal lattice, the vectors are related by [32]

$$\mathbf{a}_1 \cdot \mathbf{a}_1^* = \mathbf{a}_2 \cdot \mathbf{a}_2^* = 1, \tag{2.1}$$

$$\mathbf{a}_1 \cdot \mathbf{a}_2^* = \mathbf{a}_1^* \cdot \mathbf{a}_2 = 0. \tag{2.2}$$

Reconstructions and overlayers are always referred to the periodicity of the substrate. The lattice vectors of the overlayer or reconstruction ($\mathbf{b}_1$ and $\mathbf{b}_2$) are related to the substrate ($\mathbf{a}_1$ and $\mathbf{a}_2$) by the following relation [2, 31]

$$\begin{bmatrix} \mathbf{b}_1 \\ \mathbf{b}_2 \end{bmatrix} = \begin{bmatrix} G_{11} & G_{12} \\ G_{21} & G_{22} \end{bmatrix} \begin{bmatrix} \mathbf{a}_1 \\ \mathbf{a}_2 \end{bmatrix} = G \begin{bmatrix} \mathbf{a}_1 \\ \mathbf{a}_2 \end{bmatrix}. \tag{2.3}$$

As suggested by Park and Madden [33], the matrix G can be used to state the structure of a reconstruction or overlayer. However, often a simpler notation, the

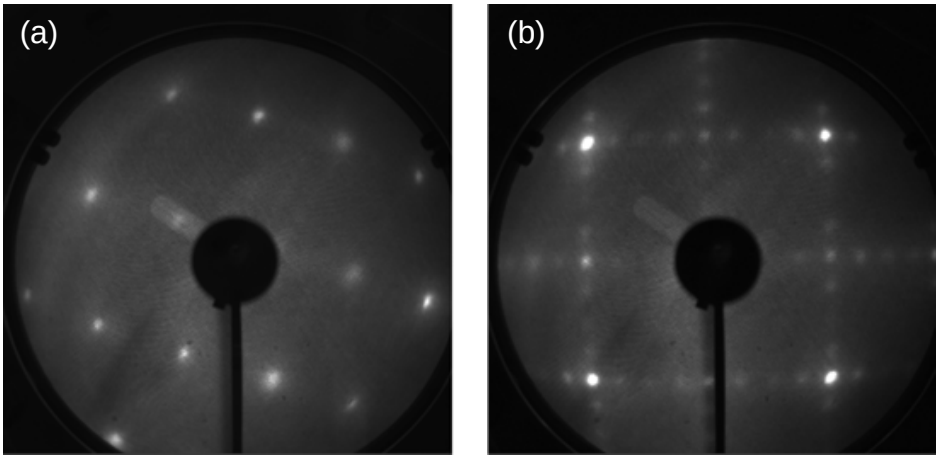

Figure 2.3: LEED patterns of the pristine anatase TiO_2(101) and (001) surfaces. (a) The (101) surface is bulk terminated and shows a (1×1) LEED pattern. The diffraction pattern was recorded at an electron kinetic energy of 142 eV. (b) The (001) surface undergoes a (4×1) surface reconstruction, recorded at an electron kinetic energy of 147 eV.

Wood-notation [34], is used. Here the ratio of the lengths of the overlayer and substrate nets, together with a possible rotation angle α, are used, which can be expressed as

$$\left(\frac{|\mathbf{b}_1|}{|\mathbf{a}_1|} \times \frac{|\mathbf{b}_2|}{|\mathbf{a}_2|}\right) \mathrm{R}\alpha. \tag{2.4}$$

In Fig. 2.3 the Wood notation is used for describing the LEED pattern of the clean anatase TiO_2(101) and (001) surfaces.

2.4 Synchrotron radiation

Techniques like photoelectron spectroscopy require an X-ray or ultraviolet (UV) source to produce the radiation. This can be achieved either by using a conventional X-ray tube or by using a synchrotron. Synchrotron radiation facilities, with their ability to produce tunable radiation of high intensity, have opened up many new possibilities in electron spectroscopy [35,36]. Some of these include resonant photoemission, soft X-ray absorption, surface magnetism studies, photoelectron microscopy and photoelectron diffraction. Most important, the high brilliance[1] of

[1] Brilliance is defined as $\#\text{photons}/(\text{s} \cdot \text{mm}^2 \cdot \text{mrad}^2 \cdot 0.1\% \,\text{bandwidth})$ [38].

these sources facilitates a high degree of monochromatization, which has made it possible to perform core level photoelectron spectroscopy of very high energy resolution.

Another important aspect of synchrotron radiation is the ability to tune the photon energy. In a home laboratory you usually only have access to a few standard X-ray and UV sources with fixed energies (typically Al K_α, Mg K_α, He-I and He-II radiation), while at a synchrotron the energy can be selected freely within a wide energy range. Since the inelastic mean free path of electrons depends on their kinetic energy, this means that the degree of surface sensitivity can be chosen. In addition, tunable photon energy is essential for techniques where you need to scan the energy, like X-ray absorption spectroscopy.

2.4.1 Basic principles of synchrotron radiation and synchrotron storage rings

Accelerated charged particles, such as electrons travelling on a curved trajectory, will emit radiation. If the particles move at relativistic speed, the radiation will be emitted in a narrow cone tangential to the path of the particles [37]. This forms the basis for synchrotron radiation. Synchrotron radiation was first observed as energy loss in electron storage rings used for high-energy physics, and the radiation was utilized for scientific experiments by extracting light through parasitic beam ports taking advantage of the otherwise lost radiation [38]. Later, dedicated synchrotron radiation sources were built.

In today's synchrotron facilities (often called *third generation facilities*) the storage rings consist of many straight sections separated by bending magnet sections. Electrons are accelerated to relativistic speed in a linear accelerator before they are injected into the storage ring and further accelerated there. The trajectory of the electrons in the ring is controlled by the use of various magnetic lenses. Synchrotron radiation can be created either by bending magnets, or by insertion devices (undulators and wigglers) in the straight sections of the storage ring. While bending magnets cause the electrons to move in a single curved trajectory, undulators and wigglers consist of periodic magnetic structures forcing the electrons to experience harmonic oscillations as they move through the insertion device. Fig. 2.4 shows a schematic illustration of an undulator. The main difference between an undulator and a wiggler is the strength of the magnetic field, and therefore also the amplitude of the electron oscillations. Undulators operate with relatively weak magnetic fields and the generated radiation from each period of the

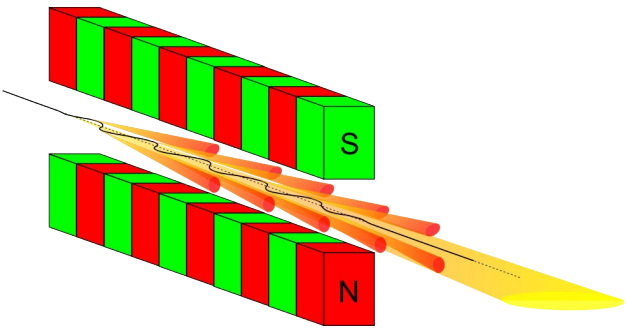

Figure 2.4: Schematic illustration of the radiation emitted by the periodic magnetic structure in an undulator. The figure is taken from [39].

magnetic structure is added in phase, resulting in a narrow radiation cone with extremely bright and partially coherent radiation. The wavelength of the emitted radiation from an undulator can be tuned by changing the gap between the magnets in the periodic structure. Wigglers are a strong magnetic field version of undulators. Here the radiation is not added in phase, resulting in a broader radiation cone in both space and angle. The radiation spectrum from a wiggler is similar to a bending magnet, except that it is shifted to higher energies and the total radiated power is much higher [38]. Fig. 2.5 shows the radiation cone and the radiation spectrum for bending magnets, wigglers and undulators.

The radiation produced by the synchrotron is directed into beamlines where the desired energy can be selected using a grating monochromator. Finally the monochromatized light is focus onto the sample in the experimental station. To avoid energy losses due to collisions between electrons and air molecules, and because soft X-ray radiation (typically in the energy range of 30–1500 eV) is strongly absorbed by air, both the storage ring, the beamlines and the end stations have to be under vacuum [38].

2.4.2 Beamlines D1011 and I311 at MAX-lab

All the experiments presented in this thesis have been carried out at either beamline D1011 or I311 of the MAX II storage ring at the Swedish National Synchrotron Laboratory, MAX-lab [41], located in Lund. The MAX II ring has a circumference of 90 m and stores electrons with an energy of 1.5 GeV [42]. Fig. 2.6 shows a schematic overview of the storage rings and beamlines at MAX-lab.

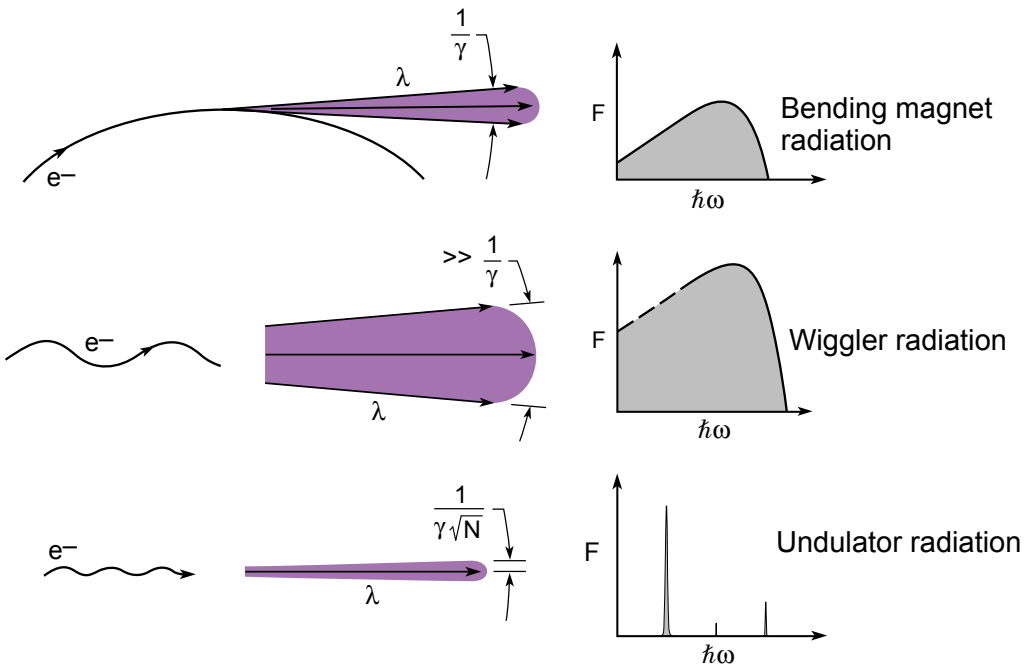

Figure 2.5: The radiation cone and radiation spectrum from bending magnets, wigglers and undulators. The width of the radiation cone is determined by γ, which is given by the electron energy (E_e) in the storage ring, $\gamma = \frac{E_e}{mc^2} = 1957 \cdot E_e(\mathrm{GeV})$, and N, which is the numbers of periods in the magnetic structure. The figure is taken from [40].

Beamline D1011 [43] is a bending magnet beamline, while I311 [44] is undulator based. Both beamlines are equipped with a modified SX-700 monochromator and cover a photon energy range of 30–1500 eV. In addition to the usual equipment for preparation and characterization of surfaces in UHV (sputter gun, LEED optics, etc.), the experimental stations of both beamlines are equipped with a 200 mm hemispherical electron energy analyzer of Scienta type providing for high resolution photoelectron spectroscopy (PES) and X-ray absorption spectroscopy (XAS).

Even though both I311 and D1011 are specially designed for surface studies, they have different strengths and weaknesses, and complement each other. Since I311 is undulator based, it has a small spot size and a high photon flux which is needed for studying low doping levels, low coverages, band mapping and resonant processes. D1011, on the other hand, has a larger spot and lower photon flux because of the bending magnet. This is ideal for studying metal-organic precursor

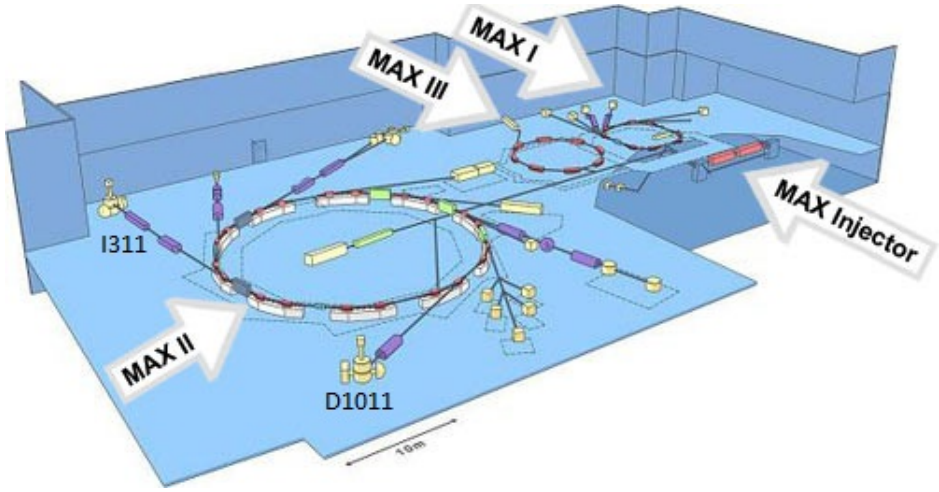

Figure 2.6: Schematic overview of MAX-lab. The figure is taken from the MAX-lab homepage [41].

molecules and water, which are very susceptible to radiation damage. Fig. 2.7 shows the experimental stations of the D1011 beamline. Our experiments at this beamline have all been carried out in the front station.

2.5 Photoelectron spectroscopy (PES)

Photoelectron spectroscopy[2] (PES) is an experimental technique based on the photoelectric effect that probes the occupied electronic levels in a material [46]. The photoelectric effect was discovered experimentally by Hertz in 1887 [47] and later explained by Einstein in 1905 [48], an achievement for which he was awarded the Nobel Prize in Physics in 1921. Hertz observed that when a material was exposed to electromagnetic radiation, it emitted electrons (photoelectrons), but he could not explain why the kinetic energy of the electrons seemed to be independent of the intensity of the radiation. Einstein solved this problem by treating light as particles (photons) with a precise energy and by proposing that a minimum energy is required to make an electron escape from a solid. This threshold energy depends on the material and is given by

$$E_{\text{min}} = h\nu_{\text{min}} = \Phi, \tag{2.5}$$

[2] Also called photoemission spectroscopy.

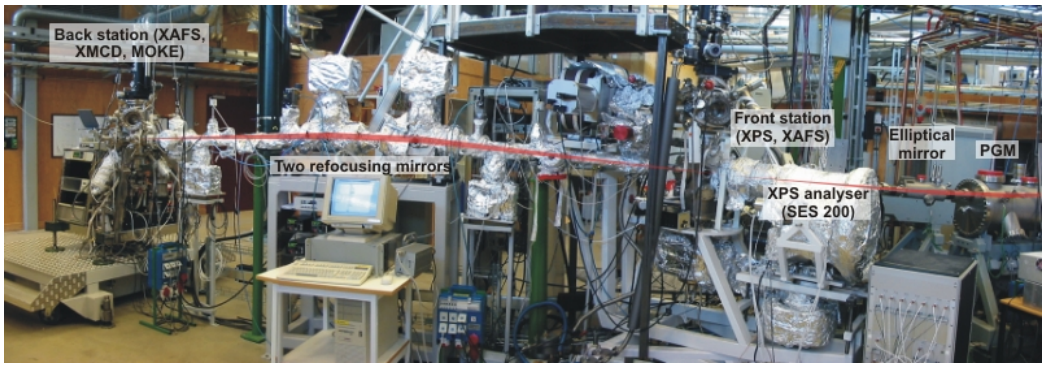

Figure 2.7: The two experimental stations of the D1011 beamline at MAX-lab. The front station features photoemission and X-ray absorption spectroscopy, while the back station is optimized for studying magnetic materials. The picture is taken from [45].

where h is Planck's constant, ν is the frequency of the incident photon and Φ is the work function for the given material.

In the 1950's and 1960's Kai Siegbahn (awarded the Nobel Prize in Physics in 1981) and co-workers in Uppsala developed the technique we today know as photoelectron spectroscopy [49]. Because of its chemical specificity it was originally called *Electron Spectroscopy for Chemical Analysis* (ESCA). Photoelectron spectroscopy provides information on the atomic composition of a sample as well as the chemical states and electronic structure of the observed atoms. Since the introduction of soft X-ray synchrotron radiation sources, PES has become one of the major techniques for studying surfaces, interfaces and thin films [24].

2.5.1 The principles of photoelectron spectroscopy

PES relies on detecting emitted photoelectrons and determining their kinetic energy. This is accomplished by the use of an electron spectrometer. A hemispherical type electron spectrometer is illustrated in Fig. 2.8. It consists of a set of electronic lenses, an energy analyser and a detector [2, 46]. After being emitted from the sample, the photoelectrons are collected, accelerated or decelerate to a selected pass energy and focused onto the entrance of the energy analyser by the electron lenses. A concentric hemispherical analyser (CHA), which is made of two concentric hemispheres with an applied voltage difference, is then used to

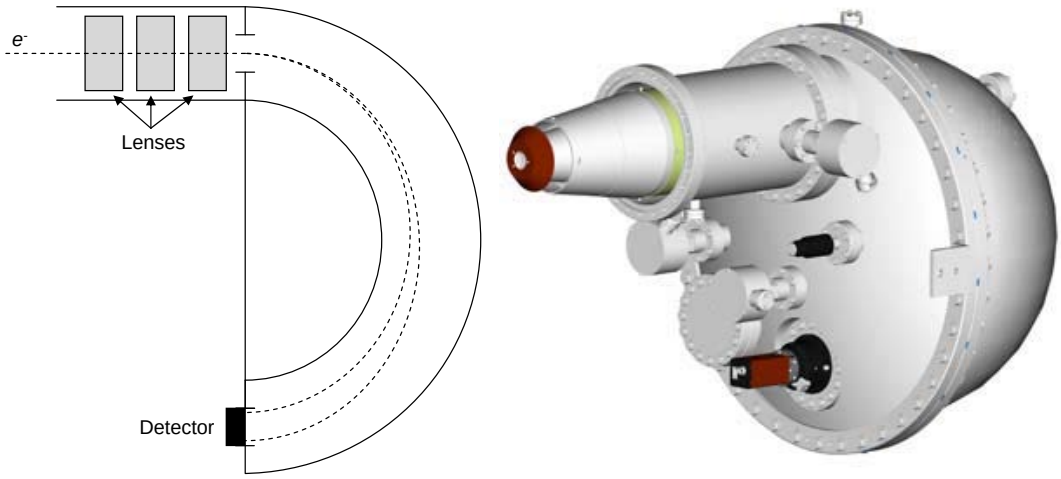

Figure 2.8: (Left) A schematic diagram of a typical electron spectrometer which is used to determine the kinetic energy of photoelectrons. It consists of a set of electronic lenses, a concentric hemispherical analyser (CHA) and a detector. (Right) A model of a spectrometer, taken from [50].

disperse the incoming electrons according to kinetic energy and momentum. Finally the electrons reach a detector commonly consisting of two micro-channel plates connected to a phosphor screen. Electrons accelerated onto the phosphor screen give off a light flash which is counted by a CCD camera.

The main features of the photoemission process are summarized in Fig. 2.9. When a sample is irradiated by light, the photons may be absorbed and excite a core or valence electron, which can be emitted. Since the total energy is conserved, the process can be described by

$$E_{\mathrm{i}} + h\nu = E_{\mathrm{f}} + E_{\mathrm{kin}}, \tag{2.6}$$

where $h\nu$ is the energy of the incoming photons, E_{kin} the kinetic energy of the emitted photoelectrons, and E_{i} and E_{f} the initial and final state energies of the system. The binding energy of the electrons, E_{B}, is then defined as the difference in total energy before and after excitation

$$E_{\mathrm{B}} = E_{\mathrm{f}} - E_{\mathrm{i}} = h\nu - E_{\mathrm{kin}}. \tag{2.7}$$

Given that the energy of the incoming photons is $h\nu > E_{\mathrm{B}} + \Phi_{\mathrm{S}}$, electrons with binding energy E_{B} can be excited into the vacuum region. Φ_{S} is here the work function of the sample. By using the electron energy analyser for measuring the

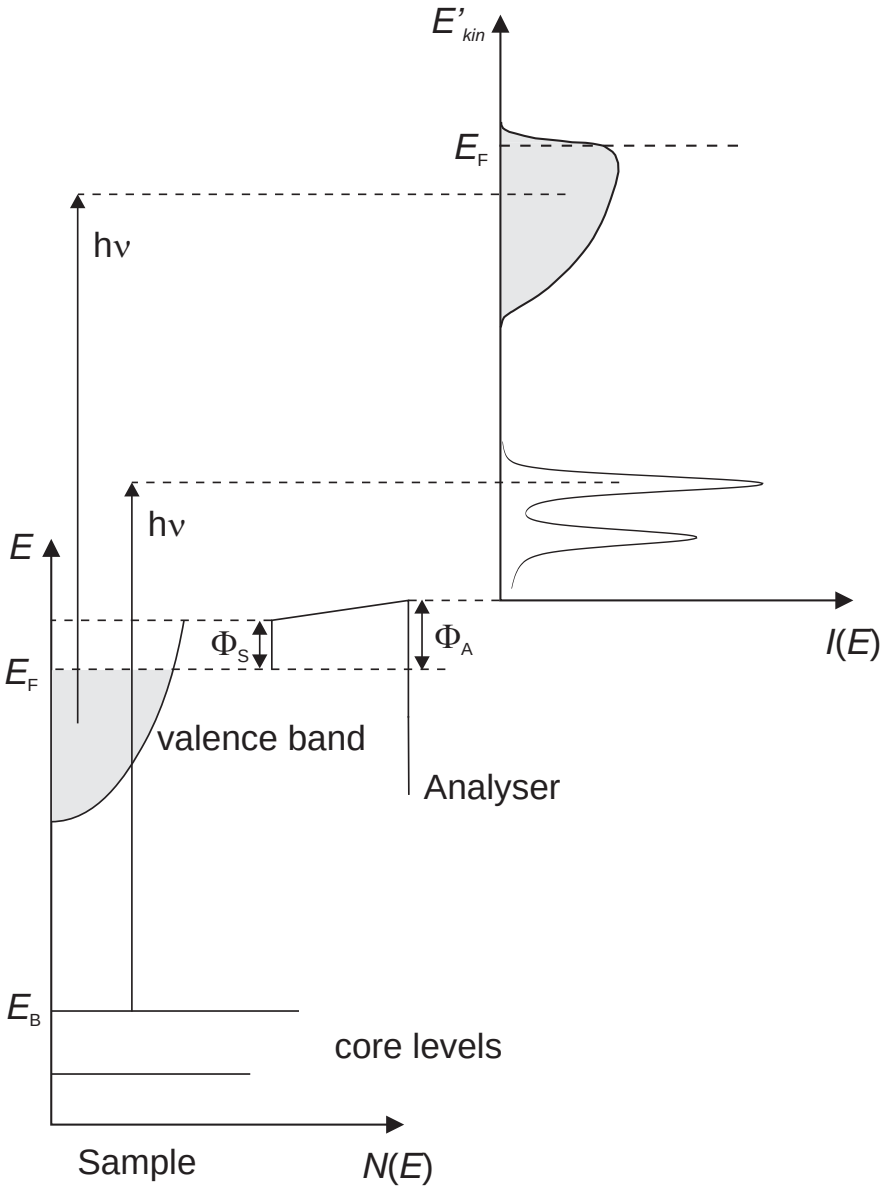

Figure 2.9: Schematic illustration of the photoelectron spectroscopy principle. Incoming photons of sufficient energy can excite core or valence electrons into the vacuum region, where their kinetic energy are measured by an electron energy analyser, after overcoming the work function of the analyser, Φ_A. When the analyser energy is scanned this produces a photoemission spectrum, $I(E)$, which is related to the electronic density, $N(E)$, in the sample. The figure is taken from [51], which has been adapted from [52].

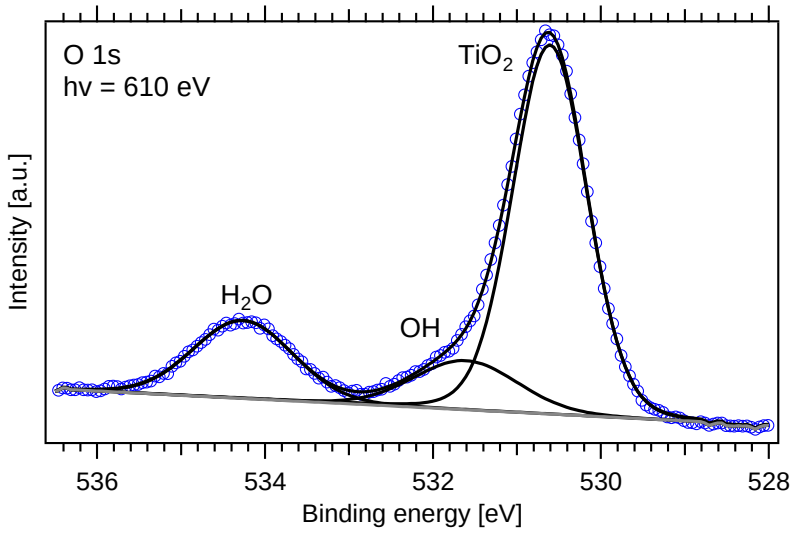

Figure 2.10: O 1s photoemission spectrum of water adsorbed on the rutile $TiO_2(110)$ surface at 210 K. The spectrum is recorded at 610 eV photon energy and 60° off-normal emission angle to allow for the observation of OH on the surface when substrate oxygen is present.

kinetic energy of the photoelectrons, the binding energy can be calculated by

$$E_B = h\nu - E'_{kin} - \Phi_A, \tag{2.8}$$

where E'_{kin} is the kinetic energy as measured by the spectrometer and Φ_A is the work function of the analyser. To be detected the photoelectrons have to overcome the work function Φ_A of the analyser, which in general is different from Φ_S. This is the reason why the measured kinetic energy, E'_{kin}, is slightly different from E_{kin} in eq. (2.7). The measured distribution of photoelectrons, $I(E)$, is related to the electronic density, $N(E)$, in the sample. For solid surfaces the binding energy is usually referenced to the Fermi level (E_F) [2, 46].

2.5.2 Surface sensitivity of PES

Even though photons can penetrate several micrometers into a sample, photoelectron spectroscopy is a highly surface sensitive technique because of the short inelastic mean free path of electrons with an energy in the range 10–1000 eV. In order to increase the surface sensitivity even further two approaches can be taken: (1) the kinetic energy can be optimized with respect to the mean free path by an

appropriate choice of photon energy, or (2) the angle between the sample and the detector can be altered to increase the amount of emitted photoelectrons originating from the surface relative to the bulk [46]. In Paper II, III and IV, both these two approaches had to be combined to increase the surface sensitivity sufficiently to be able to separate the peak due to adsorbed OH species from the much stronger TiO_2 substrate peak in the O 1s spectrum, as illustrated in Fig 2.10.

2.5.3 Core levels and core level shifts

Core levels are localized electronic states that do not participate in chemical bonding. Even so, they are influenced by changes in the local charge and potential of the atom [46, 53]. Emitted electrons from atoms with different chemical environments will therefore have a slight energy difference and the core level peak in the photoemission spectrum may be split into features with slightly different binding energies [54]. These shifts are called chemical shifts or core level shifts. Studying chemical shifts can provide information on how the atoms are chemically bonded in a system, and they may also be used as a fingerprints to identify various chemical states of the atom. An example of a chemical shift due to CO directly bonded to Au atoms on an anatase $TiO_2(101)$ surface is shown in Fig. 2.11.

Another kind of shift which is often observed in high resolution photoemission experiments, are surface core level shifts. These shifts are caused by the reduced coordination of the surface atoms of the material. Surface core level shifts are present for most materials and are expected to be larger for open surfaces because of the smaller coordination number compared to more closely packed surfaces [46]. The direction and magnitude of the surface core level shift depend on the difference in cohesive energies between the initial and final states of the bulk and surface atoms, as shown using a Born-Haber-approach by Johansson et al. [55].

As can be seen from eq. (2.7) both initial and final state effects contribute to the observed binding energy. The initial state is just the ground state of the atom before the photoemission process. A change in the atom's initial state, for instance by the formation of chemical bonds with other atoms, will alter the binding energy of the electrons in that atom and is called an initial state effect. Final state effects are on the other hand related to the screening of the resulting core hole. For simplicity it is often assumed that initial state effects are responsible for observed chemical shifts, but in a complete analysis of the core level shifts, it is necessary to also include final state effects since they may have a significant impact on the measured binding energy [46, 56].

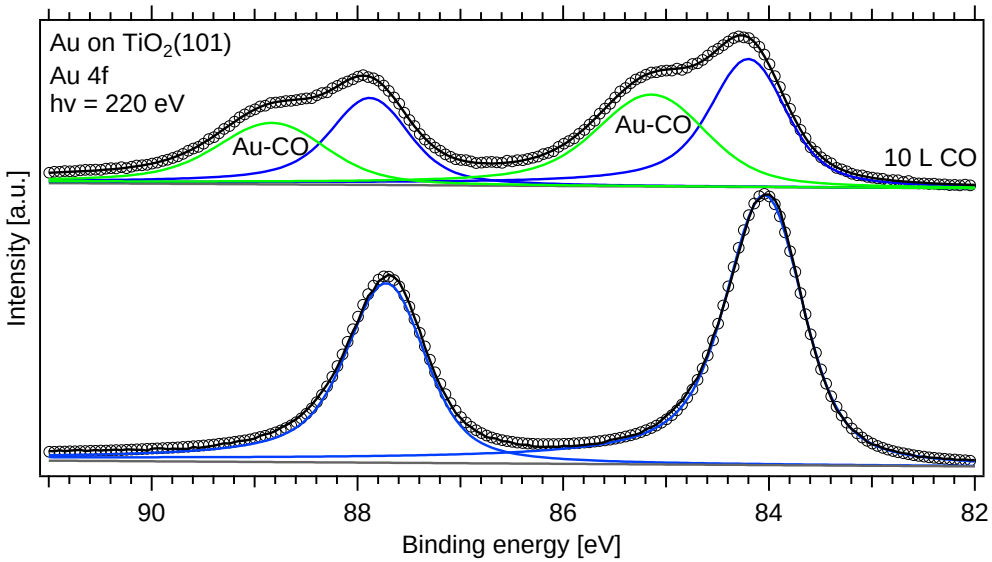

Figure 2.11: Au 4f photoemission spectra for the anatase $TiO_2(101)$ surface with 0.5 ML Au evaporated on top, before (lower spectrum) and after (upper spectrum) adsorption of 10 L CO. The chemical shifted peaks (green curves) are due to Au atoms directly bonded to CO.

2.5.4 Valence band

The valence electrons are delocalized and interact strongly with their surroundings. Due to the band structure of a solid sample, the electron density of states is usually relatively high for an extended energy interval. This makes the valence spectra complex and direct line shape analysis (see section 2.5.5) can rarely be used. Information that can be extracted from the valence band region includes band gap width, existence of filled defect states in the band gap and peaks due to adsorbates reacting with the substrate. Moreover, by performing angle resolved photoelectron spectroscopy, where both energy and angular momentum are recorded, the band structure formed by the valence electrons can be mapped out. The latter technique is not used in this thesis.

2.5.5 PES line shapes and fitting procedures

In order to extract detailed information from photoemission spectra, they have to be delineated into their individual components based on a fitting procedure.

This decomposition consists of determining binding energies, intensities and line shapes of the different contributions. For most materials, the line shape of core levels can be described by a convolution of Lorentzian and Gaussian functions, together with an asymmetry factor. Even though the energies of the core levels are well defined, the observed photoemission peaks still have a certain width due to different broadening effects.

Lorentzian contribution – lifetime broadening

The final state in the photoemission process does not have a well defined energy because of its finite lifetime. The excited state decays exponentially with time, resulting in the following relation between intensity and lifetime

$$I(t) = I(0)e^{-2\gamma t}, \tag{2.9}$$

where $t = 0$ is the time of excitation. From Heisenberg's uncertainty principle [57] it follows that this finite lifetime induces an uncertainty in the binding energy. The intensity distribution as a function of energy can be found by a Fourier transform of eq. (2.9), which gives the Lorentzian contribution to the line shape

$$I_L(E) = I_0 \frac{\gamma^2}{(E-E_0)^2 + \gamma^2}, \tag{2.10}$$

where I_0 is the intensity in the peak at $E = E_0$ and 2γ is the Lorentzian full width at half maximum (FWHM) [53].

Asymmetry – electron-hole pair excitations

Additional electrons in the sample may be excited during the photoemission process, leading to a partial energy loss for the photoelectron. In metals valence electron excitations can create electron-hole pairs within the continuum around the Fermi level contributing to this loss [58]. This affects the photoemission line shape by making it asymmetric. By combining the effect of finite lifetime with electron-hole production, Doniach and Šunjić found the following line shape [59]

$$I_{DS}(E) = I_0 \frac{\Gamma(1-\alpha)\cdot\gamma}{[(E-E_0)^2+\gamma^2]^{(1-\alpha)/2}} \cos\left[\frac{\pi\alpha}{2} + (1-\alpha)\tan^{-1}\left(\frac{E-E_0}{\gamma}\right)\right], \tag{2.11}$$

where α is the asymmetry parameter (if $\alpha = 0$ then $I_{DS} = I_L$), Γ is the gamma function and 2γ is the FWHM.

Gaussian contribution – phonon and experimental broadening

Broadening can also be caused by phonons, experimental effects such as the resolution of the electron analyser and the beamline monochromator, small unresolved chemical shifts and disorder. These effects are often assumed to give rise to Gaussian broadening, which can be described by

$$I_G(E) = I_0 e^{-\ln 2 \frac{(E-E_0)^2}{\sigma^2/4}}, \tag{2.12}$$

where σ is the Gaussian FWHM.

Fitting procedure

The photoemission spectrum also includes a background caused by inelastically scattered electrons. This background is usually subtracted from the spectrum by using a linear or Shirley [60] type function. The final line shape for each component can be found by convoluting the Doniach-Šujić function with the Gaussian contribution, giving

$$I(E) = \int_{-\infty}^{\infty} I_{DS}(E') I_G(E - E') dE'. \tag{2.13}$$

Each core level component is then described by the following parameters: intensity (I_0), binding energy (E_0), Lorentzian FWHM ($L = 2\gamma$), asymmetry factor (α) and Gaussian FWHM ($G = \sigma$). The actual fitting procedure in the present thesis has been performed using Igor [61] and FitXPS [62].

2.6 X-ray absorption spectroscopy (XAS)

X-ray absorption spectroscopy (XAS) is an experimental technique that probes the unoccupied valence states in a sample in the presence of a core hole [63]. The X-ray absorption process is shown schematically in Fig. 2.12. A photon is absorbed by an electron in a core level which is excited into an unoccupied state above the Fermi level, leaving the atom in a highly excited neutral state. A spectrum is obtained by scanning the photon energy across an absorption edge, making XAS a synchrotron based experimental method.

The absorption process can be observed by several detection schemes, including measuring the drain current, detection of fluorescent photons and detection

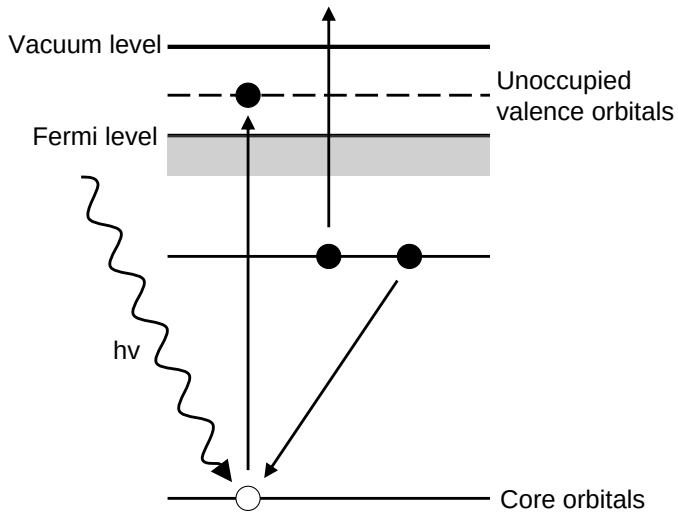

Figure 2.12: Schematic figure of the X-ray absorption process and the following decay.

of electrons. When the excited states decay, electrons will be emitted from the sample (called secondary electrons). The number of these secondary electrons is measured as a function of the photon energy. The yield is then assumed to be proportional to the probability of exciting an electron from a core level to a given energy level above the Fermi level. The XAS process is highly photon energy dependent and a peak in the XAS spectrum will be seen when the photon energy exactly matches the energy difference between the core excited final state and the ground state, given that the transitions are allowed by dipole selection rules [63].

Different modes can be used when detecting the secondary electrons: (i) Total yield, which means that all electrons (including both Auger electrons and photo-electrons) at all kinetic energies are collected. (ii) Partial yield, where a retarding voltage in front of the XAS detector is used to cut off the low kinetic energy electrons. (iii) Auger yield, where a single Auger line is measured by adjusting the energy analyzer to only accept electrons in a selected energy window. The surface sensitivity of XAS is determined by the mean free path of the emitted electrons, as well as by how many inelastically scattered electrons (i.e. electrons with lower kinetic energy) that are allowed to reach the detector. Total yield measurements are therefore most bulk sensitive, while partial and Auger yield are more surface sensitive [35, 63].

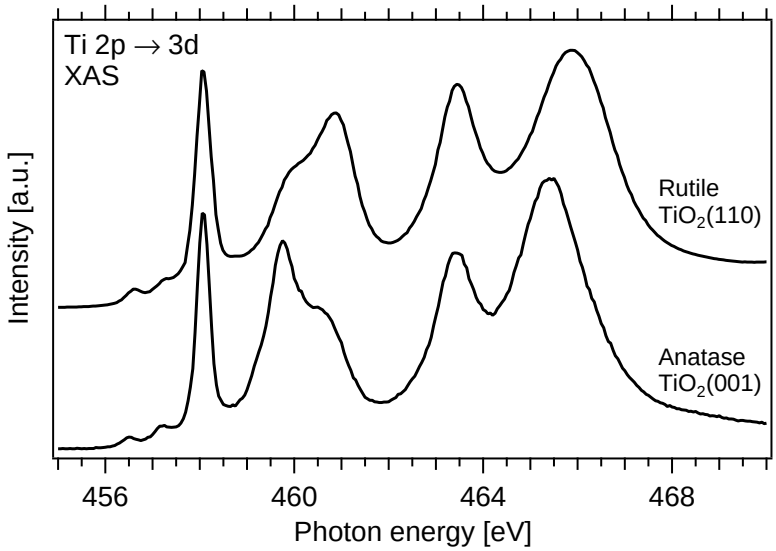

Figure 2.13: X-ray absorption spectra for the Ti L-edge (2p $\rightarrow$ 3d) of single crystal rutile $TiO_2(110)$ and anatase $TiO_2(001)$ surfaces. The Ti XAS spectrum is sensitive to the local geometry of the Ti atoms, and the relative intensities of the peaks making up the doublet feature centered at 460 eV become reversed when changing from anatase to rutile structure. The doublet is commonly assigned to e_g states, and the difference in the relative intensities between rutile and anatase is attributed to a difference in the octahedral distortion of the lattice [64, 65].

X-ray absorption spectroscopy is very useful as a fingerprint technique for determining different structural phases of materials, and also separating between crystalline and amorphous samples. In our work, we have mainly used the technique for determining the structural phase of TiO_2, by comparing with fingerprint spectra [64, 65]. Fig. 2.13 shows an example of such fingerprint spectra for single crystal anatase and rutile TiO_2 surfaces. By utilizing the polarized nature of synchrotron radiation, X-ray absorption spectroscopy can also be used as a very sensitive experimental tool for determining molecular orientation on crystal surfaces. The technique is then often called NEXAFS (near-edge X-ray absorption fine structure) [63].

2.6.1 Combining XAS and PES

By combining PES and XAS data on the same energy scale, it is possible to monitor the location of the valence and conduction band edges of the metal oxide. The

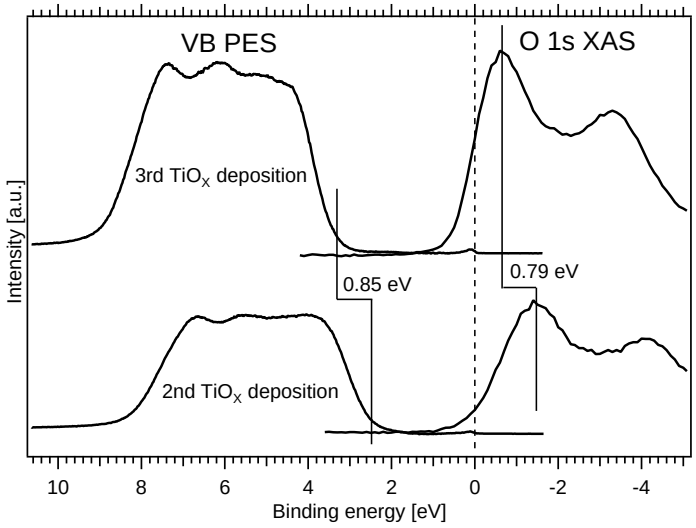

Figure 2.14: Using O 1s XAS and valence band PES spectra on the same energy scale to monitor the location of the valence and conduction band edges and to follow the band alignment during growth of TiO_x on Pt(110).

valence band is represented by the Fermi level referenced PES spectrum, while the conduction band is represented by the O 1s XAS spectrum referenced to the Fermi level by using the O 1s PES binding energy. Changes in the position of the leading peak in the O 1s XAS spectrum is expected to reflect changes in the location of the conduction band edge [66]. For TiO_2 the position of the leading peak relative the Fermi level may however be slightly offset with respect to the conduction band onset, as we find in Paper I. In Paper VI this method has been utilized to follow the band alignment during the growth of a thin TiO_x film on Pt(110), as shown in Fig. 2.14.

Chapter 3

Summary of papers

This chapter briefly summarizes the main results from the six papers included in this thesis and gives a short description of the studied systems.

3.1 The conduction-band edge of anatase TiO_2

Most of the applications of TiO_2 involve processes were electrons populate empty states in the conduction band. In the fields of photocatalysis, photovoltaics and Li ion storage [8, 11, 67, 68], anatase TiO_2 has been the primary material choice. Because the access to anatase single-crystal samples until recently has been very limited, most experimental studies have, however, been performed on the rutile phase. Previous theoretical work has shown unique electronic properties for anatase TiO_2 [69, 70]. Confirming and quantifying these theoretical findings experimentally is thus of great importance.

Paper I
Probing and modifying the empty-state threshold of anatase TiO_2: Experiments and *ab initio* theory

In this paper we use O 1s X-ray absorption spectroscopy (XAS) in conjunction with photoelectron spectroscopy to explore the conduction-band edge of single crystalline and nanostructured anatase TiO_2. The experiments are supported by *ab initio* density-functional calculations in which both the initial and core hole final states are considered. The calculations show that the states at the conduction-band

edge of anatase are of pure d_{xy} character. This is also the case in the presence of an O 1s core hole. In the O 1s XAS process, pure Ti d states cannot be probed due to selection rules. By appropriate energy referencing, the separation between the Ti d derived conduction-band edge and the threshold of the unoccupied Ti d-O p states can therefore be revealed. The electronic charge needed per Ti to eliminate this offset is discussed in quantitative terms. The theoretical and experimental values are in good agreement, showing that 4% of an electronic charge per Ti ion is sufficient to change the character of the empty states at threshold from pure Ti d to Ti d-O p.

3.2 Water adsorption on TiO_2 surfaces

Water is an integral part of the environment and the adsorption behaviour on TiO_2 is central for a wide range of applications, including photochemical water splitting, solar cells, catalysis, gas sensing and biocompatible materials [6]. After the discovery of photoinduced splitting of water into hydrogen and oxygen on a rutile TiO_2 single crystal in 1972 [9], the $H_2O/TiO_2(110)$ system has received more attention than any other comparable oxide system. The dissociation of water on the oxygen deficient $TiO_2(110)$ surface has been characterized in detail, however, there is still no consensus reached between experimentalists and theorists regarding a very fundamental question: Does water dissociate upon adsorption on the defect-free $TiO_2(110)$ surface? In Paper III we give experimental input on this important question.

The emergence of nanoscience has now put the focus on the anatase polymorph of TiO_2. Anatase is the preferred phase of TiO_2 nanoparticles [71] and is an even more potent photocatalyst compared to rutile [11]. As seen from Fig. 3.1, the equilibrium shape of an anatase crystallite exposes (101) and (001) surfaces with the latter as a minority termination. Studies of adsorption and reactivity of water on well-defined anatase surfaces can therefore be a stepping stone towards an understanding of surface processes on nanocrystalline TiO_2 in aqueous environments. In Paper II we have performed the first reported spectroscopic study of water adsorption on single crystalline anatase $TiO_2(001)$-(4×1), and in Paper IV we continue this work by doing a side-by-side comparison of the temperature dependent adsorption state of water on the anatase $TiO_2(101)$-(1×1) and (001)-(4×1) surfaces.

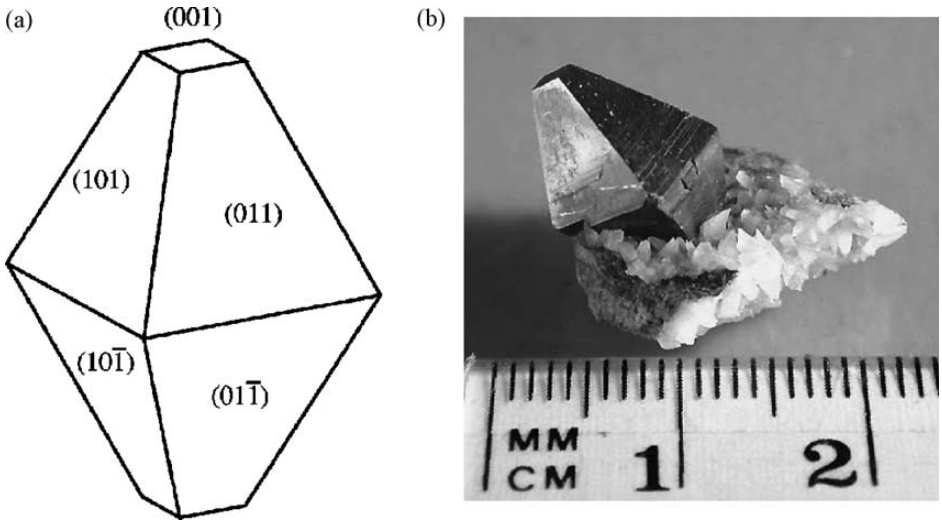

Figure 3.1: (a) The calculated equilibrium shape of an anatase TiO_2 crystal [19]. (b) Picture of an anatase mineral crystal. The figure is taken from [6].

Paper II
Water Dissociation on Single Crystalline Anatase TiO_2(001) Studied by Photoelectron Spectroscopy

Here we study the adsorption of water on the anatase TiO_2(001)-(4×1) surface using synchrotron radiation-excited core level photoelectron spectroscopy. The coverage dependent adsorption of water at low temperature is monitored and compared to the sequence obtained after heating of a water multilayer. Two adsorption phases of submonolayer coverage can be defined: Phase 1 consists only of dissociated water, observed as OH-groups. This phase is found at low coverage at low temperature (190 K) and is the only state of adsorbed water above $\sim$230 K. The saturation coverage of phase 1 is consistent with dissociation on the 4-fold-coordinated Ti ridge atoms of the (4×1) surface reconstruction. The high reactivity and the location of the hydroxyl groups confirm previous theoretical predictions. Phase 2 is found at higher coverage, reached at lower temperature. It consists of a mixture of dissociated and molecular water with a ratio of 1:1 at 170 K. The molecular water is found to bond to the hydroxyl groups. The hydroxyl coverage of phase 2 is approximately 2 times that of phase 1. The results suggest that the OH and H_2O species of phase 2 are confined to the ridges of the surface.

Paper III
Experimental evidence for mixed dissociative and molecular adsorption of water on a rutile TiO_2(110) surface without oxygen vacancies

In this paper we present a study of the interaction of water with the rutile TiO_2(110) surface using synchrotron radiation photoemission spectroscopy. We demonstrate that O 1s spectra recorded at grazing emission angle at optimized photon energy in conjunction with valence spectra allow for the observation of OH on the surface in the presence of substrate oxygen. We present clear evidence for mixed molecular and dissociate water adsorption, with a OH:H_2O ratio close to 0.5, at monolayer coverage on a TiO_2(110) surface free from oxygen vacancies. Reducing the coverage by heating of the monolayer results in an increased OH:H_2O ratio. Importantly, neither species originating from the monolayer on the defect free surface are detected at room temperature. This demonstrates that OH in the mixed monolayer is much less stable than OH formed at oxygen vacancies. The detailed nature of OH in the mixed layer is not possible to unveil with present experimental results but they are clearly consistent with the notion of pseudo-dissociated water on the vacancy free surface.

Paper IV
Mixed dissociative and molecular water adsorption on single crystal anatase TiO_2 surfaces studied by core level photoemission spectroscopy

In this study, we make a side-by-side comparison of the temperature dependent adsorption state of water on the (101)-(1×1) and (001)-(4×1) surfaces of anatase TiO_2. Using extremely surface sensitive synchrotron radiation excited O 1s photoemission spectra, we demonstrate that the formation of a water monolayer on the anatase TiO_2(101) surface involves both associative and dissociative adsorption. The behaviour is similar to that on rutile TiO_2(110) and illustrates the importance of intermolecular interactions present at higher coverages. The exact composition of the monolayer on the anatase TiO_2(101) is however difficult to deduce due to simultaneous desorption of first and second layer water. We also continue the discussion on the nature of the water layer on the (001) surface. Dissociation occurs on the ridges of the (4×1) reconstruction, while a mixture of molecular and dissociated water is formed either in connection to the ridges or on the terraces. Due to the high complexity of the surface a clear assignment of the location of all the OH groups is however not possible.

3.3 Submonolayer growth of Au on the anatase TiO_2(101) surface

Even though gold for a long time was regarded as an inert material when it came to catalysis, gold nanoparticles supported on metal oxides have recently been found to be effective catalysts for several processes, including CO oxidation at remarkably low temperatures [72]. There is also a strong size dependence, particles below 5 nm in size are far superior to larger particles in terms of catalytic activity [73]. Even though the Au/TiO_2 system has been heavily investigated, primarily on the rutile phase, the mechanism behind the CO oxidation process is still not well understood. Anatase TiO_2 is the preferred phase when forming nanosized particles [71] and model studies of Au on single crystalline anatase TiO_2 are therefore of strong relevance.

Paper V
Growth of Au on Single Crystalline Anatase TiO_2(101): Formation of oxidized gold

We have used synchrotron based core level photoelectron spectroscopy to study submonolayer growth of gold and its interaction with CO on the anatase TiO_2(101) surface. Here we observe two different Au species forming. The first type is characterized by an Au $4f_{7/2}$ binding energy of 84.8 ± 0.1 eV and a CO induced shift of 1.5 eV. This type of particles is only discerned up to an Au coverage of 0.14 ML and appears to be size-limited. It also has a constant relative CO uptake. The second particle type has an Au $4f_{7/2}$ binding energy of 84.1 ± 0.1 eV and a CO induced shift of 0.9 eV. It is first observed at 0.14 ML and continues to grow at higher Au coverages, exhibiting a decreasing relative CO uptake with increasing Au dose, which is typical for an increasing particle size. We propose that the first particle type contains oxidized gold and the low coverage suggests nucleation at defects, possibly oxygen ad-atoms located on the terraces. The oxidized gold aggregates appear to be size-limited. The second type is attributed to neutral gold that most likely nucleate at steps on the anatase TiO_2(101) surface. For the second particle type, we have used the CO uptake to estimate the particle size. Here we find an average particle size of 2 nm for the 0.4 ML Au coverage, while after an Au dose of 1 ML, the particles typically have a size of 3.5 nm.

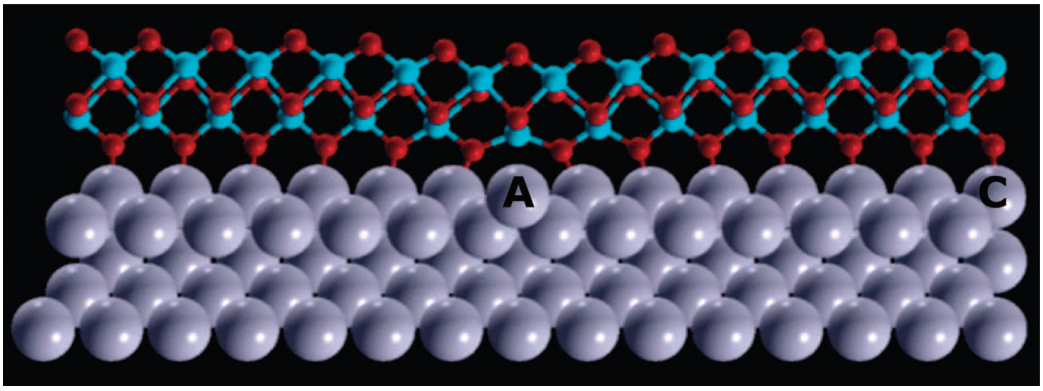

Figure 3.2: A suggested model of the TiO_x bilayer on Pt(110). The red and blue balls are oxygen and titanium, respectively. The figure is taken from [78].

3.4 Thin TiO_x films on Pt(110)

Remarkable properties of nanostructured titania, in the form of nanosheets, nanotubes, nanorods and nanoclusters, have recently been reported [74, 75]. Several of these new phases do not have a bulk counterpart and their properties are closely related to surface structure and interface effects. Titania nanosheets are thought to be the building blocks of titania nanotubes and nanorods, calling for careful investigations of their physical and structural properties. Additionally, a TiO_x double layer can be assembled on Pt(110) and Pt(111) surfaces with a geometric structure similar to that found for unsupported TiO_2 nanosheets [76–78]. Studying such ultrathin films on a single crystal metal support can serve both as a nanosheet model as well as a new material in its own right. Its properties are determined by the combination of the oxide film properties and those of the support. Fig. 3.2 shows a suggested model of the TiO_x bilayer on Pt(110).

Paper VI
Growth of ultrathin TiO_x films on Pt(110) studied by high resolution photoemission and X-ray absorption spectroscopy

In this paper we utilize high resolution photoemission and X-ray absorption spectroscopy to study the formation of an ultrathin TiO_x film on the Pt(110)-(1×2) reconstructed surface. From Ti 2p XAS spectra of the deposited TiO_x film a structural change from a rutile-like structure when TiO_x coexists with PtO_2 to an anatase-like structure upon completion of a TiO_x bilayer on the Pt surface is

observed. Upon comparison to an anatase TiO_2(001) single crystal, the complete TiO_x bilayer displays a very similar band alignment with respect to the Fermi level, but with a band gap that is 0.2 eV lower. In contrast, a rigid shift of -0.8 eV is found for the electronic states of the bilayer islands. This shift can be explained in terms of a band bending effect imposed by the PtO_2 patches.

Bibliography

[1] R. P. Feynman, *There's Plenty of Room at the Bottom* (1959), `http://www.its.caltech.edu/~feynman/plenty.html`.

[2] D. P. Woodruff and T. A. Delchar, *Modern techniques of Surface Science*, 2nd ed. (Cambridge University Press, Cambridge, 1994).

[3] A. Zangwill, *Physics at Surfaces* (Cambridge University Press, Cambridge, 1988).

[4] K. W. Kolasinski, *Surface Science: Foundations of Catalysis and Nanoscience* (Wiley, 2002).

[5] G. A. Somorjai, *Introduction to Surface Chemistry and Catalysis* (Wiley, 1994).

[6] U. Diebold, Surf. Sci. Rep. **48**, 53 (2003), and references therein.

[7] U. Diebold, Appl. Phys. A **76**, 681 (2003).

[8] B. O'Regan and M. Grätzel, Nature **353**, 737 (1991).

[9] A. Fujishima and K. Honda, Nature **37**, 238 (1972).

[10] M. Ni, M. K. H. Leung, D. Y. C. Leung and K. Sumathy, Renewable and Sustainable Energy Rev. **11**, 401 (2007).

[11] A. L. Linsebigler, G. Lu and J. T. Yates Jr., Chem. Rev. **95**, 735 (1995).

[12] Wikipedia, `http://www.wikipedia.org`.

[13] H. Zhang and J. F. Banfield, J. Mater. Chem. **8**, 2073 (1998).

[14] J. M. G. Amores, V. S. Escribano and G. Busca, J. Mater. Chem **5**, 1245 (1995).

[15] G. Charlton, P. B. Howes, C. L. Nicklin, P. Steadman, J. S. G. Taylor, C. A. Muryn, S. P. Harte, J. Mercer, R. McGrath, D. Norman, T. S. Turner and G. Thornton, Phys. Rev. Lett. **78**, 495 (1997).

[16] W. Hebenstreit, N. Ruzycki, G. S. Herman, Y. Gao and U. Diebold, Phys. Rev. B **62**, R16334 (2000).

[17] G. S. Herman, M. R. Sievers and Y. Gao, Phys. Rev. Lett. **84**, 3354 (2000).

[18] Y. Liang, Y. Gan, S. A. Chambers and E. I. Altman, Phys. Rev. B **63**, 235402 (2001).

[19] M. Lazzeri and A. Selloni, Phys. Rev. Lett. **87**, 266105 (2001).

[20] R. E. Tanner, A. Sasahara, Y. Liang, E. I. Altman and H. Onishi, J. Phys. Chem. B **106**, 8211 (2002).

[21] X.-Q. Gong, A. Selloni, O. Dulub, P. Jacobson and U. Diebold, J. Am. Chem. Soc. **130**, 370 (2008).

[22] M. Zeilik and S. A. Gregory, *Introductory Astronomy & Astrophysics* (Saunders College publishing, 1998).

[23] J. F. O'Hanlon, *A User's Guide to Vacuum Technology* (Wiley, 2003).

[24] H. Lüth, *Solid Surfaces, Interfaces and Thin Films* (Springer, 2001).

[25] G. Sauerbrey, Z. Phys. **155**, 206 (1959).

[26] P. Hofmann, *Lecture Notes on Surface Science*, `http://www.philiphofmann.net/surflec/surflec.html`.

[27] J. J. Brehm and W. J. Mullin, *Introduction to the structure of matter* (John Wiley & Sons, 1989).

[28] C. Davisson and L. H. Germer, Nature **119**, 558 (1927).

[29] C. Davisson and L. H. Germer, Phys. Rev. **30**, 705 (1927).

[30] E. J. Schreiber, L. H. Germer and C. D. Harman, Rev. Sci. Instrum. **31**, 112 (1960).

[31] M. A. van Hove, W. H. Weinberg and C.-M. Chan, *Low-Energy Electron Diffraction. Experiment, Theory and Surface Structure Determinations* (Springer, 1986).

[32] L. J. Clarke, *Surface Crystallography: An Introduction to Low Energy Electron Diffraction* (John Wiley & Sons, 1985).

[33] R. L. Park and H. H. Jr. Madden, Surf. Sci. **11**, 188 (1968).

[34] E. A. Wood, J. Appl. Phys **35**, 1306 (1964).

[35] S. Raaen, *Lecture notes on Electron spectroscopy* (Lecture notes, NTNU, 2006)

[36] G. Margaritondo, *Introduction to Synchrotron Radiation* (Oxford University Press, 1988).

[37] J. D. Jackson, *Classical Electrodynamics* (Wiley, Ney York, 1998).

[38] D. Attwood, *Soft X-Rays and Extreme Ultraviolet Radiation* (Cambridge University Press, 1999).

[39] Homepage of HASYLAB at DESY, `http://hasylab.desy.de`.

[40] Lecture notes in *Synchrotron Radiation for Materials Science Applications*, University of California, Berkeley, `http://www.coe.berkeley.edu/AST/srms`.

[41] MAX-lab homepage, `http://www.maxlab.lu.se`.

[42] Å. Andersson, M. Eriksson, L.-J. Lindgren, P. Röjsel and S. Werin, Rev. Sci. Instrum. **66**, 1850 (1995).

[43] J. N. Andersen, O. Björneholm, A. Sandell, R. Nyholm, J. Forsell, L. Thånell, A. Nilsson and N. Mårtensson, Synchrotron Rad. News **4**, 15 (1991).

[44] R. Nyholm, J. N. Andersen, U. Johansson, B. N. Jensen and I. Lindau, Nucl. Instr. and Meth. in Phys. Res. A **467-468**, 520 (2001).

[45] Homepage of Beamline D1011, MAX-lab, `http://www.maxlab.lu.se/beamlines/bld1011`.

[46] S. Hüfner, *Photoelectron Spectroscopy: Principles and Applications* (Springer, 2003).

[47] H. Hertz, Ann. Physik **267**, 983 (1887).

[48] A. Einstein, Ann. Physik **322**, 132 (1905).

[49] K. Siegbah, C. Nordling, A. Fahlmann, R. Nordberg, K. Hamin, J. Hedman, G. Johansson, T. Bergmark, S. Karlsson, I. Lindgren and B. Lingberg, *ESCA: atomic, molecular and solid state structure studied by means of electron spectroscopy* (Almqvist and Wiksells, Uppsala, 1967).

[50] The homepage of VG Scienta, `http://www.vgscienta.com`.

[51] I.-H. Svenum, *Interactions of Functional Groups with Surfaces*, PhD thesis (NTNU, Trondheim, 2009).

[52] F. Reinert and S. Hüfner, New J. Phys. **7**, 97 (2005).

[53] J. N. Andersen and C.-O. Almbladh, J. Phys.: Condens. Matter **13**, 11267 (2001).

[54] S. Hagström, C. Nordling and K. Siegbahn, Phys. Lett. **9**, 235 (1964).

[55] B. Johansson and N. Mårtensson, Phys. Rev. B **21**, 4427 (1980).

[56] J. C. Vickerman and I. S. Gilmore, *Surface Analysis - The Principal Techniques* (Wiley, 2009).

[57] R. Shankar, *Principles of quantum mechanics*, 2nd ed. (Springer, 1994).

[58] D. C. Langreth, Phys. Rev. Lett. **54**, 126 (1985).

[59] S. Doniach and M. Šunjić, J. Phys. C **3**, 285 (1970).

[60] D. A. Shirley, Phys. Rev. B **5**, 4709 (1972).

[61] Igor Pro, WaveMetrics, `http://www.wavemetrics.com`.

[62] FitXPS is written by David Adams, University of Aarhus, and can be downloaded from: `http://www.sljus.lu.se/download.html`.

[63] J. Stöhr, *NEXAFS Spectroscopy* (Springer, 2003).

[64] F. M. F. de Groot, M. O. Figueiredo, M. J. Basto, M. Abbate, H. Petersen and J. C. Fuggle, Phys. Chem. Miner. **19**, 140 (1992).

[65] R. Ruus, A. Kikas, A. Saar, A. Ausmees, E. Nõmmiste, J. Aarik, A. Aidla, T. Uustare and I. Martinson, Solid State Commun. **104**, 199 (1997).

[66] A. Sandell, P. G. Karlsson, J. H. Richter, J. Blomquist, P. Uvdal and T. M. Grehk, Appl. Phys. Lett. **88**, 132905 (2006).

[67] J. H. Richter, A. Henningsson, B. Sanyal, P. G. Karlsson, M. P. Andersson, P. Uvdal, H. Siegbahn, O. Eriksson and A. Sandell, Phys. Rev. B **71**, 235419 (2005).

[68] J. Osorio-Guillén, S. Lany and A. Zunger, Phys. Rev. Lett. **100**, 036601 (2008).

[69] R. Asahi, Y. Taga, W. Mannstadt and A. J. Freeman, Phys. Rev. B **61**, 7459 (2000).

[70] M. V. Koudriachova, S. W. de Leeuw and N. M. Harrison, Phys. Rev. B **69**, 054106 (2004).

[71] C. J. Taylor, D. C. Gilmer, D. G. Colombo, G. D. Wilk, S. A. Campbell, J. Roberts and W. L. Gladfelter, J. Am. Chem. Soc. **121**, 5220 (1999).

[72] M. Haruta, N. Yamada, T. Kobayashi and S. Iijima, J. Catal. **115**, 301 (1989).

[73] M. Valden, X. Lai and D. W. Goodman, Science **281**, 1647 (1998).

[74] X. Chen and S. S. Mao, Chem. Rev. **107**, 2891 (2007).

[75] D. V. Bavykin, J. M. Friedrich and F. C. Walsh, Adv. Mater. **18**, 2807 (2006).

[76] Y. Zhang, L. Giordano, G. Pacchioni, A. Vittadini, F. Sedona, P. Finetti and G. Granozzi, Surf. Sci. **601**, 3488 (2007).

[77] T. Orzali, M. Casarin, G. Granozzi, M. Sambi and A. Vittadini, Phys. Rev. Lett. **97**, 156101 (2006).

[78] S. Agnoli, T. Orzali, M. Sambi, A. Vittadini, M. Casarin and G. Granozzi, J. Phys. Chem. C **112**, 20038 (2008).

Part II

Papers

Paper I

Probing and modifying the empty-state threshold of anatase TiO_2: Experiments and ab initio theory

A. Sandell, B. Sanyal, L. E. Walle, J. H. Richter, S. Plogmaker, P. G. Karlsson, A. Borg and P. Uvdal

Physical Review B **78**, 075113 (2008).

Probing and modifying the empty-state threshold of anatase TiO_2: Experiments and *ab initio* theory

A. Sandell,[1,*] B. Sanyal,[1] L. E. Walle,[2] J. H. Richter,[1] S. Plogmaker,[1] P. G. Karlsson,[1] A. Borg,[2] and P. Uvdal[3]
[1]*Department of Physics and Materials Science, Uppsala University, P.O. Box 530, SE-751 21 Uppsala, Sweden*
[2]*Department of Physics, Norwegian University of Science and Technology, NO-7491 Trondheim, Norway*
[3]*Chemical Physics, Department of Chemistry, Lund University, P.O. Box 124, SE-221 00 Lund, Sweden*
(Received 3 April 2008; revised manuscript received 17 June 2008; published 18 August 2008)

O 1*s* x-ray absorption spectroscopy (XAS) in conjunction with photoelectron spectroscopy has been used to explore the conduction-band edge of single crystalline and nanostructured anatase TiO_2. The experiments are supported by *ab initio* density-functional calculations in which both the initial and core hole final states are considered. The calculations show that the states at the conduction-band edge of anatase are of pure d_{xy} character. This is also the case in the presence of an O 1*s* core hole. In the O 1*s* XAS process pure Ti *d* states cannot be probed and, by appropriate energy referencing, the separation between the Ti *d* derived conduction-band edge and the threshold of the unoccupied Ti $d-O\ p$ states can therefore be revealed. The electronic charge needed per Ti to eliminate this offset is discussed in quantitative terms. The theoretical and experimental values are in good agreement, showing that $4\pm2\%$ of an electronic charge per Ti ion is sufficient to change the character of the empty states at threshold from pure Ti *d* to Ti $d-O\ p$.

DOI: 10.1103/PhysRevB.78.075113 PACS number(s): 71.20.−b, 73.20.At, 79.60.Bm, 78.70.Dm

I. INTRODUCTION

TiO_2 is a material with a wide range of applications in many different technical areas. It is important within the fields of gas sensors, biocompatible materials, energy storage, photovoltaics, and photocatalysis.[1–4] Most of these applications involve processes where electrons populate empty states in the conduction band. Within the dye sensitized solar cell the first step is light absorption by the dye molecule upon which the excited electron is injected into the TiO_2 conduction band.[5] The key step in photocatalysis is the separation of photoinduced charge carriers.[1,2] Subsequent transfer of holes and electrons between the TiO_2 substrate and the adsorbed molecules govern the surface reactions. Examples of chemical modifications that lead to the population of conduction-band states are Li ion insertion and creation of defects in the form of oxygen vacancies.[3,6–10] Doping of TiO_2 with other transition metals is a modification that has attracted enormous interest recently.[11,12] This largely stems from the prospect of preparing dilute magnetic semiconductors (DMSs) for use in spintronic applications. Whether transition metal doped TiO_2 qualifies as a true DMS is heavily disputed. Still, the system poses many interesting fundamental questions, such as the influence of defects on the magnetic coupling between the dopants.

Anatase TiO_2 is the structural phase that has been the primary choice for applications within the fields of photocatalysis, photovoltaics, and Li ion storage.[1–4,6] Previous theoretical work has revealed ground-state electronic properties unique for the anatase phase of TiO_2.[13] The states at the conduction-band minimum (CBM) are of pure Ti d_{xy} character with the Ti $d-O\ p$ mixed states clearly separated from the CBM. This separation is much less pronounced for rutile TiO_2. A considerable optical anisotropy found for anatase was related to the offset between the *d* and *p* thresholds.[13] A transition from the nonbonding p_π states (located at the top of the valence band) to the d_{xy} states is dipole forbidden for the $E\|c$ polarization while it is allowed for the $E\perp c$ polarization. In a theoretical study on the effects of Li insertion in anatase TiO_2 it was furthermore shown that the donated electrons first populate d_{xy} states.[14] At higher *d* populations Ti d_{xz} and d_{yz} states mixed with O *p* states become populated. The orthorhombic distortion of the lattice observed experimentally[15] is not initiated until the Ti d_{yz} states become populated.[14]

Based on the theoretical studies described above it can be concluded that Ti $d-O\ p$ mixed states become degenerate with the empty states threshold only above a critical population of the d_{xy} states. This point may define: (i) a change in the transport properties of photoexcited or injected electrons, (ii) a change in the optical properties, and (iii) the onset for geometric changes. Confirming and quantifying these intriguing theoretical findings experimentally is a very important objective. The optimal way to do this is by acquiring high quality experimental data for single-crystal anatase samples. Up to date, the access to anatase single-crystal samples has been very limited. This is in stark contrast to the case of rutile TiO_2 where single crystals of various surface terminations have been readily available for a long time. For this reason rutile TiO_2 has been established as the benchmark metal oxide.

Very recently, studies on the electronic properties of anatase single crystals have started to appear. This allows for fundamental studies of the TiO_2 polymorph primarily used in applications. The results obtained for anatase also serves as the most important complement to the numerous studies of the rutile phase. For example, photoelectron spectroscopy (PES) in a resonant mode has been used to probe the character of the valence band, and important differences between rutile and anatase were highlighted.[16] A significant optical anisotropy has furthermore been found for single-crystal anatase TiO_2.[17] The $E\perp c$ oscillator strength near the absorption edge was found to be one orders of magnitude larger than for $E\|c$. The $E\|c$ and $E\perp c$ absorption edges were assigned to

be direct and indirect optical absorption processes, respectively. This is fully consistent with the theoretical calculations.[13]

In this paper, we use O 1*s* x-ray absorption spectroscopy (XAS) in conjunction with PES to explore the conduction-band edge of single crystalline anatase TiO_2. The experiments are supported by *ab initio* density-functional calculations in which both the initial and core hole final states are considered. We demonstrate that appropriately energy referenced O 1*s* PES and XAS spectra confirm the theoretically predicted separation between the CBM and the Ti 3*d* −O 2*p* mixed states. We furthermore quantify the electronic charge needed per Ti to eliminate this offset, thereby changing the character of the empty states at threshold from pure Ti *d* to Ti *d*−O *p*.

II. EXPERIMENT

The spectra were recorded at the beamlines D1011 and I311 at the Swedish national synchrotron facility MAX II.[18] The end stations at both beamlines comprise a Scienta 200 mm radius hemispherical electron energy analyzer. Binding-energy (BE) calibration was made relative to the Fermi level of a platinum foil mounted on the sample holder. The x-ray absorption spectra were calibrated by the recording of a PES peak excited with first-order and second-order light from the monochromator. The anatase TiO_2 (001) and (101) single crystals (supplied by PI-KEM Ltd., U.K.) were cleaned by cycles of Ar sputtering and subsequent annealing in oxygen to 650 °C. The preparation and characterization of the pristine and Li-modified nanostructured anatase TiO_2 films have been discussed in detail elsewhere.[19,20]

III. CALCULATIONS

Ab initio calculations have been performed by a plane-wave code (VASP) (Ref. 21) within density-functional theory (DFT). A projector augmented wave (PAW) (Ref. 22) basis is used in the local-density approximation (LDA) with Ceperley and Alder exchange-correlation functional parametrized by Perdew and Zunger. We have used a kinetic-energy cutoff of 450 eV for the plane waves included in the basis set. For Brillouin zone integration, *k* points were generated in the Monkhorst Pack scheme. The local density of states (DOS) was calculated by projecting the wave functions onto spherical harmonics. To simulate the final-state effects in the presence of a core hole, we used the $Z+1$ approximation where an impurity with atomic number $Z+1$ is substituted in place of the atom (with atomic number Z), for which spectroscopic measurement is done. For this purpose, we have used the supercell of a $3\times3\times3$ geometry and have placed an F impurity atom in the place of an O atom. The calculations have been done for the anatase phase of TiO_2. The lattice parameters and atomic coordinates were extracted from the experimental results in the literature. The DOS is artificially broadened by a Gaussian function with a full width at half maximum (FWHM) of 0.2 eV.

IV. RESULTS AND DISCUSSION

Figure 1 shows occupied valence electronic states as probed by PES. Clear changes are observed in the valence band depending on the surface studied in line with previous work.[16] An important property is the location of the valence-band edge (VBE). Qualitatively, the results displayed in Fig. 1 suggest that the VBE of the (101) surface is located at a slightly higher BE than that of the (001) surface. DOS calculations show that the VBE of anatase is very sharp.[13] Consequently, the broadening in the experimentally measured VBE is at the present resolution (about 60 meV) dominated by phonons. Fitting of a Gaussian curve therefore yields an estimate of the location of the DOS VBE. These are indicated in Fig. 1. The VBE can also be estimated by use of a linear approach as described in Ref. 23. In the case of semiconductors and metal oxides a common approach is furthermore to assume that the shifts in the VBE position are traced by the BE shifts of the core-level peaks.[24] Since core-level peaks are better defined than the valence band, a more accurate measure of relative shifts of the VBE is provided. In the present case, we have monitored the BE shifts of the Ti 2*p* (4+) and O 1*s* peaks. After applying all three methods described above we estimate that the VBE of the (101) surface is located 0.15 ± 0.05 eV above that of the (001) surface.

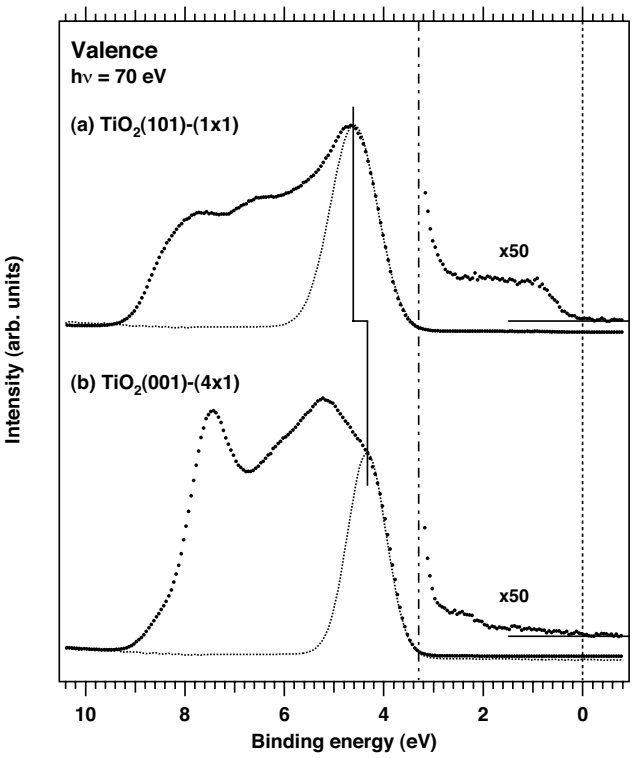

FIG. 1. Valence-band electronic states for (a) TiO_2(101)-(1x1) and (b) TiO_2(001)-(4x1) in the anatase phase. The energy scale is relative to the sample holder Fermi level (dashed line). The Gaussian peaks (dotted) represent the edges of the DOS. The vertical dashed dotted line indicates the experimentally determined optical band gap (Ref. 25) assuming an alignment of the conduction-band edge to the Fermi level.

The binding energy of the VBE relative to the Fermi level is expected to increase upon the population of Ti 3*d* states. It is known that Ti 3*d* states become populated when defects in the form of oxygen vacancies occur, that is, Ti^{3+} states are formed. The (101) surface is more prone to defect formation

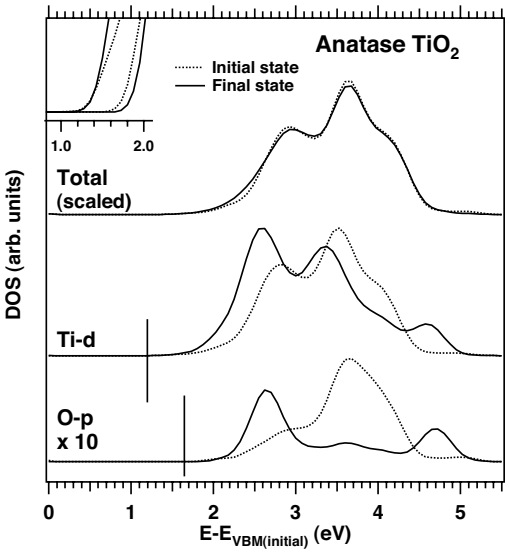

FIG. 2. Total (for the entire unit cell with s, p, and d electrons) and partial (projected on an atom with particular orbital character) density of states for anatase TiO_2 obtained by *ab initio* calculations. The energy scale is relative to the valence-band maximum of the initial state. Dashed lines: DOS curves for the initial state. Solid lines: DOS curves for the final state with an O 1s core hole present. The total density of states is scaled in order to facilitate a comparison. As indicated, the O-p DOS is comparable to the Ti-d DOS if divided by a factor of ten. The Ti-d and O-2p onsets of the final states are marked with vertical solid lines. The inset shows a magnified view of the different Ti-d and O-2p onsets for anatase.

than the (001) surface as pointed out previously.[16] A weak Ti 3d related feature at 1 eV BE is indeed observed for the (101) surface, while no Ti 3d state can be discerned for the (001) surface. (It can be noted that both spectra exhibit a much lower defect density than those previously reported.) By normalizing to a sputtered and annealed surface where reduced states are clearly visible in the Ti 2p spectrum, it was possible to estimate the Ti^{3+} density to $1.0 \pm 0.5\%$ per Ti ion for the (101) surface. (The difficulty in defining the background is the major cause of a rather large error.) The presence of a Ti 3d feature is consistent with the positive binding-energy shift of the VBE for the (101) surface when compared with the (001) surface.

Most important for the analysis is to determine the location of the CBM. There are two observations that suggest that the CBM is well aligned to the Fermi-level reference. First, the expanded spectra show populated band-gap states reaching up to a point that coincides with the Fermi level (Fig. 1). Second, the band gap of anatase TiO_2 is reported to be
3.3 eV.[25] When taking this value relative to the Fermi level (dashed dotted line in Fig. 1), the position agrees very well with the low BE onset of the valence band. Thus, the energy difference between the VBE and the Fermi level agrees very well with the band-gap energy given by optical absorption.

Figure 2 shows the calculated unoccupied DOS for anatase TiO_2. The curves for the initial and final states are included, aligned against the VBE of the initial state. The partial DOS curves show clearly that the unoccupied states in this energy region are predominantly of Ti 3d character with a small admixture of O 2p. The states closest to the CBM are however of pure Ti 3d character. The ground-state calculations presented are in very good agreement with previous work.[13] The final-state DOS reveal significant effects upon the formation of an O 1s core hole. The weight of the Ti 3d DOS and O 2p DOS moves closer to threshold and the integrated O 2p DOS decreases. An increased population of the O 2p states is expected given that the final state can be envisaged as a fluorine ion according to the $Z+1$ approximation. Most important, however, is that the offset between the Ti 3d DOS and the O 2p onsets is retained. The offset between the Ti 3d DOS and the O 2p onsets amounts to 0.45 eV. The spatial distribution of the states at the CBM confirms that these are made up of nonbonding Ti $3d_{xy}$ states (not shown).

The fact that the offset is retained in the presence of an O 1s hole strongly suggests that it is present also upon the formation of a hole in the valence band. This lends strong support for the interpretation that the large optical dichroism is correlated with the existence of nonbonding d_{xy} states at the bottom of the conduction band.[13]

That the offset is present upon the creation of an O 1s hole justifies furthermore the use of O 1s XAS to probe the properties of the empty states threshold. The symmetry condition and the strong core hole localization leads to population of states of predominantly O p character in the O 1s XAS process.[26] Hence pure Ti d states cannot be probed and a central issue is therefore to determine the position of the CBM in the O 1s XAS spectrum. This can be accomplished by a comparison with the O 1s PES spectrum. Figures 3(a) and 3(b) show O 1s XAS and PES spectra for anatase (001) and (101), respectively. The XAS and PES spectra are placed on a common energy scale. The energy values of the PES spectra are relative to the Fermi level, whereas the energy values of the XAS spectra correspond to the absolute photon energy. The spectra are normalized as to have the same peak height. The final-state calculations show an unoccupied O p DOS that is sharp at threshold. Together with additional dynamical effects[27] this results in nearly identical shapes of the XAS edge and the low BE side of the O 1s PES line.[28] That is, the shape of the XAS threshold is predominantly influenced by phonon excitations, similar to the VBE. Consequently, the DOS threshold is given by the position of the leading XAS peak.[27,28] With this in mind it stands clear from Figs. 3(a) and 3(b) that the DOS threshold as probed by O 1s XAS is well separated from the Fermi level for both surfaces. This separation is associated with the aforementioned offset between the pure d states at the CBM and the p-d states reachable in the O 1s XAS process. The offset is 0.6 ± 0.1eV for the (001) surface and 0.4 ± 0.1eV for the (101) surface. The difference in the offset furthermore matches the difference in the VBE location very well, which suggests a rigid shift of the electronic levels.

The nanostructured anatase TiO_2 film provides very important information on the O p-CBM offset since the Ti d population can be increased in a controlled fashion by Li insertion. Insertion of lithium leads to electron donation from the Li 2s orbital to Ti 3d states.[9,14,29] As a result, the gap between the CBM and the O 2p empty DOS is expected to

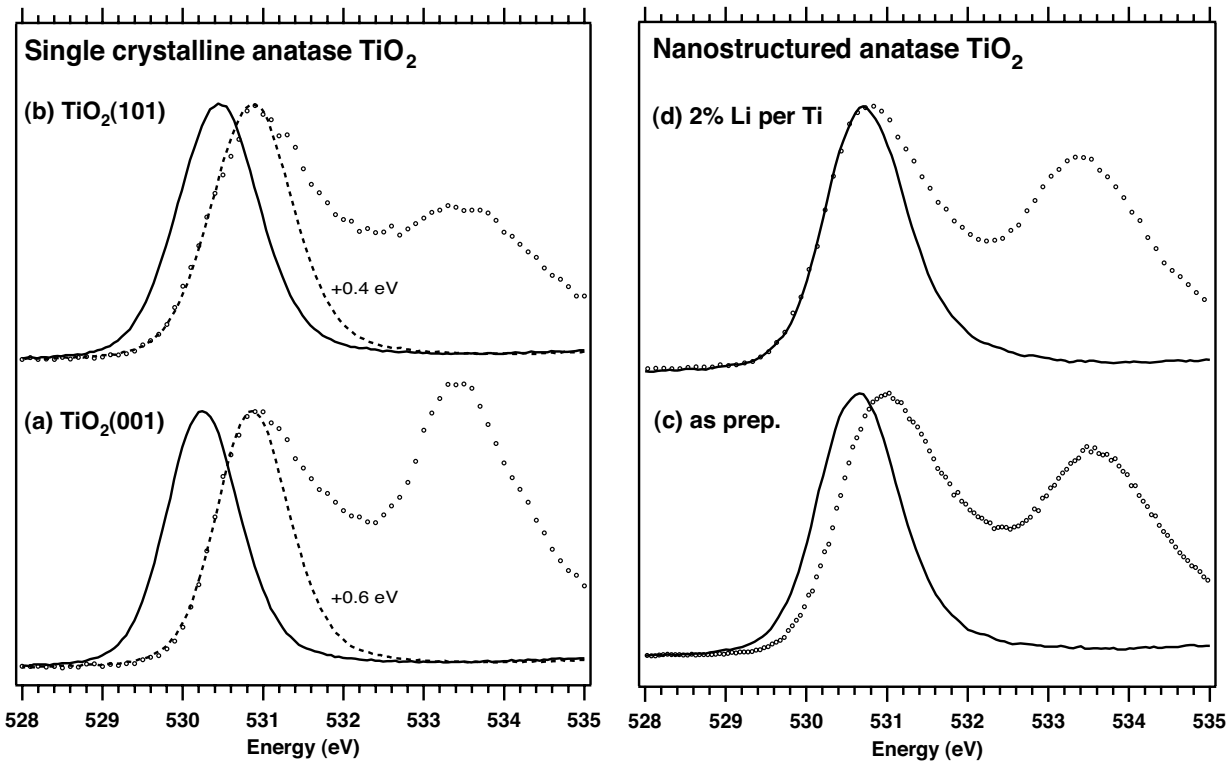

FIG. 3. O 1*s* XAS and PES spectra for anatase (a) TiO_2(001)-(4x1) and (b) TiO_2(101)-(1x1) on a common energy scale. The energy values of the PES spectra are relative to the Fermi level, whereas the energy values of the XAS spectra correspond to the absolute photon energy. The spectra are normalized as to have the same peak height. A clear separation between the XAS and PES peaks are observed for both surfaces with a smaller separation noted for the (101) surface. (c) The same comparison for an as-prepared nanostructured anatase film also reveals an XAS–PES separation. As shown in (d), this offset can be eliminated by the insertion of small amounts of lithium.

decrease. At sufficient Li concentration the O 2*p* DOS threshold will become degenerate with the empty states threshold.

The valence spectra before and after insertion of Li are shown in Fig. 4. The as-prepared film exhibits a small Ti 3*d* peak at 1 eV BE due to defects. Upon insertion of 2% Li per Ti ion the intensity of the Ti 3*d* state increases significantly and the valence band shifts toward higher BE. The O 1*s* PES-XAS relationship for the as-prepared nanostructured anatase film is qualitatively similar to the single-crystal surfaces. Figure 3(c) shows that the binding energy of the O 1*s* PES line relative to the Fermi level is about 0.3 eV lower than the photon energy of the XAS peak. Figure 3(d) shows that the PES-XAS offset for the as-prepared anatase film is eliminated by the addition of only 2% Li per Ti ion. That is, the Fermi-level referenced binding energy of the O 1*s* peak has become identical to the photon energy of the leading O 1*s* XAS peak. Since no further shift of the O 1*s* BE is found at higher Li concentrations,[29] the matching of the O 1*s* PES peak to the XAS peak remains. The conclusion that the population of *d* states eventually eliminates the O 1*s* PES-XAS separation is supported by the results for the (101) surface. Extended sputtering leads to an additional shift of $+0.35 \pm 0.05$eV, in very good agreement with the 0.4 eV offset found for the pristine surface.

The results are summarized in Fig. 5. The CBM-O *p* offset, as determined from the O 1*s* PES and XAS results—is plotted as a function of the additional Ti *d* population for the different experimental situations. (The word "additional" is used to take the small *d* character of the valence band into consideration.) The offset at zero additional Ti *d* population is set to 0.6 ± 0.1 eV, which is the value for the (001) sur-

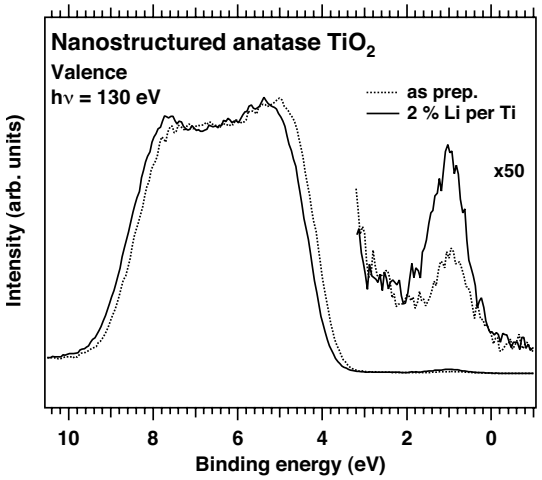

FIG. 4. Valence-band electronic states for an *in situ* prepared film of anatase TiO_2 nanoparticles before (dotted line) and after (solid line) insertion of 2% Li per Ti ion. The binding-energy scale is referenced to the sample holder Fermi level. The addition induces an increase in the intensity of the Ti 3*d* related band-gap state and a positive binding-energy shift of the valence band.

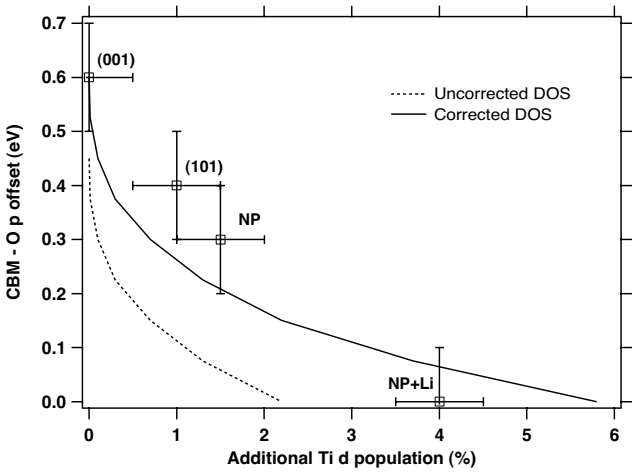

FIG. 5. Squares: The experimental offset between the conduction-band minimum and the threshold of the unoccupied O p states as a function of the additional Ti d population estimated from the intensity of the band-gap state. The dashed and solid lines show the offset as a function of the additional Ti d population for the uncorrected and corrected (shifted) calculated DOSs, respectively.

face. A progressive decrease is observed as qualitatively expected, with an elimination of the CBM—O p offset at about 4% d population per Ti.

In quantitative terms, it is the shape of the d band that determines the decrease in the offset as a function of the additional d population. This motivates a comparison with the theoretical results. The dashed line is derived from the calculated final-state DOS, whereas the solid line is for the shifted O-p edge toward higher energy. It is well known that DFT produces much smaller band gap of semiconductors and insulators. Often a scissor operator is employed to correct the band gap by shifting the band edges in order to fit with the experimental band gap. Here, a similar concept is used to shift the O-p edge by 0.15 eV to match the experimentally observed offset of 0.6 eV for zero additional d population. We find that this operation results in a significantly improved agreement. However, we emphasize that this shift should be regarded only as a way to fit the theory with the experimental observations.

The results have a clear relevance to the many applications of TiO_2 where the properties near the CBM are important, such as photovoltaic cells and photocatalysis. The results are also of importance for the understanding of TiO_2 modified by the addition of small amounts of other elements. In particular, this work can be an important input to the intense debate concerning room-temperature ferromagnetism (RTFM) in anatase TiO_2 doped with magnetic elements.[8] In the case of Co-doped TiO_2 oxygen vacancies (O_{vac}) are needed in order to charge compensate for the replacement of Ti^{4+} with Co^{2+}. The O_{vac} electrons are believed to reside close to the Co^{2+} sites. However, it has become clear that additional oxygen vacancies are required to provide charge carriers for achieving RTFM in an n-type DMS.[8] Such additional oxygen vacancies result in the population of TiO_2 CB states. As the hybridization between the transition metal d states and the O p states may become crucial for ferromagnetism, the character of the electronic states near CBM is important to understand. It is finally intriguing to note that the typical Co concentrations needed for RTFM (1%–7% per Ti ion) matches well the critical concentration for the change in the character of the populated band-gap states of TiO_2. Whether this is pure coincidence or not remains to be elucidated.

With respect to the general applicability of the approach involving O 1s core-level spectroscopy in conjunction with calculations, we can compare it with our previous work on ZrO_2.[28,30] The results for TiO_2 and ZrO_2 have in common that the leading O 1s XAS peak, when related in energy to the valence band, represents the onset for the O p empty states. The core hole appears to modify the intensity distribution of the empty DOS but not the energy position of the threshold. We therefore propose that O 1s XAS combined with O 1s PES is a general method to locate the O p empty states threshold for transition metal oxides. In the case of ZrO_2 the O p empty states threshold is degenerate with the CBM. O 1s core-level spectroscopy can therefore be used to monitor the position of the CBM.[28,30] However, the threshold for the empty O p states is not always degenerate with the CBM. Anatase TiO_2 is one example where this occurs. The kind of information derived from this particular experimental approach can therefore change depending on the electronic properties of the material under study. In order to define the issue to address supporting information from calculations or other experimental techniques is essential.

V. CONCLUSIONS

In summary, PES, XAS, and *ab initio* density-functional calculations have been used to study the properties of the electronic states located at or near the CBM of anatase titanium dioxide. In agreement with previous work we find that the states at the CBM are of pure Ti d_{xy} character. States with p-d character are offset from the CBM and can only be populated after a critical d_{xy} population has been reached. This point can be reached by creation of defects in the form of oxygen vacancies or by Li insertion. The theoretical and experimental estimates of the critical population are in good agreement, giving a value of about $4 \pm 2\%$ of an electronic charge per Ti ion.

ACKNOWLEDGMENTS

We thank the staff at MAX-laboratory for their excellent assistance. The authors are grateful to the Swedish Science Council (VR), the Göran Gustafsson Foundation, the Knut and Alice Wallenberg (KAW) Foundation, and the Crafoord Foundation for the financial support. B.S. acknowledges the Swedish National Infrastructure for Computing (SNIC) for the allocation of computational time.

*Corresponding author. Fax: +46 18 4713524.
anders.sandell@fysik.uu.se.

[1] O. Carp, C. L. Huisman, and A. Reller, Prog. Solid State Chem. **32**, 33 (2004).
[2] A. L. Linsebigler, G. Lu, and J. T. Yates, Chem. Rev. (Washington, D.C.) **95**, 735 (1995).
[3] U. Diebold, Surf. Sci. Rep. **48**, 53 (2003).
[4] M. Ni, M. K. H. Leung, D. Y. C. Leung, and K. Sumathy, Renewable Sustainable Energy Rev. **11**, 401 (2007).
[5] B. O'Regan and M. Grätzel, Nature (London) **353**, 737 (1991).
[6] S. Y. Huang, L. Kavan, I. Exnar, and M. Grätzel, J. Electrochem. Soc. **142**, L142 (1995).
[7] A. Henningsson, H. Rensmo, A. Sandell, H. Siegbahn, S. Södergren, H. Lindström, and A. Hagfeldt, J. Chem. Phys. **118**, 5607 (2003).
[8] M. Wagemaker, D. Lützenkirchen-Hecht, A. A. van Well, and R. Frahm, J. Phys. Chem. B **108**, 12456 (2004).
[9] J. H. Richter, A. Henningsson, B. Sanyal, P. G. Karlsson, M. P. Andersson, P. Uvdal, H. Siegbahn, O. Eriksson, and A. Sandell, Phys. Rev. B **71**, 235419 (2005).
[10] C. Di Valentin, G. Pacchioni, and A. Selloni, Phys. Rev. Lett. **97**, 166803 (2006).
[11] S. A. Chambers, Surf. Sci. Rep. **61**, 345 (2006).
[12] J. Osorio-Guillén, S. Lany, and A. Zunger, Phys. Rev. Lett. **100**, 036601 (2008).
[13] R. Asahi, Y. Taga, W. Mannstadt, and A. J. Freeman, Phys. Rev. B **61**, 7459 (2000).
[14] M. V. Koudriachova, S. W. de Leeuw, and N. M. Harrison, Phys. Rev. B **69**, 054106 (2004).
[15] R. J. Cava, D. W. Murphy, S. Zahurak, A. Santoro, and R. S. Roth, J. Solid State Chem. **53**, 64 (1984).
[16] A. G. Thomas, W. R. Flavell, A. K. Mallick, A. R. Kumarasinghe, D. Tsoutsou, N. Khan, C. Chatwin, S. Rayner, G. C. Smith, R. L. Stockbauer, S. Warren, T. K. Johal, S. Patel, D. Holland, A. Taleb, and F. Wiame, Phys. Rev. B **75**, 035105 (2007).
[17] N. Hosaka, T. Sekiya, C. Aatoko, and S. Kurita, J. Phys. Soc. Jpn. **66**, 877 (1997).
[18] R. Nyholm, J. N. Andersen, U. Johansson, B. N. Jensen, and I. Lindau, Nucl. Instrum. Methods Phys. Res. A **467-468**, 520 (2001); J. N. Andersen, O. Björneholm, A. Sandell, R. Nyholm, J. Forsell, L. Thånell, A. Nilsson, and N. Mårtensson, Synchrotron Radiat. News **4**, 15 (1991).
[19] A. Sandell, M. P. Andersson, Y. Alfredsson, M. K.-J. Johansson, J. Schnadt, H. Rensmo, H. Siegbahn, and P. Uvdal, J. Appl. Phys. **92**, 3381 (2002).
[20] A. Henningsson, M. P. Andersson, P. Uvdal, H. Siegbahn, and A. Sandell, Chem. Phys. Lett. **360**, 85 (2002).
[21] G. Kresse and J. Hafner, Phys. Rev. B **47**, 558 (1993); G. Kresse and J. Furthmüller, *ibid.* **54**, 11169 (1996).
[22] P. E. Blöchl, Phys. Rev. B **50**, 17953 (1994).
[23] S. A. Chambers, Y. Liang, Z. Yu, R. Droopad, J. Ramandi, and K. Eisenbeiser, Appl. Phys. Lett. **77**, 1662 (2000).
[24] R. Puthenkovilakam and J. P. Chang, Appl. Phys. Lett. **84**, 1353 (2004).
[25] G. K. Boschloo, A. Goossens, and J. Schoonman, J. Electrochem. Soc. **144**, 1311 (1997).
[26] J. Stöhr, *NEXAFS Spectroscopy*, Springer Series in Surface Science Vol. 25 (Springer-Verlag, Heidelberg, 1992).
[27] E. O. F. Zdansky, A. Nilsson, H. Tillborg, O. Björneholm, N. Mårtensson, J. N. Andersen, and R. Nyholm, Phys. Rev. B **48**, 2632 (1993).
[28] J. H. Richter, P. G. Karlsson, B. Sanyal, J. Blomquist, P. Uvdal, and A. Sandell, J. Appl. Phys. **101**, 104120 (2007).
[29] J. H. Richter, A. Henningsson, P. G. Karlsson, M. P. Andersson, P. Uvdal, H. Siegbahn, and A. Sandell, Phys. Rev. B **71**, 235418 (2005).
[30] A. Sandell, P. G. Karlsson, J. H. Richter, J. Blomquist, P. Uvdal, and T. M. Grehk, Appl. Phys. Lett. **88**, 132905 (2006).

Paper II

Water Dissociation on Single Crystalline Anatase TiO_2(001) Studied by Photoelectron Spectroscopy

J. Blomquist, L. E. Walle, P. Uvdal, A. Borg and A. Sandell

Journal of Physical Chemistry C **112**, 16616 (2008).

Water Dissociation on Single Crystalline Anatase TiO_2(001) Studied by Photoelectron Spectroscopy

J. Blomquist,[†] L. E. Walle,[‡] P. Uvdal,[†] A. Borg,[‡] and A. Sandell*[,§]

Chemical Physics, Department of Chemistry, Lund University, P.O. Box 124, SE-221 00 Lund, Sweden, Department of Physics, Norwegian University of Science and Technology, NO-7491 Trondheim, Norway, and Department of Physics and Materials Science, Uppsala University, P.O. Box 530, SE-751 21 Uppsala, Sweden

Received: June 27, 2008; Revised Manuscript Received: August 10, 2008

The adsorption of water on the anatase TiO_2(001)-(4 × 1) surface is studied using synchrotron radiation-excited core level photoelectron spectroscopy. The coverage-dependent adsorption of water at low temperature is monitored and compared to the sequence obtained after heating of a water multilayer. Two adsorption phases of submonolayer coverage can be defined: Phase 1 consists only of dissociated water, observed as OH-groups. This phase is found at low coverage at low temperature (190 K) and is the only state of adsorbed water above ∼230 K. The saturation coverage of phase 1 is consistent with dissociation on the 4-fold-coordinated Ti ridge atoms of the (4 × 1) surface reconstruction. Phase 2 is found at higher coverage, reached at lower temperature. It consists of a mixture of dissociated and molecular water with a ratio of 1:1 at 170 K. The molecular water is found to bond to the hydroxyl groups. The hydroxyl coverage of phase 2 is approximately 2 times that of phase 1. The results suggest that the OH and H_2O species of phase 2 are confined to the ridges of the surface.

1. Introduction

Water interaction with solid surfaces is central for a wide range of fields, such as catalysis, photochemistry, electrochemistry, corrosion, and biocompatible materials.[1,2] Titanium dioxide (TiO_2) is a material used within a majority of the above applications because it is photoactive and chemically stable in a variety of environments.[3] Rutile TiO_2 of the (110) termination is the most stable surface of the most stable polymorph of titanium dioxide. Rutile TiO_2(110) single crystals are readily available, which is one reason why it is one of the most studied metal oxide surfaces in the world. Water adsorption on rutile TiO_2(110) can in turn be considered as the benchmark system for molecular adsorption on metal oxides. The observation of photoinduced splitting of water into hydrogen and oxygen on a rutile TiO_2 single crystal in 1972 is a discovery that has initiated many of these studies.[4]

The anatase polymorph of TiO_2 appears to be an even more potent photocatalyst than rutile.[5−7] Anatase is furthermore the preferred phase when TiO_2 nanoparticles are formed.[8] Nanoporous TiO_2 electrodes can be prepared by forming a network of sintered nanoparticles. These have been shown to be most useful for photoelectrochemical applications by virtue of the huge effective surface area.[9] Anatase nanoparticles typically expose (101) and (100)/(010) surfaces at about equal amounts together with small amounts of (001).[10] Consequently, comparative studies of water adsorption on well-defined anatase surfaces is a stepping stone toward an understanding of surface processes on nanocrystalline TiO_2 in aqueous environments. In addition, studies of water on anatase TiO_2 can further the understanding of the prototypical water/rutile TiO_2 system.

The structure and energetics of water adsorption on the anatase TiO_2(101) and (001) surfaces at various coverages have been studied by use of density functional theory (DFT) calculations.[10] It was shown that molecular water adsorption is favored on the (101) surface. The behavior on the (001) surface was found to be very different. At low coverages, water only adsorbs dissociatively, while at higher coverages water adsorption results in a dissociated layer onto which molecular water is hydrogen bonded. Dissociative adsorption on the (001) surface and molecular adsorption on the (101) surface have also been found in other theoretical studies.[11−13]

Experimental studies of water adsorption on single crystalline anatase TiO_2 are scarce. This can be attributed to the difficulty in obtaining high-quality single crystal samples. The adsorption of water on the anatase (101) surface under ultrahigh vacuum (UHV) conditions has been studied using X-ray photoelectron spectroscopy (XPS) and temperature-programmed desorption (TPD).[14] The (101) surface was prepared by growing a homoepitaxial film on a (101) mineral sample to ensure purity. The results were found to confirm the theoretical prediction of molecular adsorption. Desorption states were found at 160, 190, and 250 K. These were assigned to multilayer water, water adsorbed on 2-fold-coordinated (bridge) O, and water adsorbed on 5-fold-coordinated Ti, respectively. In an earlier work, the photoactivities of the anatase (001) and (101) surfaces was compared.[15] The results were interpreted in terms of different water adsorption states on the two surfaces. However, no study of water adsorption on the (001) surface in UHV has been undertaken so far.

The clean (001) surface of anatase TiO_2 undergoes a (4 × 1) reconstruction in UHV.[16,17] A structure model of the (001)-(4 × 1) surface has been derived from scanning tunneling microscopy (STM) results in conjunction with DFT calculations.[18,19] The surface can be described as consisting of ridges separated by terraces. Recent calculations suggest that water dissociates also on the reconstructed (4 × 1) surface but only

* Corresponding author. Fax: +46 18 4713524. E-mail: anders.sandell@fysik.uu.se.
[†] Lund University.
[‡] Norwegian University of Science and Technology.
[§] Uppsala University.

10.1021/jp805664b CCC: $40.75
Published on Web 09/25/2008

at the ridges.[20] The adsorption of formic acid on thin film anatase TiO_2(001) has been studied by STM and noncontact atomic force microscopy.[19] The high reactivity of the ridges of the (001)-(4 × 1) surface was convincingly confirmed.

In this work, we study the coverage-dependent adsorption of water on the anatase TiO_2(001)-(4 × 1) surface by stepwise heating of a multilayer water film and by progressive water adsorption at low temperature. We find that water dissociates on the surface at low coverage. The dissociation is strongly connected to the highly reactive ridges forming the (4 × 1) reconstruction, thereby confirming the theoretical predictions. We also present evidence for a mixed phase consisting of dissociated and molecular water at higher coverages. This phase has not been addressed in the previous theoretical studies of water adsorption on the reconstructed surface.

2. Experimental Section

The O 1s core level photoemission spectra were recorded at beamline D1011 at the Swedish National Synchrotron Facility MAX II.[21] The end station comprises a 200 mm radius hemispherical electron energy analyzer of Scienta type. Binding energy (BE) calibration of the core level photoelectron (PES) spectra against the Fermi level was achieved by referencing to a Pt foil mounted on the sample holder.

Two types of anatase TiO_2(001)-(4 × 1) surfaces were prepared: one by metal organic chemical vapor deposition on a lattice matched substrate [$SrTiO_3$(001)] and one by cleaning of a natural single crystal. That single crystalline anatase TiO_2(001) forms on $SrTiO_3$(001) has been demonstrated previously.[16,17,22]

The Nb-doped (1.0 wt %) $SrTiO_3$(001) crystals were purchased from MaTeck GmbH, Germany. Cleaning of the $SrTiO_3$(001) substrate was accomplished by cycles of Ar^+ sputtering (1 keV) followed by annealing to 1000 K in O_2 atmosphere (5×10^{-7} mbar). Titanium tetra-isopropoxide (TTIP, 99.99% Aldrich) was dosed through a stainless steel dosing tube facing the sample. The TiO_2 film was grown at a TTIP background pressure of 5×10^{-8} mbar and a sample temperature of 850 K. The Sr 3d states were barely visible after TiO_2 film growth, suggesting a film at least 100 Å thick. The anatase TiO_2(001) single crystal (provided by PI-KEM Ltd., UK) was cleaned by cycles of Ar-sputtering and subsequent annealing in oxygen to 920 K. For both surfaces, the formation of the (4 × 1) reconstruction characteristic for the anatase (001) surface was confirmed with low-energy electron diffraction (LEED). A representative LEED image is shown in Figure 1. The PES spectra of the Ti 2p core level and the valence region showed that the defect density of the pristine surfaces was very low. That is, the Ti 2p spectrum displayed only a Ti^{4+} state, and no discernible structures were found in the band gap region.

Radiation-induced effects have proved to be an important issue for adsorbed water, especially on metallic surfaces.[23,24] The insertion device used in the present case is a bending magnet, giving a spot size at the sample of about 2 mm^2. The photon flux is approximately 5×10^{10} photons mm^{-2}. Previous measurements on water on rutile TiO_2(110) using a flux 1 order of magnitude greater were found to lead to minimal radiation damage after 1 h.[25] In our case, the only radiation-induced change was found for the mixed OH/H_2O layer where a very small decrease of the H_2O coverage was noted after about 1 h. Still, great care was taken to perform the measurement series as quickly as possible.

3. Results and Discussion

Figure 2a shows O 1s PES spectra recorded upon adsorption and subsequent stepwise annealing of a water multilayer on the single crystal surface. Figure 2b shows O 1s PES spectra after stepwise water adsorption on the anatase thin film surface at 190 ± 20 K. The spectra shown in Figure 2 are all normalized to the ring current and number of scans. They were measured at grazing emission angle (60°) and a photon energy of 610 eV to obtain a high surface sensitivity. The BE for the O 1s peak of the pristine TiO_2 surfaces is 530.60 eV for the film grown on $SrTiO_3$(001) and 530.45 eV for the bulk single crystal sample. We attribute this effect to a higher defect density in the MOCVD grown film, which leads to shifts of this magnitude for defects at a percentage level.[26] Upon exposure to water, states at BE:s of 532 and 534 eV are observed, assigned to adsorbed OH and H_2O, respectively.[25,27]

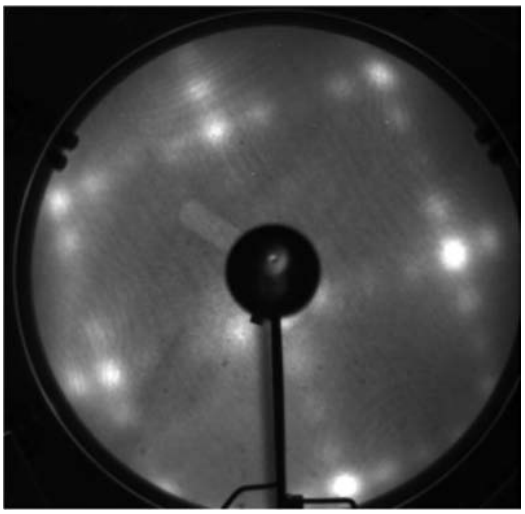

Figure 1. Low-energy electron diffraction (LEED) pattern of the pristine anatase TiO_2(001) surface. The extra spots associated with the (4 × 1) surface reconstruction are clearly visible. The electron kinetic energy was 77 eV.

To derive quantitative information, the O 1s spectra have been delineated. This was accomplished by curve fitting in combination with subtraction procedures to establish binding energies and line widths. Spectra recorded in normal and grazing emission as well as spectra for the clean surface and after adsorption were used for the subtractions. The individual components are included in Figure 2. Noteworthy is that some additional intensity is found at the high BE side of the TiO_2 related peak for the pristine surface. Figure 3 shows that the change in the spectral shape when changing the emission angle is negligible. The weak high BE tail is therefore not likely to be due to an adsorbed species because its intensity relative to the main peak would then change significantly. We therefore propose that the high BE tail is an inherent property of the O 1s spectrum of pure anatase. To facilitate the analysis, a component with parameters similar to those of the hydroxyl component has been used to describe this structure. Noteworthy is that a structure of the same BE as adsorbed OH but associated with the oxide has been found for clean rutile TiO_2(110), lending support for our interpretation.[25]

When comparing the intensities of the various components, it can be concluded that the OH and H_2O coverages above 170 K must be in the submonolayer regime. For this experimental setting, the major part of the O 1s intensity from the substrate and the water multilayer originates from ionization of the surface layer. The O 1s components assigned to OH groups and molecular H_2O have both a maximum intensity of about 20% of the clean substrate O 1s peak and about 14% of the O 1s peak for multilayer water. The low relative intensities together

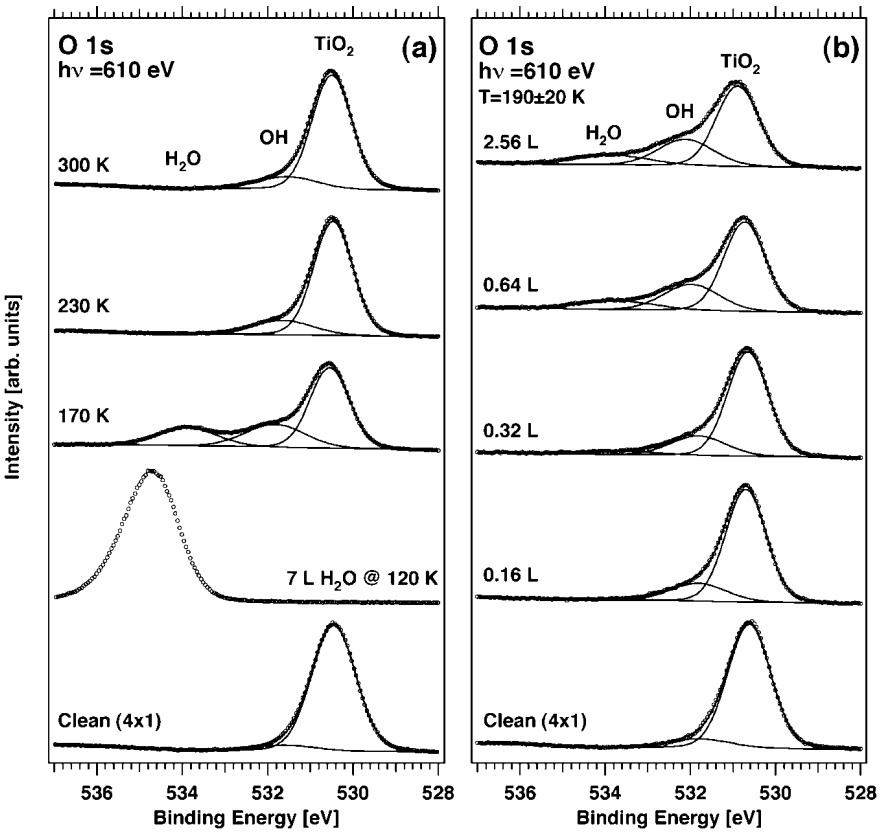

Figure 2. O 1s spectra for water adsorption on anatase TiO_2(001)-(4 × 1) recorded in grazing emission. The individual components associated with TiO_2 and adsorbed OH and H_2O obtained by curve fitting are included. (a) Heating series. (b) Growth series at a sample temperature of about 190 K.

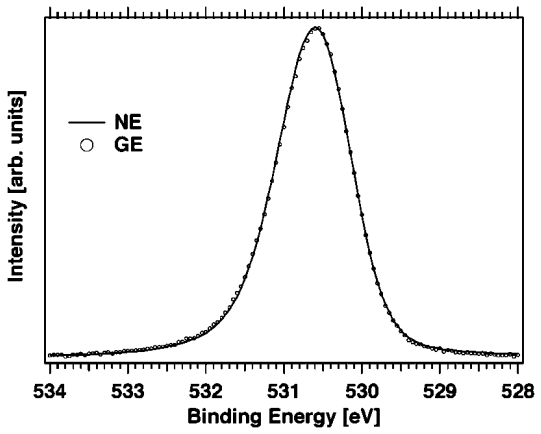

Figure 3. O 1s spectra for the pristine anatase TiO_2(001)-(4 × 1) surface recorded in normal (NE, −) and grazing (GE, ○) emission. A Shirley background has been subtracted in both spectra to facilitate the comparison.

with the fact that the substrate surface contains both O and Ti atoms show that the adsorbed OH and H_2O can only cover a fraction of the surface.

Better estimates of the adsorbate coverage can be derived from O 1s PES spectra recorded at two different angles, normal emission and 60° off normal emission. Two assumptions are needed: first, that the angle-dependent attenuation of the substrate signal follows the exponential expression and, second, that the angle dependence of the (OH):(total signal) ratio equals that of the (surface bridging O):(total signal) ratio. An advantage with this approach is that no estimate of an electron mean free path is needed. The intensities of the OH- and H_2O-peaks can in this way be translated into coverage relative to the surface bridging (2-fold-coordinated) O atoms of the clean (4 × 1) surface. The OH and H_2O coverages are summarized in Figure 4. The intensity of the OH-related component has been corrected by subtraction of the estimated contribution from the high BE tail associated with the pristine anatase surface.

The coverages derived from the temperature series start from the situation attained after desorption of the multilayer by heating to 170 K. At this point, the OH and H_2O coverages are very similar. The estimated coverage corresponds to about 0.4 per bridging surface O atom. Heating to 230 K results in nearly complete desorption of molecular water and a decrease in the hydroxyl coverage to about 0.2 OH groups per surface O atom. Subsequent heating to 300 K leads to a decrease in the OH coverage down to 0.17 OH groups per surface O atom.

Upon water dosing on the clean surface held at 190 ± 20 K, the OH-related peak increases rapidly after the first dose (0.08 L). The OH coverage is here estimated to 0.17 OH groups per surface O atom. After this point, the increase is slower, reaching a kink at 0.64 L, after which the coverage increases only very little. The OH coverage after 2.56 L amounts to 0.42 OH groups per surface O atom. A significant increase of the component assigned to adsorbed molecular water is not observed until after a dose of 0.32 L. The amount of adsorbed water increases further up to a dose of 0.64 L, after which the increase is very slow, just as for the amount of adsorbed OH. The OH/H_2O ratio after 2.56 L water at 190 ± 20 K is 1.6. When comparing to the temperature series, it is found that the OH/H_2O ratio at 190 K is indeed expected to be greater than that at 170 K.

The O 1s binding energy as a function of coverage for the different situations is shown in Figure 5. The binding energy of the OH-related O 1s component shows an increase by 0.25 ± 0.05 eV for increasing coverage. The binding energies for

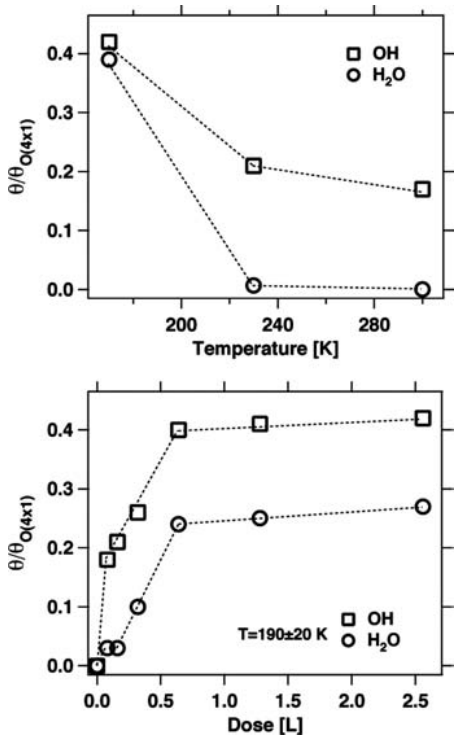

Figure 4. Summary of the quantitative results obtained from the O 1s spectra shown in Figure 1. The plots show the OH and H_2O coverages as a function of temperature (top) and water dose at 190 ± 20 K (bottom). The coverages are given relative to the number of bridging surface oxygen atoms within the (4 × 1) unit cell.

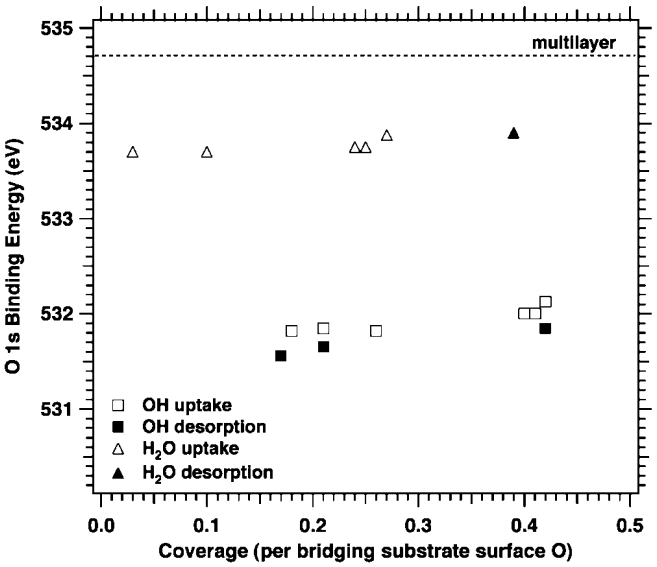

Figure 5. O 1s binding energies for the OH and H_2O components for the desorption series measured by successive heating steps and the growth series measured as the uptake at 190 K.

the uptake series are systematically greater by about 0.2 eV as compared to the desorption series. As noted above, this shift is also found when comparing the O 1s peaks of the clean surfaces and is most likely associated with slightly different defect densities in the two samples. The binding energy of the H_2O-related O 1s component increases by 0.20 ± 0.05 eV for increasing coverage. At the highest coverage (0.4 per substrate surface O), the O 1s binding energy for adsorbed water is found to be lower than that of multilayer water by about 0.8 eV.

To summarize, we can define two phases on the basis of the results presented in Figures 2 and 4, both of which are of

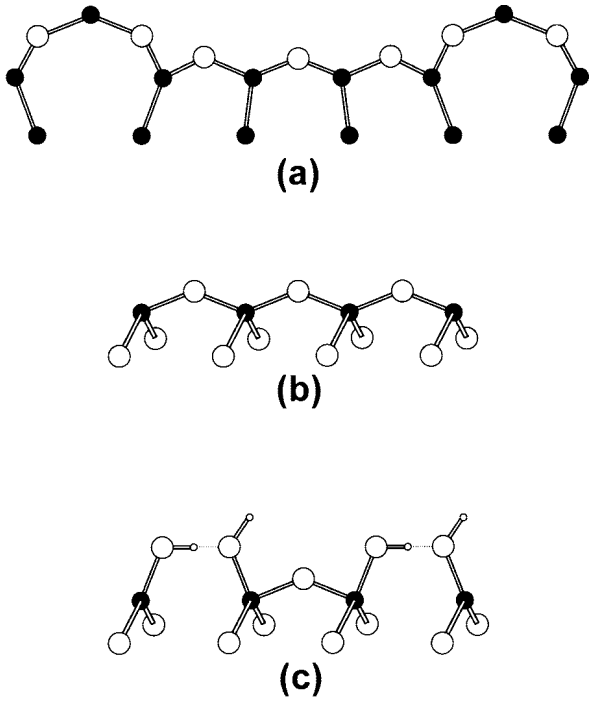

Figure 6. Schematic illustrations of the (4 × 1) reconstructed anatase TiO_2(001) surface before and after hydroxylation. The atomic structures are based on the ADM model.[18] (a) The clean reconstructed surface projected along the [100] direction. (b) Illustration of how the ridges extend along the [010] direction. (c) Hydroxylation of the ridge Ti sites as proposed in ref 20. This corresponds to phase 1 in the present study.

submonolayer coverage. The first phase consists only of dissociated water, observed as OH-groups. This phase is found at low coverage at low temperature and is the only state of adsorbed water above 230 K. We define phase 1 as the situation attained at 230 K, where the hydroxyl coverage is 0.2 OH per substrate surface O. This situation is also formed after dosing of 0.08−0.16 L water at 190 K. The second phase consists of a mixture of dissociated and molecular water, which is possible to form at higher coverage at low temperature. The maximum hydroxyl coverage for phase 2 is about 0.4 OH per substrate surface O, that is, approximately 2 times the hydroxyl coverage of phase 1. The water coverage associated with this hydroxyl coverage depends on the substrate temperature.

In the following, we will discuss plausible scenarios for the water adsorption and dissociation associated with the two different phases. The (4 × 1) surface structure is nonuniform, consisting of ridges separated by terraces. This has been verified by STM measurements.[19] Figure 6a and b illustrates schematically the ad-molecule (ADM) model, which is the atomic structural model that at present seems to be most compatible with available experimental data.[18] Within the ADM model, the (4 × 1) surface can be viewed as a transformation of the (1 × 1) surface by replacing bridging oxygen atoms by TiO_3 units.[18] The reconstruction is believed to occur to relieve the surface stress. The 4-fold-coordinated Ti atoms [Ti(4)] are located on the ridges, whereas 5-fold-coordinated [Ti(5)] atoms are located on the terraces. One (4 × 1) surface unit cell comprises six bridging O(2) atoms, four Ti(5) atoms, and one Ti(4) atom.[18]

The coverage estimate for phase 1 derived from the O 1 s spectra suggests the presence of dissociated water only on the Ti(4) atoms located on the ridges of the (4 × 1) structure. The OH amount of phase 1 is estimated to 0.20 ± 0.03 relative to the amount of bridging O atoms of the clean (4 × 1) surface,

which translates into 1.2 ± 0.2 OH groups per Ti(4) atom. This value can be regarded as an upper limit because minute traces of molecular water were observed after heating to 230 K, indicating that this temperature lies on or slightly below the border where mixed layer formation is allowed (water readsorption during the measurements is also possible). That the OH coverage is consistent with efficient water dissociation on the Ti(4) atoms is expected given the high reactivity of the ridges found in the study on formic acid adsorption.[19]

Our results provide the first experimental support of previous calculations for water adsorption on the (4 × 1) reconstructed surface. The theoretical work suggests that water dissociates effectively on the ridges while no dissociation occurs on the terraces.[20] The most favorable situation was found to be the one shown in Figure 6c. It is a structure in which one terminally bound hydroxyl group is found on all Ti(4) atoms on the ridge. This would correspond to phase 1. The calculations also present a feasible explanation to the low reactivity found for the terraces:[19,20] The (4 × 1) reconstruction causes the Ti(5) atoms to be pushed slightly away from the surface as compared to the (1 × 1) surface.[18]

Phase 2 is associated with additional water dissociation concomitant with the adsorption of molecular water. Within the temperature range 170−190 K, three different types of molecular water adsorption may be considered:[14,24,28] hydrogen bonded to hydroxyl groups, hydrogen bonded to O(2) atoms, and oxygen bonded to Ti(5) atoms. Bonding to O(2) and Ti(5) atoms is believed to occur on the anatase TiO_2(101) surface. However, when desorbing a water multilayer deposited on the TiO_2(101) surface, the O 1s BE is found to increase by 1 eV when reaching the submonolayer regime. The increased O 1s BE is associated with water adsorbed on the Ti(5) sites, while very similar O 1s binding energies are found for the water multilayer and water presumably adsorbed on the O(2) sites. The coverage dependence of the O 1s BE for water on the (101) surface is thus very different from the coverage dependence of the O 1s BE for water on the (001) surface. The 0.8 eV decrease in the O 1s BE for decreasing water coverage on the (001) surface is instead in very good agreement with the behavior found for water adsorption on a hydroxylated oxide surface.[28] From this follows that the molecular water observed on the (001) surface between 170−190 K is associated with hydrogen bonding to the hydroxyl groups formed by water dissociation.

When discussing extensive hydroxylation of the anatase TiO_2(001) surface, it is important to determine if the (4 × 1) reconstruction is affected. Calculations show that the unreconstructed (1 × 1) surface of anatase TiO_2(001) becomes stabilized by hydroxylation.[20,29] In a study of H_2O/O/Cu(110), it was furthermore found that the O p(2 × 1) reconstruction could be lifted upon water adsorption and dissociation below 220 K.[30] Thus, heating of the water multilayer on anatase TiO_2(001) could be complex and involve a (1 × 1) to (4 × 1) transition. In a preliminary study using a standard LEED, we find no sign of a lifting of the (4 × 1) structure upon water dosing at 160 K. This is not conclusive information because a partial lifting of the (4 × 1) structure can be difficult to observe and the LEED can also influence the adsorbate layer.[31]

Under the assumption of an unperturbed (4 × 1) surface, the additional water dissociation will most likely occur either on the already hydroxylated ridges or on the Ti(5) atoms located at the terraces. According to the proposed model of phase 1, the hydroxylated Ti sites on the ridges remain 4-fold-coordinated. Thus, these sites may still be reactive toward water dissociation but to a lesser extent due to the preceding hydroxylation step. A valuable comparison is the adsorption of formic acid on the (4 × 1) surface, which has been studied both experimentally and theoretically. Calculations suggest that a bidentate configuration on the Ti ridge atoms is energetically favored. The bidentate adsorption geometry leads to 5-fold-coordinated Ti. However, the bidentate geometry is not observed experimentally at room temperature.[19] Instead, formic acid appears to adsorb in a monodentate fashion.[19,20] Consequently, the results on formic acid suggest that doubly hydroxylated 5-fold-coordinated Ti atoms on the ridges may not be stable at room temperature, which is what we observe. Regarding dissociation on the terrace Ti(5) atoms, one OH group per Ti atom would result in an increased OH coverage by a factor of 5. This is not observed, making dissociation on the terraces less likely as was shown in the theoretical study.[20]

With respect to uncertainties in the results, we stress that the method of estimating the coverage is based on assumptions regarding the spectral intensities. The error within this approach is very difficult to estimate. One source of error is photoelectron diffraction effects, which can be significant for single crystal systems. In the case of water adsorbed on rutile TiO_2(110), modulations of about ±40% were observed in the kinetic energy regime used here.[25] Clearly, further studies are warranted. To estimate the diffraction effects, O 1s spectra for a range of photon energies are needed. Low-temperature STM and noncontact AFM studies can furthermore be important to shed light on the structure of the mixed layer. Regarding the adsorption mechanism, it is possible that the presence of molecular water can aid in the stabilization of the high hydroxyl coverage in the mixed layer. The interplay between the adsorbate−substrate bond and the hydrogen bonding within the mixed layer is something that could be worthwhile to address in future theoretical studies.

4. Conclusions

In summary, we have studied the adsorption of water on anatase TiO_2(001) with respect to temperature and coverage dependence. Above 230 K, only dissociated water is observed in the form of hydroxyl groups. The hydroxylation is suggested to occur on the 4-fold-coordinated Ti atoms located on the ridges of the (4 × 1) reconstructed surface. The high reactivity and the location of the hydroxyl groups confirm previous theoretical predictions. Below 230 K, it is possible to form a mixed layer consisting of hydroxyl groups and molecular water. The molecular water is found to bond to the hydroxyl groups. The OH coverage for the mixed layer can exceed that of the pure OH layer by a factor of 2. The relatively low increase in OH coverage suggests that also the additional water dissociation is associated with the ridges of the (4 × 1) surface structure.

Acknowledgment. We thank the staff at MAX-laboratory for their assistance. This work has been supported through the Swedish Science Council (VR), the Knut and Alice Wallenberg foundation (KAW), the Crafoord foundation, and the Göran Gustafsson foundation. L.E.W. has been supported through the Strategic Area Materials at Norwegian University of Science and Technology.

References and Notes

(1) Thiel, P. A.; Madey, T. E. *Surf. Sci. Rep.* **1987**, *7*, 211.
(2) Henderson, M. A. *Surf. Sci. Rep.* **2002**, *46*, 1.
(3) Diebold, U. *Surf. Sci. Rep.* **2003**, *48*, 53.
(4) Fujishima, A.; Honda, K. *Nature (London)* **1972**, *238*, 37.
(5) Carp, O.; Huisman, C. L.; Reller, A. *Prog. Solid State Chem.* **2004**, *32*, 33.

(6) Linsebigler, A. L.; Lu, G.; Yates, J. T. *Chem. Rev.* **1995**, *95*, 735.
(7) Kavan, L.; Grätzel, M.; Gilbert, S. E.; Klemenz, C.; Scheel, H. J. *J. Am. Chem. Soc.* **1996**, *118*, 6716.
(8) Taylor, C. J.; Gilmer, D. C.; Colombo, D. G.; Wilk, G. D.; Campbell, S. A.; Roberts, J.; Gladfelter, W. L. *J. Am. Chem. Soc.* **1999**, *121*, 5220.
(9) (a) O'Regan, B.; Grätzel, M. *Nature (London)* **1991**, *353*, 737. (b) Hagfeldt, A.; Grätzel, M. *Chem. Rev.* **1995**, *95*, 49.
(10) Vittadini, A.; Selloni, A.; Rotzinger, F. P.; Grätzel, M. *Phys. Rev. Lett.* **1998**, *81*, 2954.
(11) Fahmi, A.; Minot, C. *Surf. Sci.* **1994**, *304*, 343.
(12) Redfern, P. C.; Zapol, P.; Curtiss, L. A.; Rajh, T.; Thurnauer, M. C. *J. Phys. Chem. B* **2003**, *107*, 11419.
(13) Onal, I.; Soyer, S.; Senkan, S. *Surf. Sci.* **2006**, *600*, 2457.
(14) Herman, G. S.; Dohnálek, Z.; Ruzycki, N.; Diebold, U. *J. Phys. Chem. B* **2003**, *107*, 2788.
(15) Hengerer, R.; Kavan, L.; Krtil, P.; Grätzel, M. *J. Electrochem. Soc.* **2000**, *147*, 1467.
(16) Herman, G. S.; Sievers, M. R.; Gao, Y. *Phys. Rev. Lett.* **2000**, *84*, 3354.
(17) Liang, Y.; Gan, Y.; Chambers, S. A.; Altman, E. I. *Phys. Rev. B* **2001**, *63*, 235402.
(18) Lazzeri, M.; Selloni, A. *Phys. Rev. Lett.* **2001**, *87*, 266105.
(19) Tanner, R. E.; Sasahara, A.; Liang, Y.; Altman, E. I.; Onishi, H. *J. Phys. Chem. B* **2002**, *106*, 8211.
(20) Gong, X.-Q.; Selloni, A.; Vittadini, A. *J. Phys. Chem. B* **2006**, *110*, 2804.
(21) Andersen, J. N.; Björneholm, O.; Sandell, A.; Nyholm, R.; Forsell, J.; Thånell, L.; Nilsson, A.; Mårtensson, N. *Synchrotron Radiat. News* **1991**, *4*, 15.
(22) Chen, S.; Mason, M. G.; Gysling, H. J.; Paz-Pujalt, G. R.; Blanton, T. N.; Castro, T.; Chen, K. M.; Fictorie, C. P.; Gladfelter, W. L.; Fanciosi, A.; Cohen, P. I.; Evans, J. F. *J. Vac. Sci. Technol., A* **1993**, *11*, 2419.
(23) Andersson, K.; Nikitin, A.; Pettersson, L. G.; Nilsson, A.; Ogasawara, H. *Phys. Rev. Lett.* **2004**, *93*, 196101.
(24) (a) Weissenrieder, J.; Mikkelsen, A.; Andersen, J. N.; Feibelman, P. J.; Held, G. *Phys. Rev. Lett.* **2004**, *93*, 196102. (b) Clay, C.; Haq, S.; Hodgson, A. *Phys. Rev. Lett.* **2004**, *92*, 046102. Ogasawara, H.; Brena, B.; Nordlund, D.; Nyberg, M.; Pelmenschikov, A.; Pettersson, L. G.; Nilsson, A. *Phys. Rev. Lett.* **2002**, *89*, 276102.
(25) Allegretti, F.; O'Brien, S.; Polcik, M.; Sayago, D. I.; Woodruff, D. P. *Phys. Rev. Lett.* **2005**, *95*, 226104.
(26) Richter, J. H.; Henningsson, A.; Karlsson, P. G.; Andersson, M. P.; Uvdal, P.; Siegbahn, H.; Sandell, A. *Phys. Rev. B* **2005**, *71*, 235418.
(27) Wang, L.-Q.; Baer, D. R.; Engelhard, M. H.; Shultz, A. N. *Surf. Sci.* **1995**, *344*, 237.
(28) Abu Haja, M.; Guimond, S.; Kuhlenbeck, H.; Freund, H.-J. *Surf. Sci.* **2006**, *600*, 1040.
(29) Gong, X.-Q.; Selloni, A. *J. Phys. Chem. B* **2005**, *109*, 19560.
(30) Ammon, Ch.; Bayer, A.; Steinrück, H.-P.; Held, G. *Chem. Phys. Lett.* **2003**, *377*, 163.
(31) Held, G.; Menzel, D. *Surf. Sci.* **1994**, *316*, 92.

JP805664B

Paper III

Experimental evidence for mixed dissociative and molecular adsorption of water on a rutile TiO_2(110) surface without oxygen vacancies

L. E. Walle, A. Borg, P. Uvdal and A. Sandell

Submitted to Physical Review Letters (2009).

Experimental evidence for mixed dissociative and molecular adsorption of water on a rutile TiO_2(110) surface without oxygen vacancies

L. E. Walle[1], A. Borg[1], P. Uvdal[2], and A. Sandell[3,*]

[1] *Dept. of Physics, Norwegian University of Science and Technology (NTNU), NO-7491 Trondheim, Norway*

[2] *Chemical Physics, Dept. of Chemistry, P.O. Box 124, and MAX-lab, P.O. Box 113, Lund University, SE-221 00 Lund, Sweden*

[3] *Dept. of Physics and Materials Science, Uppsala University, P. O. Box 530, SE-751 21 Uppsala, Sweden*

We present evidence for mixed molecular and dissociative water adsorption at monolayer coverage on a rutile TiO_2(110) surface free from oxygen vacancies using synchrotron radiation photoemission. At monolayer coverage the OH:H_2O ratio is close to 0.5 and reducing the coverage by heating yields an increased OH:H_2O ratio. At room temperature neither species originating from the monolayer on the defect free surface can be detected. The OH species of the monolayer hence recombines and leaves the surface at much lower temperatures than OH formed by water dissociation on oxygen vacancies.

PACS: 68.47.Gh, 68.43.Hn, 82.65.+r, 79.60.Dp

*Corresponding author. Email: anders.sandell@fysik.uu.se; Fax: +46 18 4713524

Rutile TiO_2(110) has for many years been regarded as the benchmark surface for fundamental studies of metal oxide surface chemistry [1,2]. TiO_2 is also important in a wide variety of applications, such as photochemical water splitting, solar cells, catalysis, gas sensing and biomedical implants [1,3,4]. Since water is an integral part of the environment in most of the above-mentioned applications, the H_2O/TiO_2(110) system has received more attention than any other comparable system [1,2,5]. A better understanding of the interaction of water with the rutile TiO_2(110) surface will also broaden our understanding of water chemistry at oxide surfaces in general. While the dissociation of water on the oxygen deficient TiO_2(110) surface has been characterized in detail [6-13], there is as of yet no consensus reached between experimentalists and theorists regarding a very fundamental question: Does water dissociate upon adsorption on the defect-free TiO_2(110) surface?

Theoretical studies of water adsorption on the defect-free TiO_2(110) surface presented over the years are contradictory. Early studies predicted dissociative adsorption at all coverages [14,15]. More recent studies suggest a delicate balance between dissociated, partial dissociated and molecular configurations, a balance that most probably depends on the coverage [16-24]. The TiO_2(110)-(1x1) surface, shown in Fig. 1, consists of alternating rows of fivefold-coordinated Ti atoms [Ti(5)] and twofold-coordinated bridging oxygen atoms (O_{br}). The situation at a coverage corresponding to one water molecule per Ti(5) site (defined as one monolayer, 1 ML) has been heavily debated. Lindan et al. have proposed a mixed molecular-dissociated configuration as the most stable state, emphasizing the importance of intermolecular hydrogen bonding [16,19]. Still, the adsorption energies of the mixed phase and a pure molecular phase were very similar. In a recent quantum molecular dynamics study it was found that 20% of the water molecules dissociate, supporting the notion of a mixed monolayer [22]. To conclude, available theoretical results do not give a clear cut answer as to whether water adsorbs associatively or dissociatively on defect-free TiO_2(110).

The most common view expressed in experimental studies is that at all coverages water adsorbs molecularly on the ideal TiO_2(110) surface and dissociation does only take place at defect sites [1,25-27]. One plausible reason for the lack of conclusive experimental proof of dissociation on the defect-free surface can be the elusive nature of the dissociated state. The dissociated state found in the theoretical studies of the defect-free TiO_2(110) surface is depicted in Fig. 1. It consists of one

terminal OH (OH_t) at a Ti(5) site and a hydrogen atom adsorbed on a neighboring O_{br}, giving a OH_{br} [12,16,19,28]. Since the two OH groups remain neighbors, the barrier for the transition to a molecular state is low [12]. This state has therefore been denoted "pseudo-dissociated". The presence of a pseudo-dissociated state in scanning tunneling microscopy (STM) images has been controversial. At room temperature (RT), STM fails to image molecular water due to its high mobility at this temperature [29,30]. Neither has there been any record of pseudo-dissociated water. Structures assigned to OH_{br} and OH_t species have been reported but they vanish as soon as they occupy neighboring sites, leaving a bridging O atom [29]. Evidently pseudo-dissociated water is not stable at RT. The presence of pseudo-dissociated water in STM images recorded below 200 K and at low water coverages has been discussed with the aid of theoretical STM image simulations [12,28]. However, discriminating between pseudo-dissociated and molecular water using STM has proven to be difficult. Conclusive experimental results that show whether OH is formed or not upon water adsorption on a surface free from O vacancies are therefore much needed.

In this Letter, we present a study of the interaction of water with the rutile TiO_2(110) surface using synchrotron radiation photoemission. We demonstrate that O 1s spectra recorded at grazing emission angle at optimized photon energy in conjunction with valence spectra allow for the observation of OH on the surface even when substrate oxygen is present. We present clear evidence for mixed molecular and dissociative water adsorption at monolayer coverage on a TiO_2(110) surface free from oxygen vacancies. Reducing the coverage by heating of the monolayer results in an increased OH:H_2O ratio. Importantly, neither species originating from the monolayer is detected at room temperature, which shows that OH in the mixed monolayer is much less stable than OH formed at oxygen vacancies. The detailed nature of OH in the mixed layer is not possible to unveil with present experimental results but they are clearly consistent with the notion of pseudo-dissociated water on the vacancy free surface.

The photoemission measurements were performed at beamline D1011 at the Swedish synchrotron radiation source MAX-II using a Scienta 200 mm hemispherical electron energy analyzer [31]. The rutile TiO_2(110) single crystal (SurfaceNet GmbH) was cleaned by sputtering (Ar^+, 1 keV) and annealing to 900 K until no contaminations could be discerned with photoelectron spectroscopy (PES) and a sharp (1x1) low energy electron diffraction (LEED) pattern was observed. Pure water was

introduced through a leak valve and doses are given in Langmuirs (1 L = $1 \cdot 10^{-6}$ Torr·sec). Annealing of the adsorbate layer was performed at a rate of about 1 K per second and with the sample kept at the desired temperature during measurements in order to minimize re-adsorption of water. Spectra for the clean sputtered and annealed surface were measured at elevated temperature (400-550 K). The presented O 1s spectra were recorded in 60° off normal emission using 610 eV photons. The valence spectra were recorded in normal emission using 130 eV photons. The binding energy was referenced to the Fermi level of a Pt foil attached to the sample holder. Radiation damage of the overlayer was carefully checked and found to be negligible [32].

A TiO_2(110) surface free from oxygen vacancies was prepared following the recipe in ref. [33]. Sputtering and annealing in vacuum produce a reduced surface, denoted *r*-TiO_2(110). At room temperature, water dissociates on the O_{br} vacancies on the *r*-TiO_2(110) surface giving a hydrated surface. The capping H atoms can be reacted off by subsequent exposure to O_2 resulting in a surface with perfect O_{br} rows [33]. This is a critical step since O_2 doses exceeding the optimal value yields oxygen ad-atoms that may affect the surface chemistry [30]. Therefore, the capping hydrogen atoms were titrated away in a stepwise fashion by careful monitoring of the intensity of the OH 3σ peak. Figure 2 (a) shows valence photoemission results for such a preparation sequence, performed at RT. Spectra are shown for: the clean *r*-TiO_2 surface (green curve), after a subsequent dose of 5 L H_2O (blue curve), after a total dose of 5 L O_2 deposited in three steps (red curve) and finally after another 5 L of H_2O (black curve). An OH 3σ peak at a binding energy of 11.0 eV is evident in the spectrum measured after 5 L H_2O on the *r*-TiO_2(110) surface (blue curve). A much lower OH 3σ intensity is found after O_2 dosing and we find that 85±5 % of the capping H atoms can be reacted off, giving an estimate of the degree of perfection of the surface. Consistently, if the surface is subsequently exposed to water at RT there is no increase of the OH 3σ peak intensity.

Fig. 2 (b) shows the corresponding O 1s spectra with the same color-coding as in Fig. 2 (a). The green, red and black curves are identical while the blue curve, measured after 5 L H_2O on the *r*-TiO_2(110) surface, shows an increased intensity at about 532 eV due to surface hydroxyls [32,34,35]. In agreement with previous STM studies [8,12,28,33] we find that (1) water adsorbs through dissociation on O_{br} vacancies at room temperature, (2) a large fraction of the capping H atoms can be

removed through reaction with O_2 and (3) no water adsorption can be detected on the ideal terraces, at RT. The density of O_{br} vacancies in the RT experiment is estimated to 6±1% and the O_2 dose sufficient for complete surface dehydration (5 L) is consistent with that reported earlier (4 L) for an O_{br} density of 5.5±0.2% [33].

The presence of a mixed OH/H_2O monolayer is demonstrated in Fig. 2 (c). The monolayer is prepared by annealing a multilayer of water to 210 K [26]. A pronounced shoulder at 532 eV, related to OH, is observed for both the surface without O_{br} vacancies as well as for the *r*-TiO_2 surface with vacancies. The presence of molecular water is evident on both surfaces, giving rise to the O 1s peak at 534.2 eV. The OH peak is in both cases clearly more intense than the corresponding peak observed for water adsorption at room temperature on the *r*-TiO_2 surface [Fig. 2 (b)]. Clearly there is a mixed layer of dissociative and molecular water on the defect free surface, confirming previous theoretical work [16,19,22].

O 1s spectra monitoring desorption of OH and H_2O from the mixed monolayer on the surface free of O_{br} vacancies are shown in Fig. 3 (a). The O 1s spectra have been recorded at different temperatures and delineated into individual contributions from TiO_2, OH and H_2O. Based on the O 1s intensities at ML coverage [36] the coverage of OH and H_2O are estimated for the different temperatures, Fig. 3 (b). The OH intensity is compensated for the O 1s line profile as well as for the trace amounts of OH that remains after O_2 treatment to produce the surface free of O vacancies (see above). No species originating from the mixed monolayer can be detected on the surface at RT. The absence of water is consistent with previous TPD studies [6,26]. The OH originating from the mixed layer is clearly quite different from the OH formed as OH_{br} at the O vacancies. The latter does not recombine and desorb until about 490 K [6,26].

The OH coverage stays essentially at 0.43 ML up to 210 K. Assuming that all the OH is in the pseudo-dissociated state, 0.22 ML will be accommodated on the OH_t sites. The H_2O coverage at the monolayer point (210 K) is 0.78 ML. This means that the Ti rows comprise 0.22 ML OH_t and 0.78 ML H_2O. In the theoretical treatment the energies of a pure water phase and a mixed phase (with a $OH:H_2O$ ratio of two) were found to be very similar at monolayer coverage [16,19]. Applying this model, we obtain 0.44 ML of the mixed phase and 0.56 ML of the water phase. This suggests rather similar energies with a slightly higher probability for the pure water phase to form. The OH species formed at monolayer coverage is a result of the reduction of the

dissociation barrier induced by intermolecular hydrogen bonding [16,19]. Figure 3 (b) shows that lowering the coverage by heating results in an increased OH:H_2O ratio. Importantly the OH:H_2O ratio of the layer formed by heating the multilayer to 210 K is identical to that found when exposing the surface to water at 210 K. The barrier is thus reduced as the water coverage is reduced as predicted theoretically. Also, the kinetic effects have to be minor.

Our results can be related to the nature of the wetting layer formed at ambient conditions. The O 1s spectrum of a wetting layer on the rutile TiO_2(110) surface was presented recently [35]. Along with molecular water, OH was observed and attributed to vacancy-assisted dissociation. However, assuming a typical amount (5-10 %) of O_{br} vacancies, our results show that the contribution from vacancy-assisted dissociation is much too low to account for the OH peak of the wetting layer. We therefore propose that the OH within the wetting layer stems predominantly from OH within a mixed phase on defect free areas, similar to the monolayer formed under ultrahigh vacuum (UHV) conditions.

Finally, the chemistry of the TiO_2(110) surface may be influenced by Ti interstitials [33]. Although no water adsorption has been related to Ti interstitials at room temperature [33], the effect at low temperatures is as of yet unknown and deserves further study.

In summary, we have demonstrated that the formation of a monolayer of water on a rutile TiO_2(110) surface free from oxygen vacancies at low temperature under UHV conditions involves both molecular and dissociative adsorption. Lower coverages are characterized by an increased OH:H_2O ratio. At room temperature, water adsorption is only possible through dissociation at oxygen vacancies. The mixed nature of the monolayer demonstrates the importance of intermolecular interaction at coverages reached at low temperature in ultra-high vacuum or under ambient wetting conditions.

This work was supported through the Swedish Science Council (VR), the Knut and Alice Wallenberg foundation (KAW), NordForsk and the Crafoord foundation. L.E.W. has been supported through the Strategic Area Materials at NTNU and the Research Council of Norway (project no. 138368/V30). The assistance by the staff at MAX-lab is greatly acknowledged.

References

1. U. Diebold, Surf. Sci. Rep. **48**, 53 (2003).
2. C. L. Pang, R. Lindsay, and G. Thornton, Chem. Soc. Rev. 37, 2328 (2008).
3. A. L. Linsebiegler, G. Lu, and J. T. Yates, Jr., Chem. Rev. **95**, 735 (1995).
4. A. Fujishima and K. Honda, Nature (London) **238**, 37 (1972).
5. M. A. Henderson, Surf. Sci. Rep. **46**, 1 (2002).
6. M. A. Henderson, Surf. Sci. **400**, 203 (1998).
7. C. Di Valentin, G. Pacchioni, and A. Selloni, Phys. Rev. Lett. **97**, 166803 (2006).
8. I. M. Brookes, C. A. Muryn, and G. Thornton, Phys. Rev. Lett. **87**, 266103 (2001).
9. S. Suzuki, K. I. Fukui, H. Onishi, and Y. Iwasawa, Phys. Rev. Lett. **84**, 2156 (2000).
10. R. Schaub *et al*., Phys. Rev. Lett. **87**, 266104 (2001).
11. S. Wendt *et al*., Surf. Sci. **598**, 226 (2005).
12. S. Wendt *et al*., Phys. Rev. Lett. **96**, 066107 (2006).
13. O. Bikondoa *et al*., Nature Mater. **5**, 189 (2006).
14. J. Goniakowski and M. J. Gillan, Surf. Sci. **350**, 145 (1996).
15. P. J. D. Lindan *et al*., Chem. Phys. Lett. **261**, 246 (1996).
16. P. J. D. Lindan, N. M. Harrison, and M. J. Gillan, Phys. Rev. Lett. **80**, 762 (1998).
17. E. V. Stefanovich and T. N. Truong, Chem. Phys. Lett. **299**, 623 (1999).
18. C. Zhang and P. J. D. Lindan, J. Chem. Phys. **118**, 4620 (2003).
19. P. J. D. Lindan and C. Zhang, Phys. Rev. B **72**, 075439 (2005).
20. L. A. Harris and A. A. Quong, Phys. Rev. Lett. **93**, 086105 (2004); P. J. D. Lindan and C. Zhang, *ibid*. **95**, 029601 (2005); L. A. Harris and A. A. Quong, *ibid*. **95**, 029602 (2005).
21. H. Perron *et al*., Surf. Sci. **601**, 518 (2007).
22. W. Zhang *et al*., J. Chem. Phys. **129**, 064703 (2008).
23. P. M. Kowalski, B. Meyer, and D. Marx, Phys. Rev. B **79**, 115410 (2009).
24. W. Wangel, Surf. Sci. **496**, 141 (2002).
25. M. B. Hugenschmidt, L. Gamble, and C. T. Campbell, Surf. Sci. 302, 329 (1994).
26. M. A. Henderson, Surf. Sci. 355, 151 (1996).

27. F. Allegretti *et al*., Phys. Rev. Lett. **95**, 226104 (2005).
28. G. Teobaldi *et al*., Chem. Phys. Lett. **437**, 73 (2007).
29. Y. Du *et al.*, J. Phys. Chem. C **113**, 666 (2009).
30. Y. Du *et al*., Phys. Rev. Lett. **102**, 096102 (2009).
31. J. N. Andersen *et al*., Synchrotron Radiat. News **4**, 15 (1991).
32. The photon flux in the present study is approximately $5 \cdot 10^{10}$ photons mm^{-2}. That no observable radiation damage is found in our data is not surprising given that measurements on water on rutile TiO_2(110) using a flux one order of magnitude greater have been found to lead to minimal radiation damage after 1 hour [25].
33. S. Wendt *et al*., Science **320**, 1755 (2008).
34. L.-Q. Wang *et al*., Surf. Sci. **344**, 237 (1995).
35. G. Ketteler *et al*., J. Phys. Chem. C **111**, 8278 (2007).
36. The monolayer (ML) point is defined as the situation where all Ti(5) sites are occupied by either H_2O or OH. According to the TPD spectrum in ref. [26], this point is reached after heating to about 210 K. Assuming pseudo-dissociation of water the O 1s intensity representing ML coverage of H_2O/OH is obtained as 1xO 1s (H_2O) + 0.5xO 1s (OH).

Figure captions

FIG. 1 (color online). Schematic illustration of the rutile TiO_2(110) surface. Blue and red spheres denote lattice O and Ti, respectively. The light blue spheres are bridging oxygen atoms (O_{br}), which lie in the [001] azimuth of the substrate. One bridging oxygen vacancy is indicated (O_{vac}). Parallel rows that lie between the O_{br} rows are Ti(5) atoms. Green spheres indicate oxygen atoms bonded to H atoms (yellow spheres). Indicated are OH groups on bridging sites (OH_{br}) and on terminal [Ti(5)] sites (OH_t). One water molecule adsorbed on a Ti(5) site is also indicated.

FIG. 2 (color online). (a) OH 3σ spectra for the clean *r*-TiO_2 surface (green curve, measured at elevated temperature), after 5 L H_2O on the *r*-TiO_2 surface (H_2O/*r*-TiO_2(110), blue curve), after a subsequent dose of 5 L O_2 (H_2O+O_2/*r*-TiO_2(110), red curve) and finally after adsorption of another 5 L of H_2O (H_2O/TiO_2(110), black curve). (b) O 1s spectra for the same situations as in (a) and with the same labeling and color-coding. (c) O 1s spectra for the clean surface (green curve), after annealing of a water multilayer on the *r*-TiO_2(110) surface to 210 K (H_2O/*r*-TiO_2(110), blue curve) and after annealing of a water multilayer on the oxygen vacancy free TiO_2(110) surface to 210 K (H_2O/TiO_2(110), black curve).

FIG. 3 (color online). (a) O 1s spectra for water adsorption on a rutile TiO_2(110) surface free from oxygen vacancies. The spectra show the results after progressive heating of a multilayer of water and each spectrum has been delineated into individual contributions from the substrate, OH and H_2O. (b) Estimates of the OH and H_2O coverages given in monolayers (ML) where one ML corresponds to the density of Ti(5) sites on the surface.

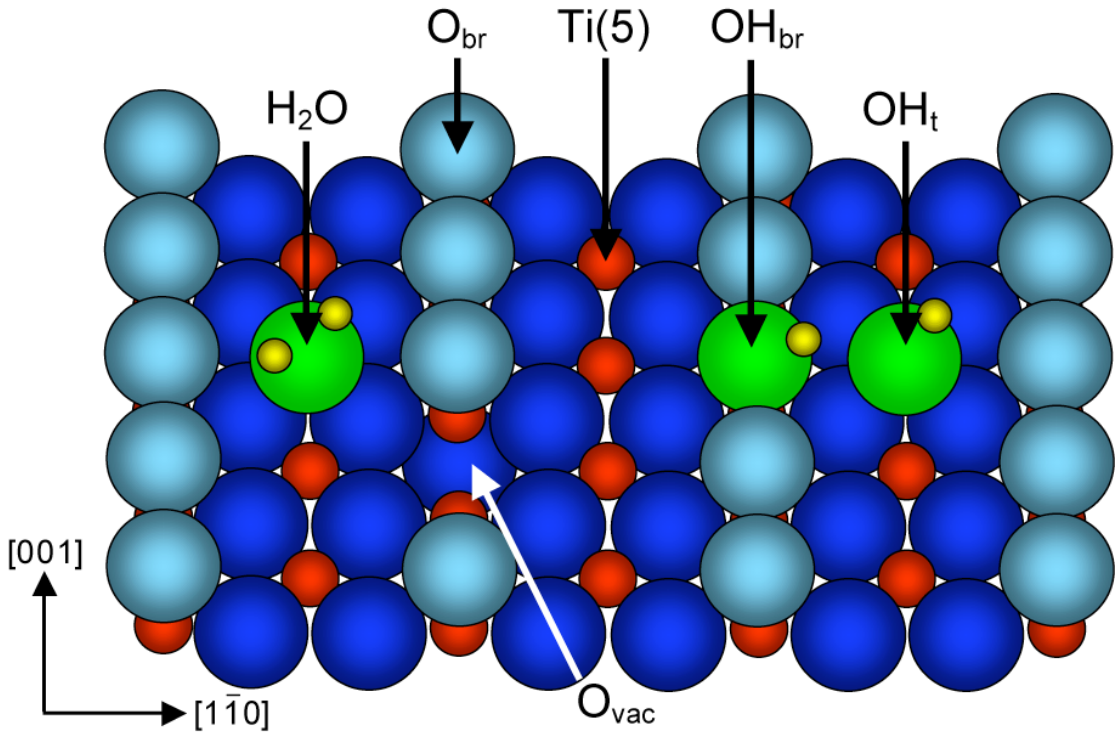

Figure 1
L. E. Walle et al.

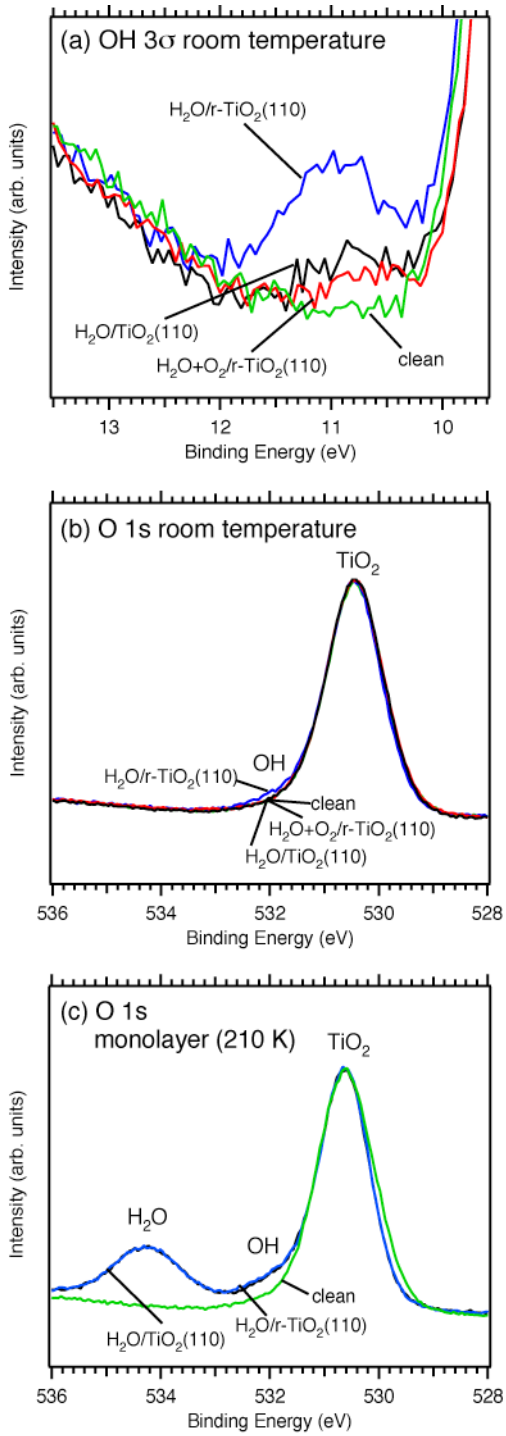

Figure 2
L. E. Walle et al.

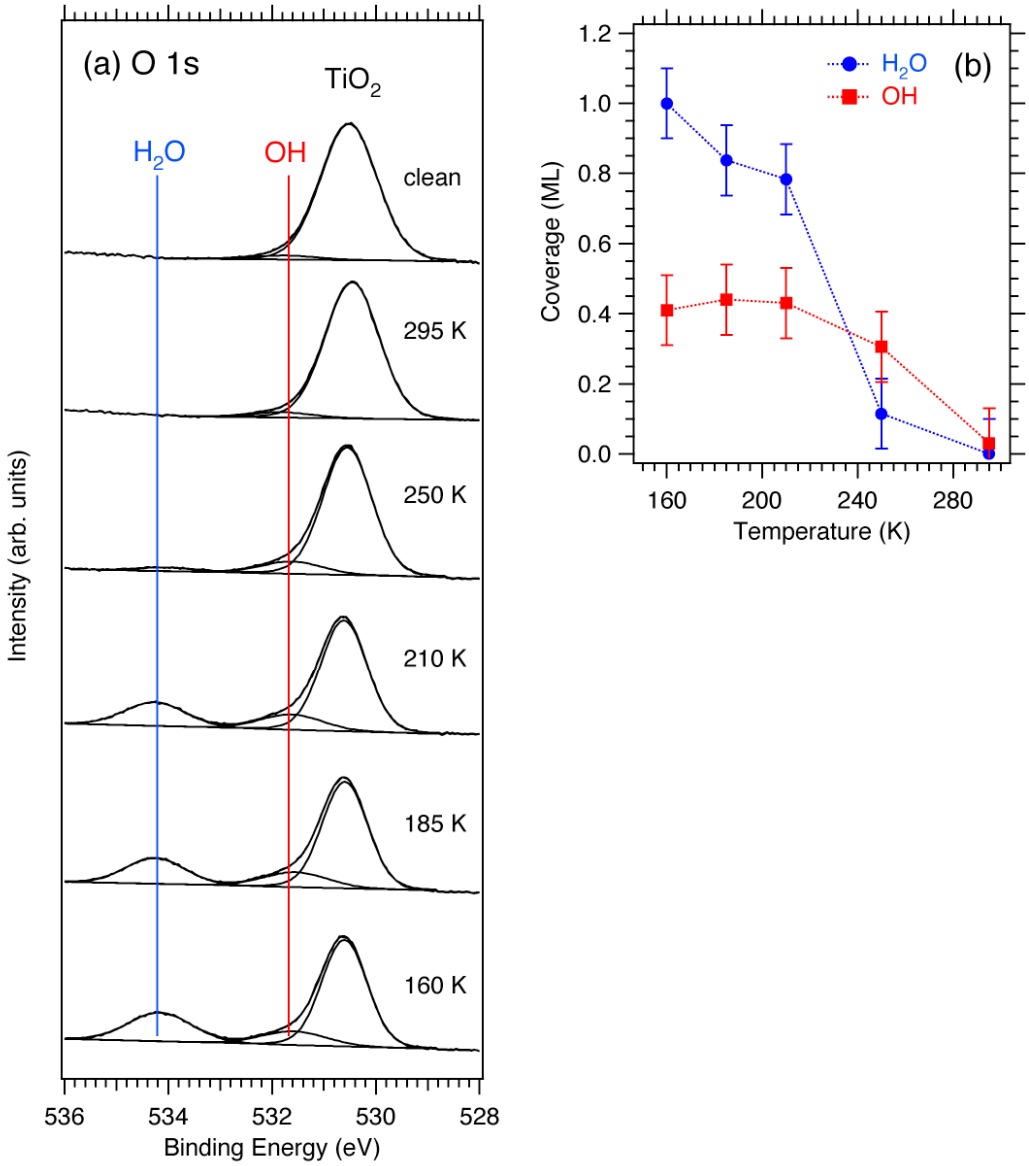

Figure 3
L. E. Walle et al.

Paper IV

Mixed dissociative and molecular water adsorption on single crystal anatase TiO_2 surfaces studied by core level photoemission spectroscopy

L. E. Walle, S. Plogmaker, E. Johansson, A. Borg, P. Uvdal and A. Sandell

In manuscript.

Mixed dissociative and molecular water adsorption on single crystal anatase TiO_2 surfaces studied by core level photoemission spectroscopy

L. E. Walle[1], A. Borg[1], E. M. J. Johansson[2], S. Plogmaker[2], H. Rensmo[2], P. Uvdal[3], and A. Sandell[2,*]

[1] *Dept. of Physics, Norwegian University of Science and Technology, NO-7491 Trondheim, Norway*

[2] *Dept. of Physics and Materials Science, Uppsala University, P. O. Box 530, SE-751 21 Uppsala, Sweden*

[3] *Chemical Physics, Dept. of Chemistry, P.O. Box 124, and MAX-lab, P.O. Box 113, Lund University, SE-221 00 Lund, Sweden*

We demonstrate that the formation of a water monolayer on the anatase TiO_2(101) surface involves both associative and dissociative adsorption. The behavior is similar to that recently found on rutile TiO_2(110) and illustrates the importance of intermolecular interactions. Water adsorption on the (001) surface becomes complex due to the (4x1) reconstruction. Dissociative adsorption occurs on the under-coordinated Ti sites of the ridges while a mixture of molecular and dissociated water is formed either in connection to the ridges or on the terraces.

1. Introduction

One of the most important goals within the area of oxide surface chemistry is to reach a fundamental understanding of the interaction of water with titanium dioxide (TiO_2). The adsorption of water on TiO_2 is central for a wide range of applications, such as catalysis, photochemistry, electrochemistry, corrosion and biocompatible materials [1-4]. With respect to fundamental studies, water adsorption on single crystalline rutile TiO_2(110) can be considered as the prototype system, owing to the readily available high quality samples [2,5]. The extensive experimental and theoretical methods developed to explore the H_2O/TiO_2(110) system can furthermore be regarded as central for how to model the interaction of water with oxide surfaces in general.

The emergence of nanoscience has however put the focus on the anatase polymorph of TiO_2. Nanoporous TiO_2 electrodes can be prepared by forming a network of sintered nanoparticles. These have been shown to be most useful for photoelectrochemical applications by virtue of the huge effective surface area [6]. It has been found that anatase is the preferred phase of TiO_2 nanoparticles [7]. Moreover, anatase TiO_2 appears to be an even more potent photocatalyst than rutile [8-10]. The equilibium shape of an anatase crystallite exposes (101) and (001) surfaces, of which the latter is the minority termination [1]. Consequently, comparative studies of water adsorption on well-defined anatase surfaces is a stepping stone towards an understanding of surface processes on nanocrystalline TiO_2 in aqueous environments. There are however very few experimental studies of water adsorption on single crystalline anatase TiO_2.

The anatase TiO_2(101) surface is found to exhibit a bulk terminated, unreconstructed (1x1) surface when prepared in ultra-high vacuum (UHV) [11]. The anatase TiO_2(101)-(1x1) surface is schematically depicted in Figure 1 (a). The adsorption of water on the anatase (101) surface in UHV has previously been studied using x-ray photoelectron spectroscopy (XPS) and temperature-programmed desorption (TPD) [12]. The TPD spectrum displayed desorption states at 160, 190 and 250 K. These were assigned to multilayer water, water adsorbed on 2-fold-coordinated (bridge) O, and water adsorbed on 5-fold-coordinated Ti [Ti(5)], respectively. No evidence for water dissociation was found in the O 1s XPS spectra, which was also suggested in an earlier theoretical study [13].

The clean (001) surface of anatase TiO_2 undergoes a (4x1) reconstruction in UHV [14,15]. A structure model of the TiO_2(001)-(4x1) surface has been derived from scanning tunneling microscopy (STM) results in conjunction with DFT calculations [16,17]. This structure model is shown in Figure 1 (b). The surface can be described as consisting of ridges, made up by TiO_3 chains, separated by terraces. The Ti atoms of the ridges are only four-fold coordinated [Ti(4)] while the terrace Ti atoms are five-fold coordinated. Consequently, the ridges have been found to be very reactive upon adsorption. Calculations demonstrate that water dissociates at the ridges but not at the terraces [18]. We have recently demonstrated experimentally that the ridges are indeed highly active towards water dissociation [19]. Using O 1s photoelectron spectroscopy (PES) we showed that water dissociates on the anatase TiO_2(001)-(4x1) surface at low coverage and that the OH coverage shows a good correspondence to the density of four-fold coordinated Ti sites. That is, this structure contains terminally adsorbed OH (OH_t) on Ti(4) sites as illustrated in Figure 1 (b). At higher coverages, we found evidence for a mixed phase consisting of dissociated and molecular water but the exact nature of this phase could not be elucidated.

In summary, the available experimental and theoretical results show that the interaction of water with the TiO_2(101)-(1x1) and TiO_2(001)-(4x1) surfaces of anatase TiO_2 is very different. The current view is that adsorption of water on the (101)-(1x1) surface is purely molecular while dissociation takes place on the (001)-(4x1) surface.

Returning to the rutile TiO_2(110) surface the adsorption state of water has been subject to an intense debate. While the efficient dissociation of water on the oxygen deficient TiO_2(110) surface has been characterized in detail [20-27], there is as of yet no consensus reached between experimentalists and theorists whether water dissociates or not upon adsorption on a defect-free TiO_2(110) surface. Very recently, we demonstrated that mixed molecular and dissociative water adsorption occurs at monolayer coverage on a rutile TiO_2(110) surface free from oxygen vacancies [28]. The dissociated water is most likely in the form of an OH_{br}–OH_t pair. This configuration, included in Figure 1, is often denoted pseudo-dissociated water. The OH_{br}–OH_t pair is not stable at room temperature [28,29] in contrast to the OH_{br} groups formed at oxygen vacancy sites, which remain on the surface up to 490 K [20,30]. The formation of a layer that comprises molecular and (pseudo-) dissociated water is believed to be the result of intermolecular interactions [31,32]. The finding of

such a mechanism on the rutile TiO_2(110) surface makes it highly motivated to perform further studies on the adsorption of water on anatase surfaces.

In this study, we make a side-by-side comparison of the temperature dependent adsorption state of water on the (101)-(1x1) and (001)-(4x1) surfaces of anatase TiO_2. Using extremely surface sensitive synchrotron radiation excited O 1s photoemission spectra, we demonstrate that the formation of a water monolayer on the anatase TiO_2(101) surface involves both associative and dissociative adsorption. This suggests that the mechanism leading to dissociation within the monolayer on rutile (110) is also present for the anatase (101) surface. We also continue the discussion on the nature of the water layer on the (001) surface. Dissociation occurs on the ridges of the (4x1) reconstruction but the high complexity of the surface prevents a clear assignment of the location of all the OH groups.

2. Experimental

The measurements were performed at beamline D1011 at the Swedish National Synchrotron Facility MAX II [33]. The end station comprises a Scienta 200 mm radius hemispherical electron energy analyzer. The presented O 1s spectra were recorded in 60° off normal emission using 610 eV photons. Binding energy (BE) calibration of the core level photoelectron (PES) spectra against the Fermi level was achieved by referencing to a Pt foil mounted on the sample holder.

The anatase TiO_2(101) and (001) single crystals (supplied by SurfaceNet GmbH) were cleaned by cycles of Ar-sputtering and subsequent annealing in oxygen to 650°C. The formation of the (4x1) reconstruction characteristic for the anatase (001) surface was confirmed with low energy electron diffraction (LEED). A sharp (1x1) LEED pattern was observed for the (101) surface. This cleaning procedure results in a very low surface defect density according to PES spectra [34]. That is, the Ti 2p spectrum displayed only a Ti^{4+} state and no discernable structures were found in the band gap region.

Pure water was introduced through a leak valve, backfilling the chamber. Doses are given in Langmuirs (1 L = $1 \cdot 10^{-6}$ Torr·sec). Annealing of the adsorbate layer was performed by increasing the temperature to the desired value at a rate of about 1 K per second and then kept at this temperature for 60 seconds. Measurements

were started immediately after heating in order to reduce the effects of water re-adsorption. The two samples were mounted together on a common sample holder. Thus, they were exposed to identical amounts of water and heated to similar temperatures for identical time periods. This arrangement furthermore optimizes the ability to make direct quantitative comparisons of spectral intensities, which otherwise may prove difficult when measuring at a synchrotron radiation source.

3. Results and discussion

Figures 2 (a) and (b) show surface sensitive O 1s spectra obtained after adsorption and subsequent annealing of a water multilayer on the anatase TiO_2 (101)-(1x1) and (001)-(4x1) surfaces, respectively. The spectra have been delineated into individual contributions from the TiO_2 substrate, OH and H_2O. We will initially focus on the results for the (101) surface. After adsorption of water at 120 K followed by heating to 160 K in order to desorb multilayer water two O 1s features are observed apart from the TiO_2 substrate peak at 530.5 eV. The state at 531.5 eV can be assigned to OH and the state at 534 eV to H_2O. It is clear that the water monolayer consists of both species since both OH and H_2O are present between 160 K and 260 K. At 160 K, multilayer water has desorbed and bonding to substrate atoms, i.e. bridge bonded O and surface Ti(5) atoms, is the only possibility. Above 190 K bonding to surface Ti(5) atoms strongly dominates according to the previous TPD results [12]. The O 1s peak due to molecular water vanishes after heating to 300 K, which is in good agreement with the previous study [12].

The appearance of an OH related feature is a striking result since it is in apparent contradiction to theoretical calculations and the previous XPS study [12,13]. However, from an experimental point of view our observation of the OH related peak is most likely by virtue of the optimized measurement conditions. The low surface sensitivity (and worse resolution) in conventional XPS causes the OH peak to become obscured by the substrate signal. We can therefore conclude that the water layer attained by adsorption and subsequent annealing of a multilayer contains a mixture of molecular and dissociated species. From this follows that the mechanism responsible for creating a mixed phase on the rutile TiO_2(110) surface is most probably also operating for the water layer on the anatase TiO_2(101) surface. That is, intermolecular

hydrogen bonding lowers the dissociation barrier, which leads to partial dissociation [28,31,32].

The O 1s spectra for water adsorption and subsequent annealing on the anatase TiO_2(001)-(4x1) surface show the same general behavior as those obtained for the (101)-(1x1) surface. That is, a mixture of H_2O and OH is found at lower temperatures. At higher temperature adsorbed H_2O vanishes leaving OH as the only adsorbed species. The results are in good agreement with our previous study [19]. In contrast to the (101) surface, the presence of OH is not unexpected since the four-fold coordinated Ti atoms on the ridges of the (4x1) reconstruction are expected to be very reactive [18].

The next step is to quantify the water and hydroxyl coverages based on the O 1s intensities. It is common to define one monolayer (ML) as equal to the density of Ti surface sites available for adsorption. Consequently, a monolayer reference point is needed. However, the TPD spectrum for H_2O/anatase TiO_2(101) shows a complex desorption behavior; the structure associated with desorption from bridging oxygen sites is overlapping with the structure associated with desorption from Ti sites [12]. This makes it difficult to prepare a monolayer without the presence of a partial layer bonded to bridging oxygens. In contrast, the TPD spectrum for H_2O/rutile TiO_2(110) shows that the monolayer point is relatively well-defined since there is a clear dip between the desorption structure from bridging oxygen sites and the desorption structure from Ti sites [20,30]. The coverage estimates in the present work were therefore made by using the O 1s data recorded for water adsorption on the rutile TiO_2(110) surface using the same experimental parameters [28].

The dissociated state on the defect-free rutile TiO_2(110) surface consists as previously mentioned of one terminal OH (OH_t) at a Ti(5) site and a hydrogen atom adsorbed on a neighboring O_{br} site, giving a bridging OH (OH_{br}) [26,31,32]. Since the two OH groups remain neighbors, see Figure 1, the state has been denoted “pseudo-dissociated”. For a mixture of molecular and pseudo-dissociated water the O 1s intensity representing the density of occupied Ti sites is obtained by:

$$\text{O 1s (Ti)} = 1\text{x O 1s } (H_2O) + 0.5\text{x O 1s (OH)} \qquad (1)$$

For a monolayer on the rutile TiO_2(110) surface the O 1s intensity calculated in this way defines a coverage corresponding to the Ti(5) density, which is $5.2 \cdot 10^{14}$

cm^{-2}. Thus, by normalizing to the results for a monolayer of water adsorbed on rutile TiO_2(110), OH and H_2O coverages on the anatase surfaces can be calculated [35]. The results are shown in Figure 3.

The OH coverage on the (101) surface is found to be close to constant in the temperature regime 160 – 200 K, with a density of about $3.1 \cdot 10^{14}$ OH/cm^2. At higher temperatures the OH coverage decreases but at much lower rate than the H_2O coverage. The decrease in OH density signals desorption of first layer species, from which follows that the last temperature at which the first layer is complete is 200 K. At this point, however, Figure 3 shows that the H_2O density is $6.7 \cdot 10^{14}$ cm^{-2}, which exceeds the density of Ti(5) sites on the anatase (101) surface ($5.2 \cdot 10^{14}$ cm^{-2}). That is, the coverage is greater than one monolayer. Increasing the temperature to 230 K leads to a dramatic decrease of adsorbed H_2O and a slight decrease of the OH coverage. Adding the O 1s intensities using (1) yields that the density of occupied Ti sites is now $5.1 \cdot 10^{14}$ cm^{-2}, which is close to the monolayer density. That monolayer density is obtained at a temperature at which some of the OH has desorbed can be taken as a result of the complex desorption behavior mentioned above. A small amount of OH is finally detected on the anatase TiO_2(101) surface even after annealing to 400 K. This is not expected from the previous TPD results [12]. We cannot exclude that re-adsorption is the cause for the observation of a small OH related peak after this annealing.

Concerning the (001)-(4x1) surface it is highly motivated to first compare the present coverage estimate, obtained by normalization to the monolayer on the rutile TiO_2(110) surface, with that in our previous study where the angular dependence of the relative O 1s intensities was used [19]. In the present study, Figure 3 gives an estimate of $1.6 \cdot 10^{14}$ OH/cm^2 after heating to 300 K. The value presented in our previous work corresponds to a density of $1.7 \cdot 10^{14}$ OH/cm^2, that is, the agreement is very good.

The detailed temperature dependences of the H_2O and OH coverages are different for the two surfaces. The density of molecularly adsorbed water on the (001) surface is lower than on the (101) surface up to a temperature of 260 K. The OH coverage on the (001) surface is higher than on the (101) surface within the whole temperature range shown in Fig. 3. In addition, the OH coverage on the (001) surface displays a maximum after heating to 180 K, rather than the plateau found in curve showing the OH coverage on the (101) surface. The reason for having a maximum is

not clear. A plausible explanation is that the O 1s intensity from all or a part of the OH groups becomes attenuated by second layer water. It is not unlikely that the attenuation effect is different on the two surfaces due to the geometric differences, especially since the (001) surface is reconstructed.

It is very difficult to obtain a detailed understanding of the water interaction with the (001)-(4x1) surface based on the present results. The main complication is the inhomogeneous properties of the (4x1) reconstructed surface. As previously noted, the four-fold coordinated Ti atoms on the ridges are expected to be very reactive, leading to water dissociation. However, the (4x1) reconstruction causes the five-fold coordinated Ti atoms on the terraces to be pushed slightly inwards, towards the bulk, which will reduce the interaction strength with adsorbates as compared to the unreconstructed surface. Moreover, the Ti(5) atoms on the terraces are not identical; the Ti atoms adjacent to the ridges are located even further below the neighboring bridging O atoms than the Ti atoms located in the center of the terrace. That is, the (4x1) reconstructed surface comprises three different types of Ti atoms for which the interaction strength with adsorbates may vary considerably.

In our previous work, the OH coverage remaining after heating to 300 K was consistent with one OH bonded to each ridge Ti, i.e. this is the most strongly interacting species. This result is well reproduced in the present work since the density of ridge atoms is $1.7 \cdot 10^{14}$ cm^{-2} and the OH density after heating to 300 K is $1.6 \cdot 10^{14}$ cm^{-2}. We have also shown that the uptake, if undertaken at 190 K, is characterized by rapid filling of the Ti(4) ridge sites with one OH at each site. Continued exposure leads to adsorption of H_2O and OH with an intensity ratio close to one. The reverse process to this second adsorption step, i.e. upon desorption, can be seen in Fig. 3 where the H_2O and OH coverages appear to be rather well correlated in the temperature regime 200-300 K.

We can only speculate on the location of the H_2O and OH species associated with the desorption between 200-300 K. The OH and H_2O desorbing in this temperature regime correspond to densities of $2.3 \cdot 10^{14}$ cm^{-2} and $2.0 \cdot 10^{14}$ cm^{-2}, respectively, in good agreement with our previous results [19]. These values are very low with respect to the density of Ti(5) atoms on the terraces ($6.98 \cdot 10^{14}$ cm^{-2}). This fact, together with the presumed low reactivity of the terraces has lead us to the conclusion that these species are interacting with the ridge atoms or with the OH adsorbed on the ridge atoms. However, after finding partial dissociation on the rutile

(110) surface [28] that is most likely induced by the intermolecular interactions, the formation of a mixed layer on the terraces is a definite possibility. Considering that the central Ti atoms on the terraces may be more reactive than the others, partial population of terrace sites is possible. The density values are compatible with such a scenario.

It is finally important to note that the preparation of (natural) anatase samples has far from reached the level of sophistication found for the grown rutile TiO_2 samples. Impurities on a percentage level are present and the character of defects and how they can be avoided are issues that deserve further studies. It is for example plausible that the cleaning method employed here, with O_2 treatment, leads to the presence of oxygen ad-atoms. Preliminary results on gold growth on the (101) surface show the presence of oxidized gold, possibly formed by interaction with oxygen ad-atoms. However, the coverage associated with this defect is only of the order of a few percent.

4. Conclusions

In summary, we have demonstrated that the formation of a water monolayer on the anatase TiO_2(101) surface involves both associative and dissociative adsorption. The behavior is similar to that on rutile TiO_2(110) and illustrates the importance of intermolecular interactions present at higher coverages. The exact composition of the monolayer on the anatase TiO_2(101) surface is however difficult to deduce due to simultaneous desorption of first and second layer water. The (001) surface is more reactive towards water dissociation than the (101) surface. The higher activity can to a large extent be ascribed to the very reactive ridges of the (4x1) reconstruction, comprising four-fold coordinated Ti atoms. The terraces are less active but adsorption of a mixture of a mixed molecular and dissociated phase cannot be excluded.

Acknowledgements

We thank the staff at MAX-lab for their assistance. This work has been supported through the Swedish Science Council (VR), the Knut and Alice Wallenberg foundation (KAW), the Crafoord foundation, NordForsk and the Göran Gustafsson

foundation. L.E.W. has been supported through the Strategic Area Materials at NTNU.

References

1. U. Diebold, Surf. Sci. Rep. **48**, 53 (2003).
2. C. L. Pang, R. Lindsay, and G. Thornton, Chem. Soc. Rev. **37**, 2328 (2008).
3. A. L. Linsebiegler, G. Lu, and J. T. Yates, Jr., Chem. Rev. **95**, 735 (1995).
4. A. Fujishima and K. Honda, Nature (London) **238**, 37 (1972).
5. M. A. Henderson, Surf. Sci. Rep. **46**, 1 (2002).
6. B. O´Regan and M. Grätzel, Nature (London) **353**, 737 (1991); A. Hagfeldt and M. Grätzel, Chem. Rev. **95**, 49 (1995).
7. C. J. Taylor, D. C. Gilmer, D. G. Colombo, G. D. Wilk, S. A. Campbell, J. Roberts, W. L. Gladfelter, J. Am. Chem. Soc. **121**, 5220 (1999).
8. O. Carp, C. L. Huisman, and A. Reller, Prog. Solid State Chem. **32**, 33 (2004).
9. A. L. Linsebigler, G. Lu, and J. T. Yates, Chem. Rev. **95**, 735 (1995).
10. L. Kavan, M. Grätzel, S. E. Gilbert, C. Klemenz, and H. J. Scheel, J. Am. Chem. Soc. **118**, 6716 (1996).
11. W. Hebenstreit, N. Ruzycki, G. S. Herman, Y. Gao, and U. Diebold, Phys. Rev. B **62**, R16334 (2000).
12. G. S. Herman, Z. Dohnálek, N. Ruzycki, and U. Diebold, J. Phys. Chem. B **107**, 2788 (2003).
13. A. Vittadini, A. Selloni, F. P. Rotzinger, and M. Grätzel, Phys. Rev. Lett. **81**, 2954 (1998).
14. G. S. Herman, M. R. Sievers, and Y. Gao, Phys. Rev. Lett. **84**, 3354 (2000).
15. Y. Liang, Y. Gan, S. A. Chambers, E. I. Altman, Phys. Rev. B **63**, 235402 (2001).
16. M. Lazzeri and A. Selloni, Phys. Rev. Lett. **87**, 266105 (2001).
17. R. E. Tanner, A. Sasahara, Y. Liang, E. I. Altman and H. Onishi, J. Phys. Chem. B **106**, 8211 (2002).
18. X.-Q. Gong, A. Selloni, and A. Vittadini, J. Phys. Chem. B **110**, 2804 (2006).
19. J. Blomquist, L. E. Walle, P. Uvdal, A. Borg, and A. Sandell, J. Phys. Chem. C **112**, 16616 (2008).
20. M. A. Henderson, Surf. Sci. **400**, 203 (1998).

21. C. Di Valentin, G. Pacchioni, and A. Selloni, Phys. Rev. Lett. **97**, 166803 (2006).
22. I. M. Brookes, C. A. Muryn, and G. Thornton, Phys. Rev. Lett. **87**, 266103 (2001).
23. S. Suzuki, K. I. Fukui, H. Onishi, and Y. Iwasawa, Phys. Rev. Lett. **84**, 2156 (2000).
24. R. Schaub, P. Thostrup, N. Lopez, E. Lægsgaard, I. Stensgaard, J. K. Nørskov, and F. Besenbacher, Phys. Rev. Lett. **87**, 266104 (2001).
25. S. Wendt, R. Schaub, J. Matthiesen, E. K. Vestergaard, E. Wahlström, M. D. Rasmussen, P. Thostrup, L. M. Molina, E. Lægsgaard, I. Stensgaard, B. Hammer, and F. Besenbacher, Surf. Sci. **598**, 226 (2005).
26. S. Wendt, J. Matthiesen, R. Schaub, E. K. Vestergaard, E. Lægsgaard, F. Besenbacher, and B. Hammer, Phys. Rev. Lett. **96**, 066107 (2006).
27. O. Bikondoa, C. L. Pang, R. Ithnin, C. A. Muryn, H. Onishi, and G. Thornton, Nature Mater. **5**, 189 (2006).
28. L. E. Walle, A. Borg, P. Uvdal, and A. Sandell (to be submitted).
29. Y. Du, A. Deskins, Z. Zhang, Z. Dohnálek, M. Dupuis, and I. Lyubinetsky, J. Phys. Chem. C **113**, 666 (2009).
30. M. A. Henderson, Surf. Sci. **355**, 151 (1996).
31. P. J. D. Lindan, N. M. Harrison, and M. J. Gillan, Phys. Rev. Lett. **80**, 762 (1998).
32. P. J. D. Lindan and C. Zhang, Phys. Rev. B **72**, 075439 (2005).
33. J. N. Andersen, O. Björneholm, A. Sandell, R. Nyholm, J. Forsell, L. Thånell, A. Nilsson, and N. Mårtensson, Synchrotron Radiat. News **4**, 15 (1991).
34. A. Sandell, B. Sanyal, L. E. Walle, J. H. Richter, S. Plogmaker, P. G. Karlsson, A. Borg and P. Uvdal, Phys. Rev. B **78**, 075113 (2008).
35. The integrated O 1s intensities of the clean rutile TiO_2(110) and anatase TiO_2(101) surfaces should furthermore be very similar, providing an independent check of the experimental conditions at hand.

Figure captions

FIG. 1. Schematic illustration of (a) the anatase TiO_2(101)-(1x1) surface and (b) the anatase TiO_2(001)-(4x1) surface. The rectangles define areas of (10.24×7.57) $Å^2$ and (15.14×7.57) $Å^2$, respectively. Blue and red spheres denote lattice O and Ti, respectively. The light blue spheres are bridging oxygen atoms (O_{br}). The coordination number of the Ti atoms is given in parentheses. Green spheres indicate oxygen atoms bonded to H atoms (yellow spheres). Indicated are OH groups on bridging sites (OH_{br}) and on terminal (Ti) sites (OH_t). Molecular water molecules adsorbed on Ti(5) sites are also indicated. The shaded areas of the (001)-(4x1) define the ridges associated with the surface reconstruction.

FIG. 2. O 1s spectra for water adsorption on (a) the anatase TiO_2(101)-(1x1) surface and (b) the anatase TiO_2(001)-(4x1) surface. The spectra show the results after progressive heating of a multilayer of water and each spectrum has been delineated into individual contributions from the TiO_2 substrate, OH and H_2O.

FIG. 3. Estimates of the OH and H_2O densities (in molecules per cm^2) on the anatase TiO_2(101)-(1x1) and TiO_2(001)-(4x1) surfaces as a function of temperature.

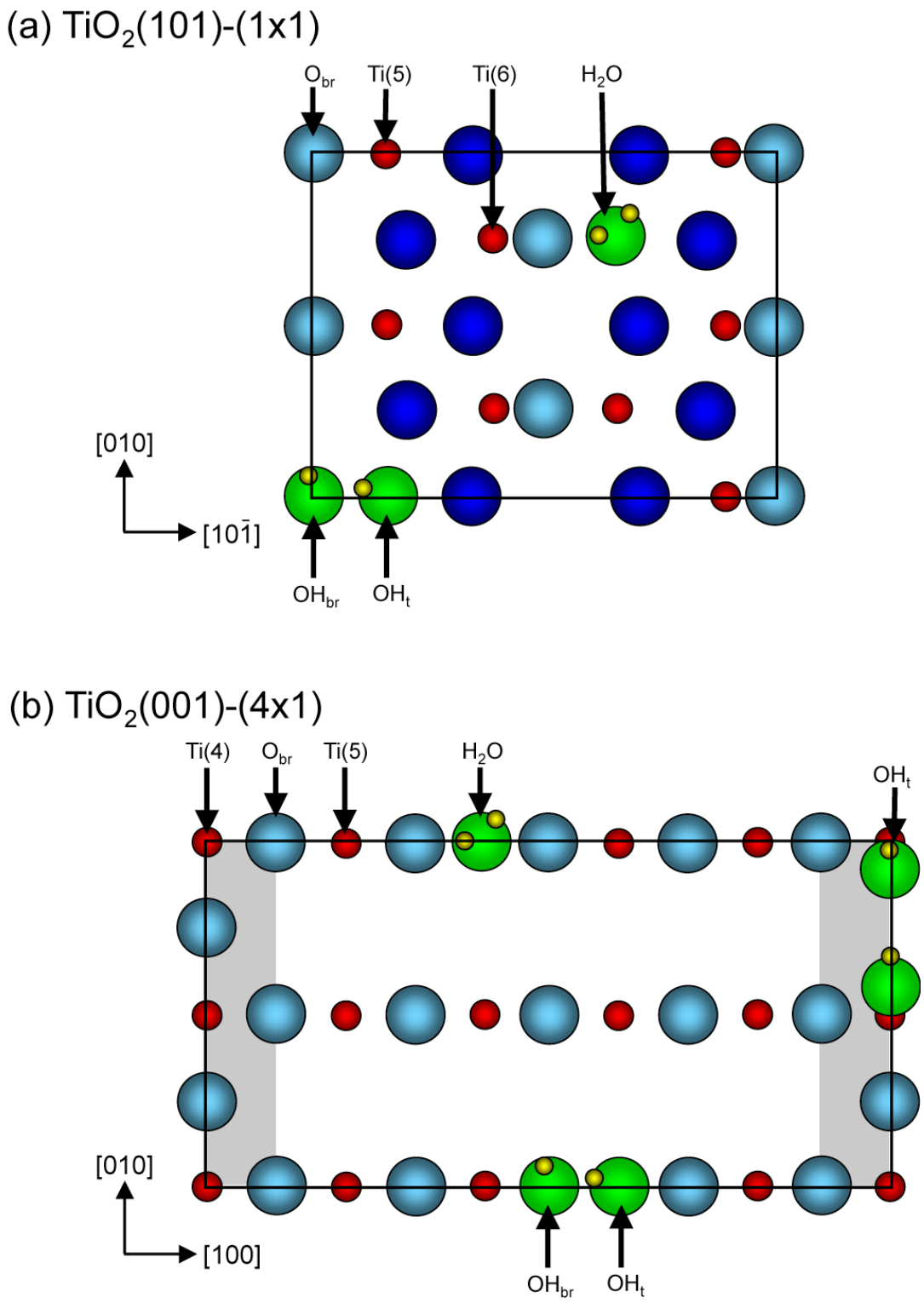

Figure 1 L E Walle et al

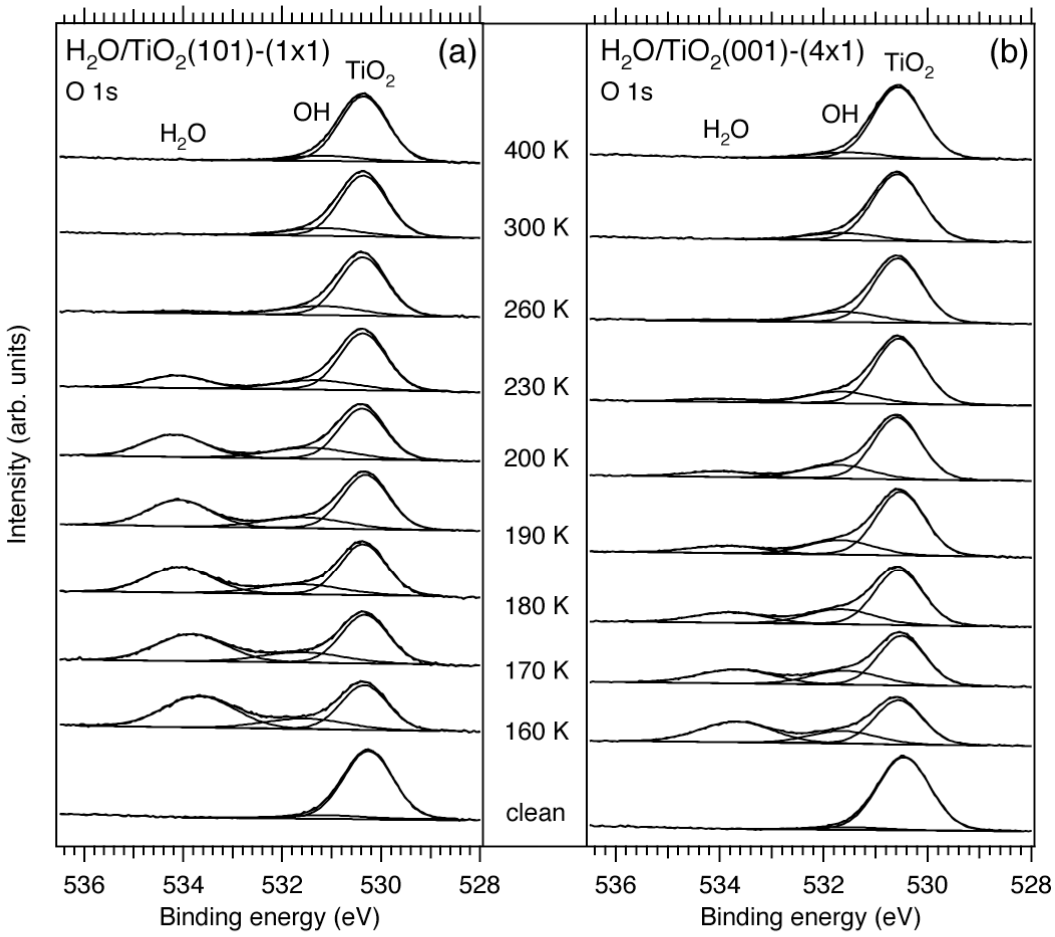

L E Walle et al
Figure 2

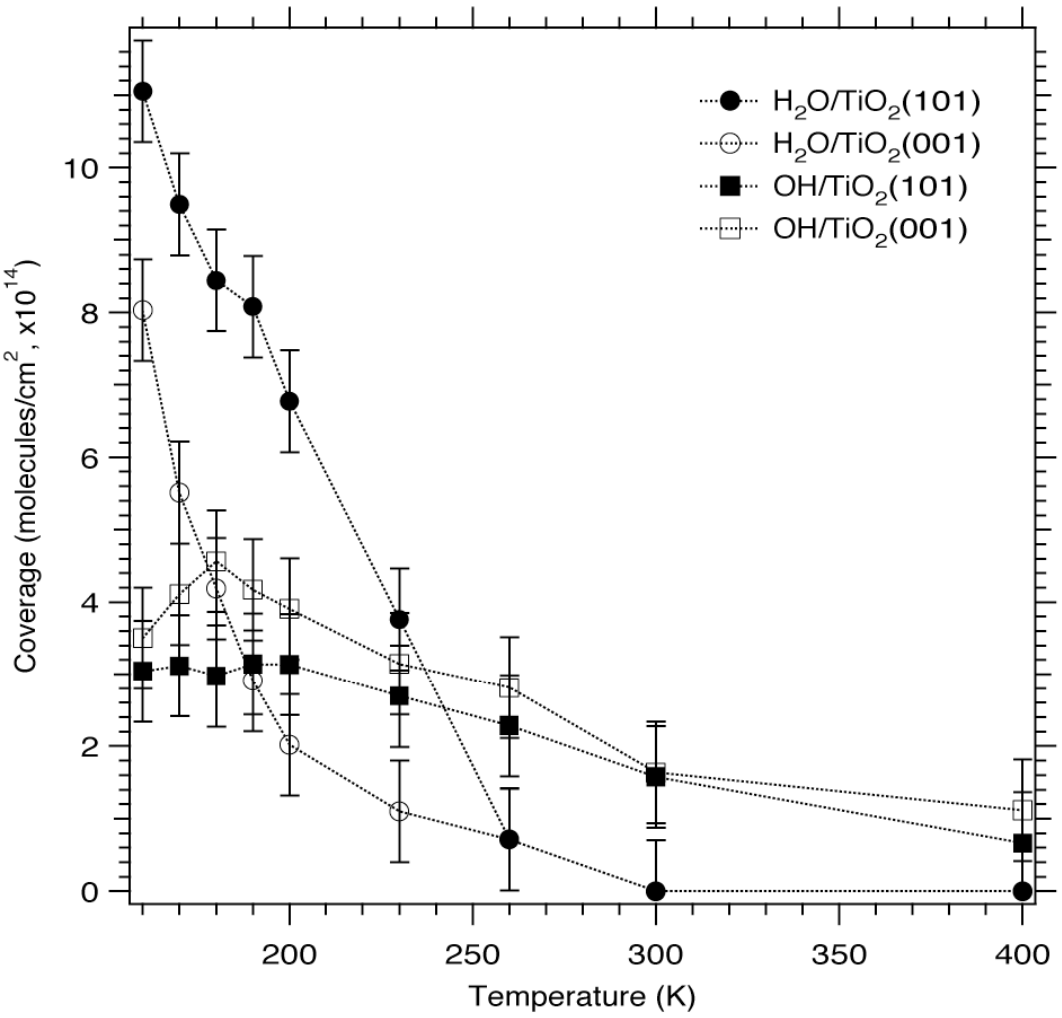

L E Walle et al
Figure 3

Paper V

Growth of Au on Single Crystalline Anatase TiO_2(101): Formation of oxidized gold

L. E. Walle, S. Plogmaker, A. Borg and A. Sandell

In manuscript.

Growth of Au on Single Crystalline Anatase TiO_2(101): Formation of oxidized gold

L. E. Walle[1], S. Plogmaker[2], A. Borg[1] and A. Sandell[2,*]

[1] *Dept. of Physics, Norwegian University of Science and Technology, NO-7491 Trondheim, Norway*

[2] *Dept. of Physics and Materials Science, Uppsala University, P. O. Box 530, SE-751 21 Uppsala, Sweden*

By using high resolution core level photoelectron spectroscopy to study submonolayer growth of gold and its interaction with CO on the anatase TiO_2(101) surface, we show that two different kinds of Au aggregates are formed. The first type is characterized by an Au $4f_{7/2}$ binding energy of 84.8±0.1 eV and a CO induced shift of 1.5 eV. This type of particle is only observed up to a coverage of 0.14 ML. The second particle type has an Au $4f_{7/2}$ binding energy of 84.1±0.1 eV and a CO induced shift of 0.9 eV. It is first observed at 0.14 ML and continues to grow at higher Au coverages, exhibiting a decreasing relative CO uptake with increasing Au dose, which is typical for an increasing particle size. We propose that the first particle type contains oxidized gold and the low coverage suggests nucleation at defects, possibly oxygen ad-atoms located on the terraces. The oxidized gold aggregates appear to be size-limited. The second type is attributed to neutral gold that most probably nucleate at steps on the anatase TiO_2(101) surface.

*Corresponding author. Email: anders.sandell@fysik.uu.se; Fax: +46 18 4713524

1. Introduction

Gold has for a long time been regarded as an inert material of little use as catalyst [1]. However, in the last decade gold nanoparticles have begun to garner attention for their unique catalytic properties [2,3]. Supported gold particles on metal oxides have been shown to be effective catalysts for several processes, including CO oxidation [4], NO reduction [5] and the water gas shift reaction [6]. The oxidation of CO has been found to take place at remarkably low temperatures [4,7-10]. Most significant is the strong size dependence, particles below 5 nm in size are far superior to larger particles in terms of catalytic activity [8,11,12]. Titanium dioxide is one of the metal oxides which have been studies most intensively over the last decades, both due to its physical properties and as catalyst support. The detailed mechanism behind the CO oxidation process on the Au/TiO_2 system is still largely an enigma. Many studies have suggested under-coordinated Au atoms [13], surface defects [14] and the $Au\text{-}TiO_2$ interface [15] as reactive sites. A fundamental understanding of the growth mechanism of Au clusters on TiO_2 and the nature of the Au/TiO_2 bond is thus of great importance.

Up till now most experimental studies of Au particles on single crystal TiO_2 have been done on the rutile phase, due to the good availability of high quality rutile single crystals. On the other hand, the anatase TiO_2 polymorph seems to be the preferred phase when forming nanosized particles [16] and applied systems almost exclusively comprise anatase TiO_2 nanostructures. Hence model studies of Au on single crystalline anatase TiO_2 are highly motivated. A pioneering experimental study addressing the deposition of Pt and Au on the single crystalline anatase $TiO_2(101)$ surface was published very recently [17]. Using Scanning Tunneling Microscopy (STM), it was found that deposition of Au at room temperature predominantly results in the formation of large clusters that nucleate on step edges. The creation of surface oxygen vacancies had a dramatic influence on the growth. In this case, Au particles formed at the vacancy sites, resulting in particles preferentially located on the terraces. In this respect, the anatase $TiO_2(101)$ surface is very similar to the rutile $TiO_2(110)$ surface. Defect sites on rutile $TiO_2(110)$, either in the form of oxygen vacancies or oxygen ad-atoms, have been found to interact very strongly with Au atoms [14]. In the absence of defects, Au prefers to nucleate at the step edges. That is, the minority sites, i.e. those that deviate from the ideal terrace sites, appear to be

critical for the growth of Au on both the anatase TiO_2(101) and rutile TiO_2(110) surfaces.

In this work, we use synchrotron based core level photoelectron spectroscopy to study the submonolayer growth of gold and its interaction with CO on the single crystalline anatase TiO_2(101) surface. We identify two different Au particle types, one defect related minority type, which is only observed up to an Au coverage of 0.14 ML. It appears to be size-limited and has a constant relative CO uptake. A second particle type is first observed at 0.14 ML Au. These aggregates continue to grow at higher Au coverages and exhibit a decreasing relative CO uptake with increasing Au dose. We attribute the first particle type to oxidized gold, nucleating at oxygen ad-atoms at the terraces, while the second type is neutral gold particles growing at steps.

2. Experimental

High resolution synchrotron radiation photoemission spectroscopy measurements were performed at beamline I311 of the MAX II storage ring at the Swedish National Synchrotron Laboratory in Lund, Sweden. The beam line is equipped with a modified Zeiss SX-700 monochromator and a 200 mm radius hemispherical electron energy analyzer of Scienta type [18]. The base pressure of the UHV chamber was about $2 \cdot 10^{-10}$ mbar.

The anatase TiO_2(101) single crystal (supplied by PI-KEM Ltd., UK) was cleaned by cycles of argon sputtering followed by annealing at 920 K in oxygen ($p = 5 \cdot 10^{-7}$ mbar) and cooling the crystal down in the oxygen atmosphere. The procedure gave a clean and well-defined surface, as judged from photoemission measurements of the C 1s and Ti 2p core level regions and the valence region, and observed low energy electron diffraction (LEED) patterns. The Ti 2p spectrum showed only a Ti^{4+} state and no discernible structures were observed in the band gap region, indicating a very low defect density of the pristine surfaces. Figure 1 shows the LEED pattern for the anatase surface, which is bulk terminated and exhibits a (1x1) LEED pattern [19].

Gold was evaporated from a tungsten crucible heated by electron bombardment, and the evaporation rate was measured with a quartz crystal microbalance at the sample position. The Au coverage is given in monolayer equivalents (ML), which corresponds to a Au(111) packing density of $1.39 \cdot 10^{-15}$ Au

atoms per cm^2. The anatase crystal was mounted on a sample holder supported by 0.5 mm tungsten wires in thermal contact with a liquid nitrogen reservoir. The temperature was measured by a chromel-alumel thermocouple mounted close to the sample.

The sample was held at room temperature during Au evaporation, while CO adsorption and photoemission measurements were performed at a sample temperature of about 120 K. After each Au dose, 10 L (1 L = 10^{-6} torr·s) CO (Air Liquide, 99.97%) was introduced into the chamber through a leak valve to reach saturation. Before the next Au dose, CO was removed by flashing the sample to room temperature.

The photoemission spectra for the Au 4f core levels were recorded at normal emission with a photon energy of 220 eV. The overall experimental resolution for these spectra was about 0.2 eV. Binding energy calibration of the core level photoelectron spectra against the Fermi level was achieved by referencing to a Pt foil mounted on the sample holder. The spectra were fitted using a convolution of a Doniach-Sunjic line shape [20] and a Gaussian function, and by subtracting a linear background.

3. Results and discussion

Figure 2a shows the Au 4f spectra for increasing amounts of gold evaporated at room temperature on the anatase TiO_2(101) surface. For the two lowest coverages (0.007 ML and 0.03 ML Au) we observe one Au 4f contribution, with the $4f_{7/2}$ binding energy (BE) shifting from 84.9 eV to 84.7 eV. When going to the next Au dose (0.14 ML), the Au $4f_{7/2}$ BE has decreased to 84.1 eV. With increasing gold dose, the Au 4f peaks become sharper and there is a small shift to lower binding energy. For higher coverages the peak position stabilizes at 84.0 eV. The spectrum in the upper panel of figure 2a is for a thick Au film. Here it is possible to resolve the individual surface and bulk components. The BE for the bulk component is 84.0 eV while the BE of the surface component is 83.6 eV, giving a surface core level shift of 0.4 eV, in good agreement with that published for Au(111) [21]. The coverage dependent core level shift (0.9 eV) is significantly larger than that found previously for Au/rutile-TiO_2 and

Au/CeO_2 (0.3 eV) [22,23]. However, the major part of the shift, 0.6 eV, occurs when increasing the coverage from 0.03 ML to 0.14 ML.

Figure 2b shows the corresponding Au 4f spectra after CO saturation. In all cases, CO is found to induce a new state that appears at higher BE (green lines), while the intensity of the original peak becomes attenuated and the BE shifts towards higher values. The CO induced shift for 0.007 ML and 0.03 ML coverages is +1.5 eV, while the shift for 0.51 ML and larger coverages is +0.9 eV. Thus, a dramatic change in the electronic properties appears to occur between 0.03 ML and 0.14 ML coverage. This calls for a more detailed analysis of the spectra measured after these depositions.

The Au 4f spectrum measured at 0.14 ML coverage displays a clear asymmetry towards higher BE:s. We find that this spectrum can be delineated into two contributions, of which the component at the higher binding energy (dashed line) has the same position and intensity as for the peak at 0.03 ML coverage. After CO dosing, the spectrum at 0.14 ML coverage shows a pronounced asymmetry towards the high BE side, reaching up to the value found after CO exposure on the 0.03 ML situation. It is possible to describe this spectrum as a superposition of the CO dosed 0.03 ML situation (dashed lines) and a new situation with components located at lower BE. The CO induced shift of the lower binding energy peak is the same as for the higher Au coverages (+0.9 eV), while the shift is +1.5 eV for the higher binding energy peak.

Figure 3 shows the relative CO uptake, which is the ratio of the integrated CO-induced Au 4f contribution and the total integrated Au 4f intensity before CO adsorption, as a function of Au dose. The CO uptake is almost constant for the high BE Au contribution, while it decreases with the Au coverage for the low BE contribution.

The results suggest that the particles (denoted “particle type 1”) formed after 0.007 ML and 0.03 ML deposition are unique. Further deposition beyond 0.03 ML does not lead to any observable growth of these particles but rather to the nucleation of a new type of particles (“particle type 2”). The changeover from particle type 1 to particle type 2 is not continuous. At 0.14 ML coverage the two contributions (shifted 0.6 eV relative to each other) coexist and it is therefore appropriate to discuss the two particle types independently. The low coverage and limited growth of particle type 1 strongly suggest that their appearance is connected to the presence of point defects at

the surface. In contrast, particle type 2 shows the behavior typical for growth on an extended surface, i.e. continuous BE shift and a progressively decreasing CO uptake.

Figure 4 shows the binding energy of the Au $4f_{7/2}$ peak for gold that does not directly bond to CO, before and after CO adsorption, as a function of Au dose and separated into the two particle types. It is noted that the peak shifts to higher binding energy after CO adsorption. The most straightforward explanation is that this is an effect of having a negative core level shift of components from atoms with lower coordination number. This has been established by the observation of a negative surface core level shift for Au(111) [21]. That is, only the Au 4f states that are associated with under-coordinated Au atoms will shift towards higher BE upon CO adsorption. In the absence of resolved bulk and surface peaks, the result will be an apparent shift of the original peak and an appearance of a CO related peak.

The core level BE for particle type 2 shifts progressively towards lower values with increasing Au dose. Such shifts can in principle be caused by both initial and final state effects, including metal oxidation, charge transfer, reduced metal-metal coordination, screening and delocalization of the core hole [24]. A gradual shift with metal dose for metallic particles on poorly conducting supports has previously been reported by Howard et al. [22]. The shift was explained by assuming a model where the screening of the photoemission final state is less efficient for small particles compared to larger particles, indicating that the shift is due to increased particle size. Bäumer et al. have previously shown that metal particles of mean particle size d supported on alumina films exhibit a d^{-1} dependence of the BE shift [25]. The same group has also found that 3 nm Au particles already have the same binding energy as Au bulk (84.0 eV) [24]. Assuming a d^{-1} dependence, the single atom limit corresponds to a shift of about 1 eV. Consequently, if 3D aggregates are formed a shift by only a few tenths of an eV is expected to occur due to changes in particle size. In comparison, changing the oxidation state by one (a pure initial state effect) is expected to lead to a shift by about 1 eV.

The coverage dependent Au 4f core level shift for gold on a CeO_2 support is only about 0.3 eV to lower BE [23]. Accordingly, it was concluded that the shift is caused by the increasing particle size rather than a change in the Au oxidation state. We observe a similar behavior for Au particle type 2 on anatase TiO_2(101). Figure 4 shows that the BE shift found for particle type 2 is only 0.2 eV, from which follows that the shift can be attributed to a progressively increased particle size. That the

particle size increases is consistent with the decreasing CO uptake as seen in figure 3. CO is known to only adsorb on under-coordinated Au atoms [17,26]. The fraction of such atoms (which includes interface, corner and edge sites) decreases with increasing particle size, resulting in a reduced relative CO uptake [23], as discussed below.

The BE of the Au 4f peak for particles of type 1 is found to be shifted by +0.6 eV relative that of particle type 2. We assign this shift to initial state effects, most likely due to the formation of positively charged gold. The BE shift cannot be attributed to a size effect. A shift by +0.6 eV would correspond to a particle size close to a single atom [24], which is not compatible with the finding of partial adsorption of CO. If the particle size was close to one atom, adsorption of CO would be basically binary, i.e. none or all atoms would bond to CO.

Oxidized gold has recently been reported on various supports, including titania [14,27], magnesia [28], ceria [29,30] and iron oxide [31], and is considered to be important in achieving high activity of dispersed Au catalysts. Matthey et al. have shown that oxidized TiO_2 enhances the bonding strength of gold nanoparticles on rutile TiO_2(110) [14]. In that study, oxidized TiO_2 was formed by exposure to O_2, which heals oxygen vacancies and yields excess O atoms located in the troughs of this surface. The Au particles interact strongly with the O ad-atoms and calculations show an ionic bonding where Au becomes oxidized. In our case, the clean surface was prepared using O_2 treatment. It is feasible that this process leads to a small amount of O ad-atoms. We therefore propose that particle type 1, with the Au 4f component at higher binding energy, is due to oxidized gold particles, nucleating at the O ad-atoms on the TiO_2 terraces. Particle type 2 is identified as neutral gold aggregates, most likely located on the step edges, as seen with STM for the anatase TiO_2(101) surface by Gong et al. [17]. The behavior is consistent with the study of Au on rutile TiO_2(110) [14] since the oxidized Au particles are the first to form because of the strong interaction with O ad-atoms. Apparently, the oxidized particles only grow to a certain size after which nucleation at step edges begin.

Although oxidized gold is the minority species in the present work its presence is of interest with respect to the catalytic properties of the Au/TiO_2 system. Currently there is a lot of research interest in how defects in the form of oxygen vacancies and Ti interstitials on TiO_2 surfaces, influence the catalytic properties. We find that gold initially grows as oxidized particles, indicating that oxygen ad-atoms may be playing an important role. Under realistic conditions for catalyst applications, most oxygen

vacancies and Ti interstitials would be instantly healed by the high O_2 pressure. This could make oxygen ad-atoms one of the major sources of defects and strongly influence the catalytic behavior.

The particle size is a very important parameter. Gold has been suggested to be catalytically active only when the particles become smaller than 5 nm [2], with an optimum size for CO oxidation around 2 nm [8]. CO only adsorbs on under-coordinated Au atoms, and the fraction of such atoms on the surface of a particle is given by the size and shape of the particle. This means that the relative CO uptake in figure 3 can be related to the particle size, if we assume a specific particle shape. Figure 5 shows two modeled Au particles using the Wulff construction [32]. The particle sizes are 1 nm and 2 nm, respectively, and they look similar to real Au particles found by electron microscopy on a CeO_2 support [33]. From such models the number of under-coordinated surface atoms can be found, as done by Weststrate et al. [23]. For the 1 nm model particle, there are 15 under-coordinated surface atoms of totally 16 surface atoms (93%), while 39 of totally 57 (68 %) for the 2 nm particle.

Moreover, since CO adsorbs on the surface atoms and therefore reduces the intensity of the surface component, we need to know the ratio between the intensity of the surface component and the total Au 4f signal intensity. For our submonolayer coverages, it is not possible to separate the individual surface and bulk components, so this has to be estimated. For the thick Au film, the surface contribution to the overall Au 4f signal is found to be 0.46. For very small particles the ratio is expected to be close to one. Weststrate et al. has for Au on both CeO_2 and Ru(0001) found a ratio of 0.67 at an Au coverage of ~1.5 ML [23]. For our smaller model particles, shown in figure 5, this ratio can be estimated by knowing the mean free path, which we estimate to be 4.7 Å from the thick Au film. We find a ratio of 0.90 and 0.77 for the 1 nm and 2 nm model particles, respectively. For larger particles we assume a ratio of 0.67, in line with Weststrate et al.

By multiplying the fraction of under-coordinated surface atoms with the surface to total intensity ratio for a given particle size, we obtain the relative CO uptake for that particular size. The CO uptake values for our two model particles of size 1 nm and 2 nm are 0.84 and 0.52, respectively, as given in figure 5. By comparing the relative CO uptake values calculated for different particle sizes with the relative CO uptake curve for type 2 particles in figure 3, we can find the size of these Au particles. From this we estimate that the particles at ~0.4 ML Au coverage

are approximately 2 nm in size, while at ~1 ML Au coverage, they have a size of 3.5 nm.

The size of the oxidized particles (type 1) is not possible to estimate in the same way. The oxidized particles exhibit a constant relative CO uptake, which is much lower than for the initially formed type 2 particles. Using the same approach as for the type 2 particles, the CO uptake would suggest a size of 3-4 nm. However, such large particles are not feasible. First of all, the reducing conditions of this experiment make the formation of large 3D particles of oxidized gold very unlikely. Moreover, had the particles already after 0.03 ML reached a size of 3-4 nm it would be very difficult to explain a sudden stop in the growth such as that observed at 0.14 ML.

There can be several reasons for the very different behavior found for the oxidized particles with respect to CO adsorption. Both geometric and electronic effects are possible. The shape and location of the particle can make under-coordinated sites inaccessible to CO. It is also likely that electronic effects are important. The width of the Au 4f peak prior to CO adsorption is larger than the width of the Au 4f peaks related to gold bonded to CO. This suggests that there may be a distribution of Au 4f states with slightly different binding energies and hence a varying degree of oxidation. Such a scenario has been proposed based on calculations in the study of small Au particles interacting with O ad-atoms on the rutile TiO_2(110) surface [14]. From this an additional constraint on the adsorption of CO can be envisioned, namely that a certain electronic population of the Au atom is required, i.e. when sufficiently oxidized, gold atoms do not adsorb CO. Thus, the small particles containing oxidized gold can have a substantial part of under-coordinated sites but the CO uptake becomes reduced due to the electronic properties of the gold atoms.

4. Conclusions

In summary, we have utilized high resolution core level photoelectron spectroscopy to study submonolayer growth of gold and its interaction with CO on the anatase TiO_2(101) surface. We found that two different kinds of Au aggregates were formed. The first type is characterized by an Au $4f_{7/2}$ binding energy of 84.8±0.1 eV and a CO induced shift of 1.5 eV. This type of particle is only observed up to an Au coverage of 0.14 ML and appears to be size-limited. It also has a constant relative CO uptake. The

second particle type has an Au $4f_{7/2}$ binding energy of 84.1±0.1 eV and a CO induced shift of 0.9 eV. It is first observed at 0.14 ML and continues to grow at higher Au coverages, exhibiting a decreasing relative CO uptake with increasing Au dose, which is typical for an increasing particle size. We propose that the first particle type is oxidized gold. The low coverage suggests nucleation at defects, possibly oxygen ad-atoms located on the terraces. The second particle type is attributed to neutral gold, probably nucleating at steps. For the second particle type, we have used the CO uptake to estimate the particle size. Here we find an average particle size of 2 nm for the 0.4 ML Au coverage, while after an Au dose of 1 ML, the particles typically have a size of 3.5 nm.

Acknowledgements

This work was supported through the Swedish Science Council (VR), the Knut and Alice Wallenberg foundation (KAW), the Crafoord foundation and the Göran Gustafsson foundation. L.E.W. has been supported through the Strategic Area Materials at Norwegian University of Science and Technology. The assistance by the staff at MAX-lab is greatly acknowledged.

References

[1] B. Hammer and J. K. Nørskov, Nature **376**, 238 (1995).
[2] M. Haruta, Catal. Today **36**, 153 (1997).
[3] G. C. Bond, Catal. Today **72**, 5 (2002).
[4] M. Haruta, N. Yamada, T. Kobayashi, and S. Iijima, J. Catal. **115**, 301 (1989).
[5] A. Ueda and M. Haruta, Gold Bull. **32**, 3 (1999).
[6] D. Andreeva, V. Idakiev, T. Tabakova, A. Andreev, and R. Giovanoli, Appl. Catal. A: General **134**, 275 (1996).
[7] H. Huber, D. McIntosh, and G. A. Ozin, Inorg. Chem. **16**, 975 (1977).
[8] M. Valden, X. Lai, and D. W. Goodman, Science **281**, 1647 (1998).
[9] B. Schumacher, V. Plzak, M. Kinne, and R. J. Behm, Catal. Lett. **89**, 109 (2003).
[10] F. Boccuzzi and A. Chiorino, J. Phys. Chem. B **104**, 5414 (2000).
[11] M. Valden, S. Pak, X. Lai, and D. W. Goodman, Catal. Lett. **56**, 7 (1998).
[12] G. C. Bond and D. T. Thompson, Catal. Rev. Sci. Eng. **41**, 319 (1999).
[13] M. Mavrikakis, P. Stoltze, and J. K. Nørskov, Catal. Lett. **64**, 101 (2000).
[14] D. Matthey, J. G. Wang, S. Wendt, J. Matthiesen, R. Schaub, E. Laegsgaard, B. Hammer, and F. Besenbacher, Science **315**, 1692 (2007).
[15] Z.-P. Liu, X.-Q. Gong, J. Kohanoff, C. Sanchez, and P. Hu, Phys. Rev. Lett. **91**,

266102 (2003).
[16] C. J. Taylor, D. C. Gilmer, D. G. Colombo, G. D. Wilk, S. A. Campbell, J. Roberts, and W. L. Gladfelter, J. Am. Chem. Soc. **121**, 5220 (1999).
[17] X.-Q. Gong, A. Selloni, O. Dulub, P. Jacobson, and U. Diebold, J. Am. Chem. Soc. **130**, 370 (2008).
[18] R. Nyholm, J. N. Andersen, U. Johansson, B. N. Jensen, and I. Lindau, Nucl. Instrum. Methods Phys. Res., Sect. A **467-468**, 520 (2001).
[19] W. Hebenstreit, N. Ruzycki, G. S. Herman, Y. Gao, and U. Diebold, Phys. Rev. B **62**, R16334 (2000).
[20] S. Doniach and M. Sunjic, J. Phys. C: Solid State Phys. **3**, 285 (1970).
[21] P. Heimann, J. F. van der Veen, and D. E. Eastman, Solid State Commun. **38**, 595 (1981).
[22] A. Howard, D. N. S. Clark, C. E. J. Mitchell, R. G. Egdell, and V. R. Dhanak, Surf. Sci. **518**, 210 (2002).
[23] C. J. Weststrate, A. Resta, R. Westerström, E. Lundgren, A. Mikkelsen, and J. N. Andersen, J. Phys. Chem. C **112**, 6900 (2008).
[24] M. Baron, O. Bondarchuk, D. Stacchiola, S. Shaikhutdinov, and H.-J. Freund, J. Phys. Chem. C **113**, 6042 (2009).
[25] M. Bäumer and H.-J. Freund, Prog. Surf. Sci. **61**, 127 (1999).
[26] W.-L. Yim, T. Nowitzki, M. Necke, H. Schnars, P. Nickut, J. Biener, M. M. Biener, V. Zielasek, K. Al-Shamery, T. Kluner, and M. Baumer, J. Phys. Chem. C **111**, 445 (2007).
[27] L. Fu, N. Q. Wu, J. H. Yang, F. Qu, D. L. Johnson, M. C. Kung, H. H. Kung, and V. P. Dravid, J. Phys. Chem. C **109**, 3704 (2005).
[28] J. Guzman and B. C. Gates, J. Am. Chem. Soc. **126**, 2672 (2004).
[29] Q. Fu, H. Saltsburg, and M. Flytzani-Stephanopoulos, Science **301**, 935 (2003).
[30] J. Guzman, S. Carrettin, and A. Corma, J. Am. Chem. Soc. **127**, 3286 (2005).
[31] G. J. Hutchings, M. S. Hall, A. F. Carley, P. Landon, B. E. Solsona, C. J. Kiely, A. Herzing, M. Makkee, J. A. Moulijn, A. Overweg, J. C. Fierro-Gonzalez, J. Guzman, and B. C. Gates, J. Catal. **242**, 71 (2006).
[32] G. Z. Wulff, Krystallogr. Mineral. **34**, 449 (1901).
[33] T. Akita, M. Okumura, K. Tanaka, M. Kohyama, and M. Haruta, J. Mater. Sci. **40**, 3101 (2005).

Figure captions

FIG. 1. Low-energy electron diffraction (LEED) pattern of the pristine anatase TiO_2(101) surface, which is bulk terminated and shows a (1x1) LEED pattern. The electron kinetic energy is 142 eV.

FIG. 2. Au 4f spectra for the anatase TiO_2(101) surface recorded after different Au exposures, (a) before and (b) after saturation with 10 L CO at 120 K sample temperature. The contributions indicated by green lines are due to Au atoms directly bonded to CO. The peaks indicated by dotted lines for the 0.14 ML coverage have the same positions and intensities as the peaks in the 0.03 ML case. The spectrum at the top of the figure is for a thick Au film, where the individual bulk and surface components are clearly visible.

FIG. 3. Relative CO uptake, which is the ratio of the integrated CO-induced intensity and the total integrated intensity before CO adsorption of the Au $4f_{7/2}$ peaks, for the two particle types as a function of Au dose.

FIG. 4. Binding energy of the Au $4f_{7/2}$ peak for gold that does not directly bond to CO, before and after CO adsorption, as a function of Au dose for the two particle types.

FIG. 5. Model gold particles using the Wulff construction, with the calculated relative CO uptake.

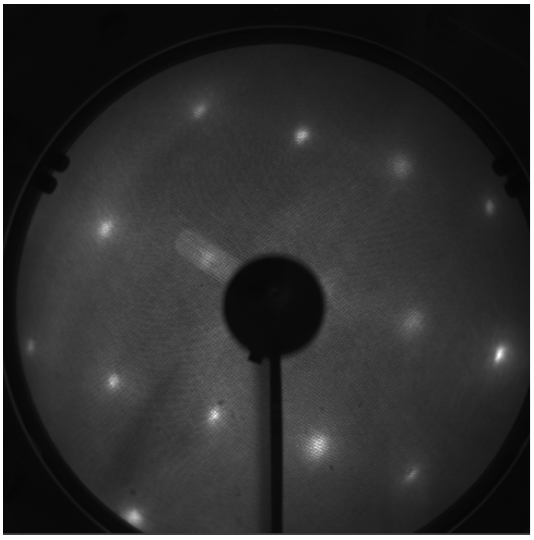

Figure 1

L. E. Walle et al.

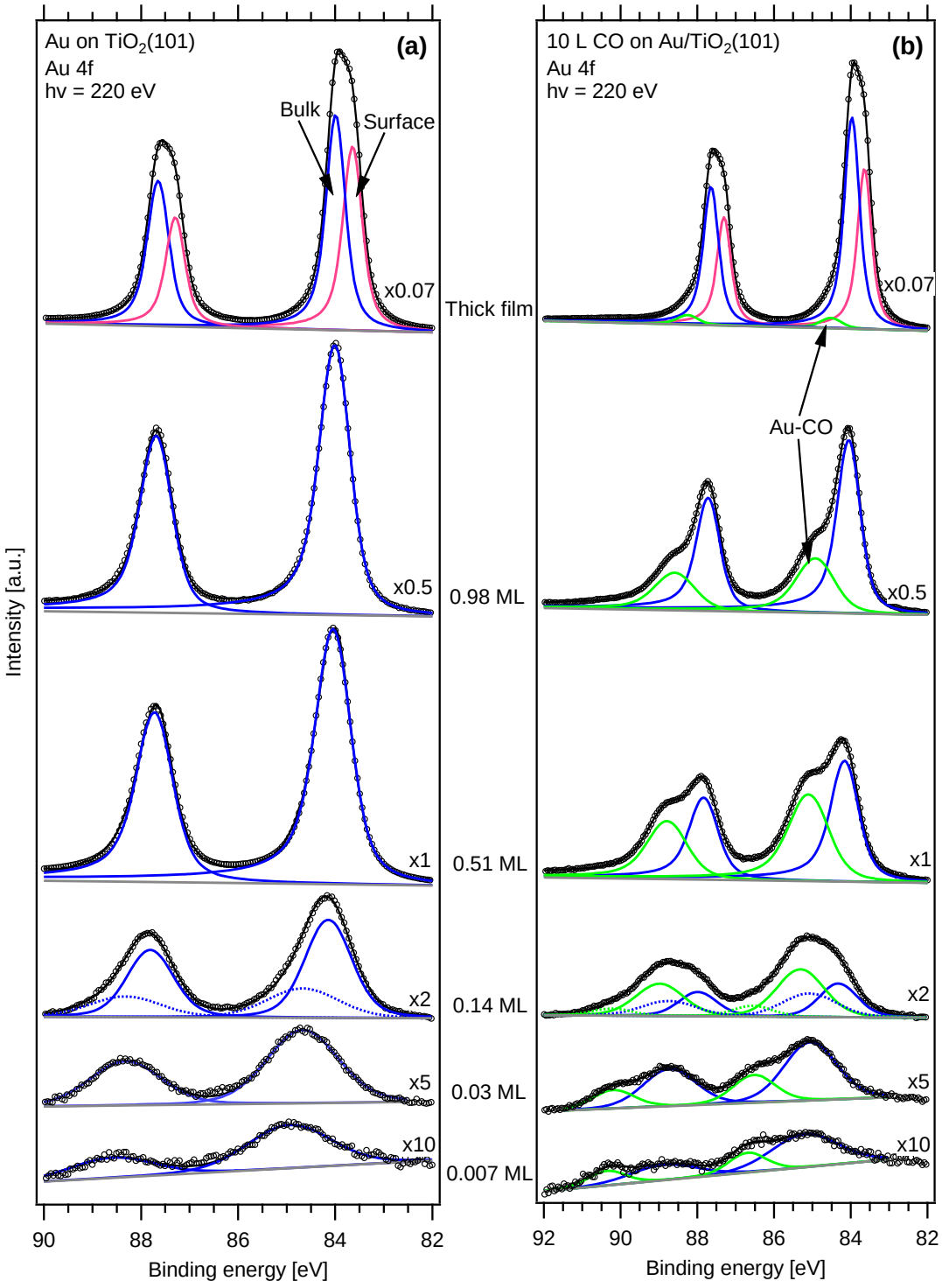

Figure 2

L. E. Walle et al.

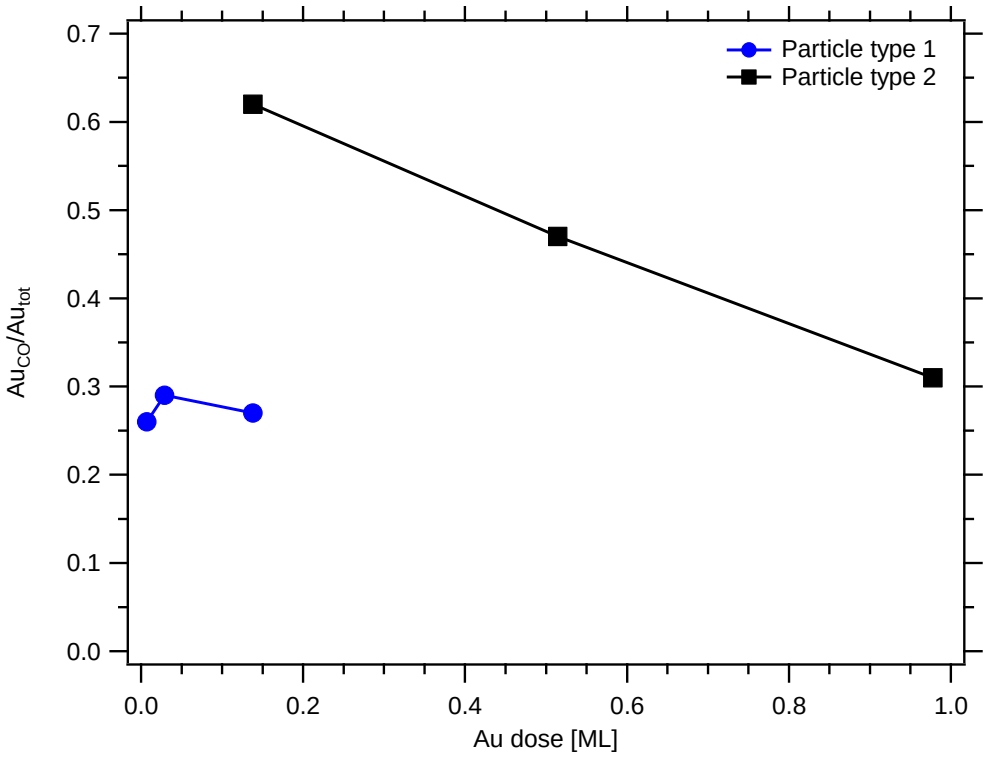

Figure 3

L. E. Walle et al.

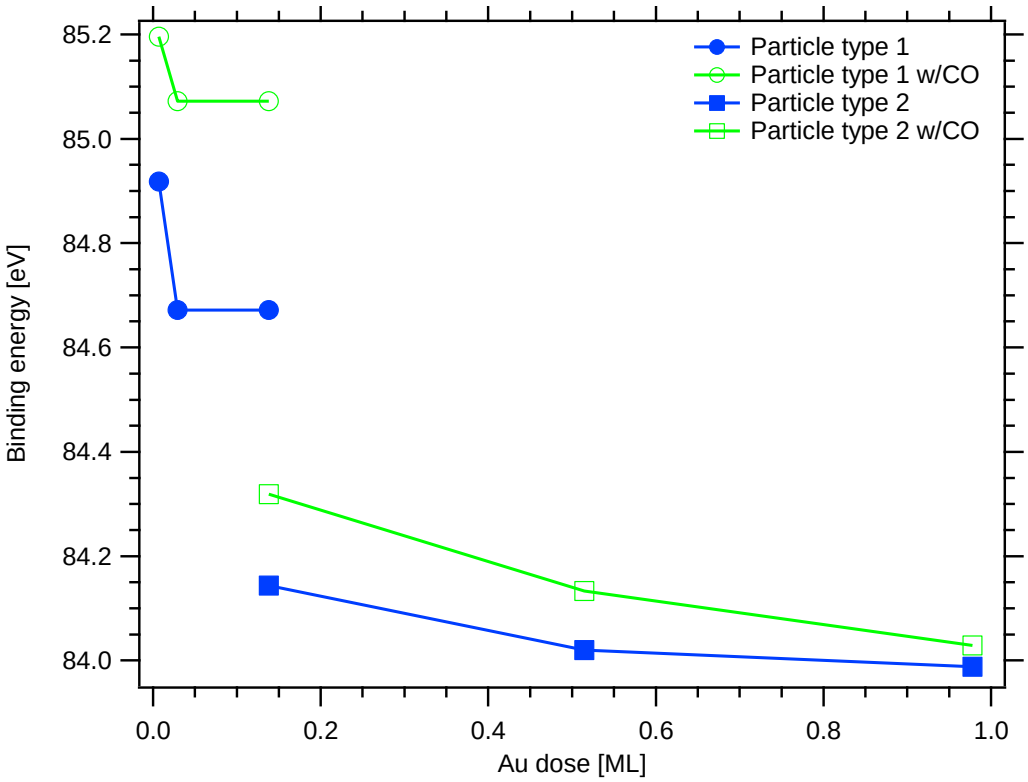

Figure 4

L. E. Walle et al.

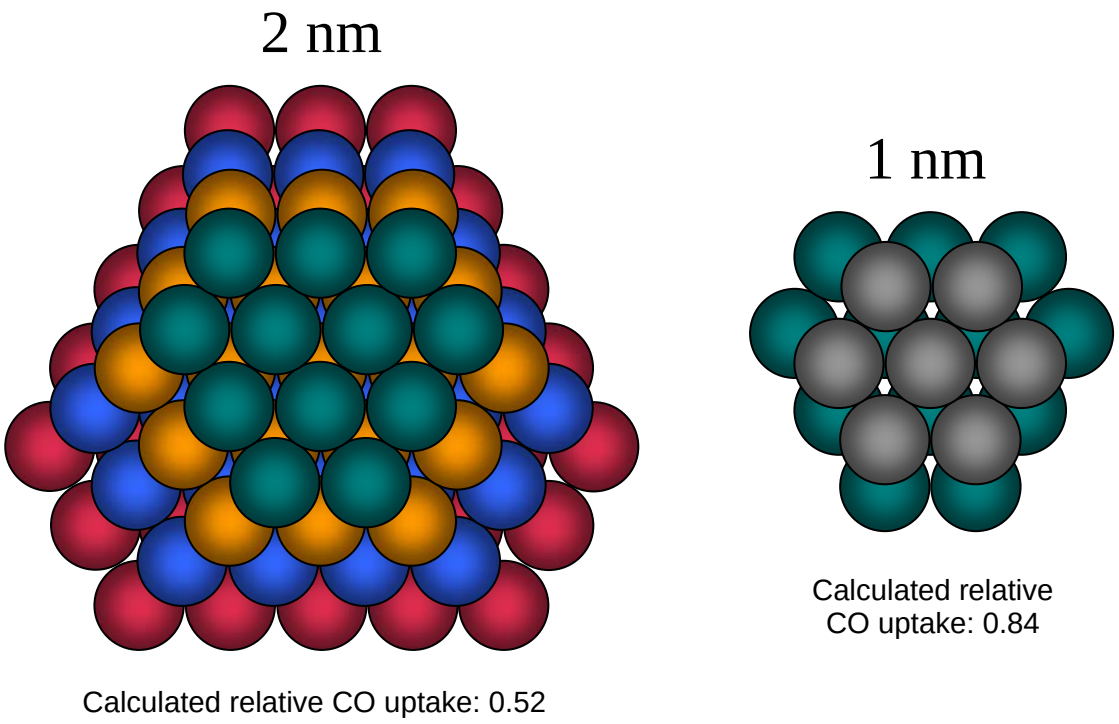

Figure 5

L. E. Walle et al.

Paper VI

Growth of ultrathin TiO_x films on Pt(110) studied by high resolution photoemission and X-ray absorption spectroscopy.

L. E. Walle, I.-H. Svenum, A. Borg and A. Sandell

In manuscript.

Growth of ultrathin TiO_x films on Pt(110) studied by high resolution photoemission and X-ray absorption spectroscopy

L. E. Walle[1], I.-H. Svenum[1], A. Borg[1] and A. Sandell[2,*]

[1] *Dept. of Physics, Norwegian University of Science and Technology, NO-7491 Trondheim, Norway*

[2] *Dept. of Physics and Materials Science, Uppsala University, P. O. Box 530, SE-751 21 Uppsala, Sweden*

Using high resolution photoemission and X-ray absorption spectroscopy the growth of an ultrathin TiO_x film on the Pt(110)-(1x2) surface has been studied. From Ti 2p XAS spectra of the deposited TiO_x film a structural change from a rutile-like structure when TiO_x coexists with PtO_2 to an anatase-like structure upon completion of a TiO_x bilayer on the Pt surface is observed. Upon comparison to an anatase TiO_2(001) single crystal, the complete TiO_x bilayer displays a very similar band alignment with respect to the Fermi level but with a band gap that is 0.2 eV lower. In contrast, a rigid shift of –0.8 eV is found for the electronic states of the bilayer islands. This shift is explained in terms of a band bending effect imposed by the PtO_2 patches.

*Corresponding author. Email: anders.sandell@fysik.uu.se; Fax: +46 18 4713524

1. Introduction

Titanium dioxide is a material that has been thoroughly studied in the last couple of decades because of its importance in technical areas, including catalysis and photocatalysis [1-3], sensors [4,5], biomedical [6-8] implants and various energy applications [9,10]. Recently nanostructured titania started to attract a lot of research interest because of the remarkable properties found for new and exotic phases like nanosheets, nanotubes, nanorods and nanoclusters [11,12]. Several of these new phases do not have a bulk counterpart and their properties are closely related to the surface structure and to interface effects, making a surface science approach highly relevant.

Titania nanosheets are thought to be the building blocks of titania nanotubes and nanorods calling for careful investigations of their physical and structural properties. It was recently reported that a TiO_x double layer can be assembled on Pt(110) and Pt(111) surfaces with a geometric structure similar to that found for unsupported TiO_2 nanosheets [13,14]. Studying such ultrathin films on a single crystal metal support can serve both as a nanosheet model as well as a new material in its own right, which properties are determined by the combination of the oxide film properties and those of the support.

Agnoli et al. [15] have demonstrated that it is possible to prepare a fully oxidized TiO_2 ultrathin film by deposition of Ti in an O_2 background pressure on the Pt(110)–(1x2) reconstructed surface. They find that the oxide overlayer is a stoichiometric lepidocrocite-like single domain nanosheet, which can be thought of as originating from an anatase bilayer spontaneously reconstructing by an uniaxial relative sliding of one single layer with respect to the other by half a unit cell. From STM they find that the film grows in a bilayer mode even for submonolayer coverages where only a fraction of the Pt surface is covered. LEED shows a (11x2) pattern during the initial film growth, due to oxygen chemisorption on the Pt(110)-(1x2) surface [16]. For higher coverages, this pattern disappears and a 14x splitting develops. When reaching a complete bilayer, a (14x4) supercell becomes evident.

In the present work we have utilized synchrotron based photoemission and X-ray absorption spectroscopy to study the formation of an ultrathin TiO_x film on the

Pt(110)-(1x2) reconstructed surface complementing the reported detailed structural analysis performed by STM and LEED by Agnoli et al [15]. Using X-ray absorption spectroscopy (XAS) we are able to add to this picture an observed structural difference between the sub-layer and the full double layer where the sub-layer has a rutile-like structure, while the bilayer appears more anatase-like. Photoelectron spectroscopy (PES) in combination with XAS reveal a band bending of about 0.8 eV for the TiO_x bilayer islands that vanishes upon completion of the bilayer. The band gap of the bilayer is furthermore found to be about 0.2 eV lower than that of bulk anatase.

2. Experimental

High-resolution synchrotron radiation PES and XAS measurements were performed at beamline I311 of the MAX II storage ring at the Swedish National Synchrotron Laboratory, MAX-lab, in Lund, Sweden. The beam line is equipped with a modified Zeiss SX-700 monochromator and a 200 mm radius hemispherical electron energy analyzer of Scienta type [17]. The base pressure of the UHV chamber was about $1 \cdot 10^{-10}$ mbar.

The Pt(110) single crystal (supplied by Surface Preparation Laboratory) was cleaned by cycles of argon sputtering and annealing at 980 K, followed by cooling in oxygen ($p = 5 \cdot 10^{-7}$ mbar) down to 700 K. Finally the sample was flashed to 980 K to remove any adsorbed oxygen. The procedure gave a clean and well-defined surface, as judged from photoemission measurements of the C 1s, O 1s and Pt 4f core level regions, and observed low energy electron diffraction (LEED) patterns.

Titanium was evaporated by sending direct current through a 0.5 mm Ti wire filament. The evaporation was performed in an oxygen atmosphere ($p = 1 \cdot 10^{-6}$ mbar), followed by a post annealing treatment in oxygen at 700 K to improve long-range order of the titania layer and to have a complete oxidation of Ti. The Pt crystal was supported by 0.5 mm tungsten wires, and the temperature was measured by a chromel-alumel thermocouple spot welded to the back side of the crystal.

The sample was kept at room temperature both during Ti evaporation and measurements. The photoemission spectra were recorded at normal emission with a

photon energy of 610 eV for the Ti 2p, 625 eV for the O 1s and 125 eV for the Pt 4f core levels, and 130 eV for the valence band region. For all spectra, a scan of the Fermi level region was recorded immediately after measuring the core level region and used as binding energy reference. The X-ray absorption spectra were calibrated by recording the Fermi level region with first- and second-order light from the monochromator.

3. Results and discussion

In the following, we will focus on three Ti depositions. As discussed below, deposition 3 is assigned to a full bilayer. At this point a 14x LEED pattern was observed. We were never able to observe the x4 periodicity. Increasing the coverage inevitably leads to a complete loss of surface order according to LEED. Assuming growth of bilayer islands that eventually form a full bilayer, the intensities of the Ti 2p photoemission peaks for deposition 1 and 2 correspond to a surface covered by 20% and 70% of TiO_x, respectively.

Figure 1 shows Ti 2p XAS spectra for different TiO_x coverages. Included for comparison are also results for anatase TiO_2(001) and rutile TiO_2(110) single crystals. The Ti 2p XAS spectrum is sensitive to the local geometry of the Ti atoms and can be used to fingerprint different TiO_2 polymorphs [18]. This is demonstrated in Fig. 1 where the relative intensities of the peaks making up the doublet feature centered at 460 eV becomes reversed when changing from anatase to rutile. The doublet structure is commonly assigned to e_g states. The difference in the relative intensities between rutile and anatase is attributed to a change in the octahedral distortion of the lattice. A change in the e_g structure is also observed in the case of TiO_x formation on Pt(110). When separate TiO_x islands are present (1st and 2nd deposition), the e_g structure has a rutile-like shape. However, once the extended TiO_x layer is formed (3rd deposition) it changes into a more anatase-like appearance. The anatase-like structure is in accordance with the previous results on the full double layer [15]. After the 4th deposition, the peaks broaden as an effect of the loss of order.

The Pt $4f_{7/2}$ spectra for deposition 1 to 3 are compared in Fig. 2. Deposition 1 and 2 are characterized by a high binding energy (BE) shoulder, located at 71.5 eV, relative to the Pt $4f_{7/2}$ bulk contribution. This shoulder appears as a result of formation

of PtO_2 stripes on the Pt(110)-(1x2) reconstructed surface, a reconstruction remaining upon oxygen adsorption [19]. This stripe formation has been investigated by STM [16], revealing formation of a nanopattern with a (11x2) superstructure at high oxygen coverage. STM results for TiO_x/Pt(110) show similar stripes on the areas not covered by TiO_x islands [15]. The magnitude of the Pt 4f shift depends on the O coverage and the sites occupied by the O atoms. In a previous high resolution PES study of O adsorbed on the stepped Pt(332) surface, one-dimensional (1D) PtO_2 was found to form at the step edges [20]. The Pt 4f spectrum displayed a shoulder similar to that in Fig. 2. Based on the Pt 4f spectrum we can therefore conclude that PtO_2 most probably forms after the first deposition. Increasing the TiO_x coverage leads to a decrease in the amount of PtO_2 with very little left after the 3rd deposition. Our photoemission data thus support PtO_2 coexisting with TiO_x islands. The disappearance of the PtO_2 contribution in the Pt 4f spectra after the 3rd deposition coincides with the appearance of an anatase-like structure in the Ti 2p XAS spectra and is taken as evidence for formation of a complete TiO_x bilayer at this point. When the coverage is sufficient to form a full double layer, PtO_2 vanishes and the geometric structure of the TiO_x film changes. Thus, PtO_2 appears to influence the geometric structure of the TiO_x film and in the following we will also show that it has a significant influence on the electronic structure.

Figure 3 shows O 1s (a) and Ti $2p_{3/2}$ (b) photoemission spectra for deposition 1 to 3. Valence spectra measured after deposition 2 and 3 are found in Figure 4. It stands clear that essentially all the TiO_x related PES structures undergo a substantial positive BE shift between the 2nd and 3rd deposition. The shifts are very similar: The O 1s peak shifts by +0.83 eV, the Ti $2p_{3/2}$ intensity maximum shifts by +0.83 eV and the valence band maximum shifts by approximately +0.85 eV. This strongly suggests a rigid shift of the TiO_x electronic levels.

The Ti $2p_{3/2}$ spectra show however a rather complex behavior with increasing TiO_x coverage. More than one state are present in all the spectra and while the shift of the maximum is in accordance with the rigid band model, the low BE onset appears unchanged. We therefore expect to have states that shift by about +0.8 eV and (at least) one state that shifts very little with coverage. The spectra have therefore been delineated based on this assumption. The width and position of species 3 in the spectrum after deposition 2 were estimated by subtracting the spectrum after deposition 1 from the spectrum measured after deposition 2. The spectrum after the

3rd deposition was fitted with components and the constraint that the width of peak 2 should not exceed the width of peak 2 after deposition 2. Moreover, provided that peak 2 shifts by about 0.8 eV between deposition 2 and 3, it becomes very difficult to discriminate this component from component 1. We have therefore chosen to indicate the assumed BE of species 1 with a dashed line for the 1st and 2nd depositions. Regarding peak 4, it is not clear whether this is a chemically shifted state or the result of having asymmetric line shapes due to the presence of the Pt substrate.

In an initial state picture, the low BE of species 1 suggests that it is associated with reduced Ti, that is, Ti of an oxidation state below +4. The low BE may also be the result of efficient final state screening due to the proximity of the Pt substrate (c.f. below). In either case, it is most likely that species 1 is related to direct Ti-Pt bonds and hence associated with an O_xTi-Pt configuration. For reasons that will be discussed in more detail in the next section, the other Ti 2p species are assigned to TiO_x not in direct contact with metallic Pt. Since the relative intensity of the low BE Ti $2p_{3/2}$ states increases with decreasing coverage, it is feasible that formation of Ti-Pt bonds are important for the island nucleation.

Variations in the relative amount of species 1 should in principle modify the Ti 2p XAS spectrum accordingly. However, the change in the Ti 2p XAS spectral shape when going from deposition 1 to deposition 2 is very small. The fine structure of the Ti 2p XAS spectrum is thus largely determined by the properties of species 2-4. That is, the relative intensities of the e_g states is a signature of the incomplete and complete TiO_x bilayer itself.

Except for the Ti 2p contribution due to species 1 all the TiO_x related PES structures undergo a rigid positive BE shift between the 2nd and 3rd deposition. We will demonstrate that this shift can be understood in terms of a band bending effect. The argumentation that follows is schematically illustrated in Fig. 5. We reiterate that this step in the growth is associated with (1) the completion of the TiO_x bilayer, (2) the disappearance of PtO_2 and (3) a geometric change in the TiO_x local structure. Clearly, in the case of a semiconducting oxide in contact with a metal both initial and final state effects can influence the photoemission results. With respect to initial state effects, band bending typically appears when a metal is brought into contact with a semiconductor since the Fermi levels have to match. The driving force for the band bending is then the difference between the work function (WF) of the metal and the electron affinity (EA) of the semiconductor. Charge will flow between the metal and

the semiconductor leading to a shift in the Fermi level location of the semiconductor. TiO_2 is often found to be an n-type semiconductor in that the Fermi level is located close to the conduction band minimum [21]. When in contact with a metal with higher WF than the EA of TiO_2, charge will flow from the TiO_2 to the metal. As a result the Fermi level of TiO_2 at the interface will be shifted towards the valence band maximum and the valence and conduction band edges exhibit a bending downwards in binding energy.

We have previously presented an approach with which the location of the valence and conduction band edges can be monitored [21,22]. The valence band is represented by the Fermi level referenced PES spectrum. The conduction band is represented by the O 1s XAS spectrum, referenced to the Fermi level by using the O 1s PES binding energy. Changes in the position of the leading peak in the O 1s XAS spectrum is expected to reflect changes in the location of the conduction band edge [22]. However, the position of the leading peak relative the Fermi level may be offset with respect to the conduction band onset in the case of TiO_2 [21].

The band alignment obtained for the second and third TiO_x depositions on Pt(110) are shown in Fig. 4. The results for a clean anatase TiO_2(001) bulk sample is shown at the top for comparison. For the full TiO_x double layer, attained after the 3rd deposition, the band alignment relative to the Fermi level is very similar to that found for bulk anatase TiO_2(001). The leading peak of the unoccupied states is in both cases found 0.79 eV above the Fermi level whereas the valence band maximum is found at 3.49 eV for the bulk sample and at 3.31 eV for the TiO_x layer on Pt(110). This indicates a smaller band gap for the TiO_x film. Importantly, the similar alignment of the TiO_x layer and the bulk sample indicates that the band bending is small, i.e. the difference between the TiO_x EA and the substrate WF is small [23].The WF values for Pt(110) in the literature varies between 5.1 and 5.9 eV [24,25]. A WF value of 5.1 eV for single crystalline anatase (001) has been reported [26]. Consequently, although not straightforward to verify, the similar band alignments of the TiO_x film and bulk anatase are not unlikely.

The situation is different for the sub-layer coverages where PtO_2 is present. The PtO_2/Pt(110) system has a higher WF than the clean Pt(110) surface due to the presence of adsorbed oxygen atoms [27,28]. Hence a shift of the TiO_x derived levels due to band bending is observed for the sub-layer situations (depositions 1 and 2). The valence band maximum and the leading XAS peak shift by –0.85 eV and –0.79 eV,

respectively, relative to the Fermi level. The direction and magnitude are both consistent with the increased the WF for PtO_2/Pt relative to that of Pt(110). Previous studies report WF changes of 0.3 eV [28] up to about 1 eV [27]. The lower value was found after O adsorption at 300 K whereas the higher value was found after O adsorption at 560 K. Since our preparation procedure includes post-oxidation at 700 K it is most likely that a value similar to the higher one applies here.

The behavior in Fig. 4 shows that the BE shift for the Ti species 2-4 found in the Ti 2p spectra is primarily the result of band bending and not a change in the chemical state of Ti. The Ti $2p_{3/2}$ BE of species 3 after deposition 3 is 458.55 eV, which is smaller than the BE found for bulk anatase, at 458.90 eV. The difference is partly accounted for by the 0.2 eV wider band gap of the bulk sample. Thus, the oxidation state of species 3 is +4. The chemical state of species 2 is more nebulous. The peak undergoes a shift due to band bending, which indicates that it is electronically a part of the oxide and not hybridized with the Pt. A plausible explanation is that this state is associated with Ti in the first layer. The Ti atoms within the first layer will be image screened more efficiently by the Pt substrate upon ionization than the Ti atoms in the second layer. Thus, the split observed between state 2 and 3 might therefore be the result of a layer dependent BE.

Species 1 in the Ti 2p core level PES spectrum is not subjected to the shift due to band bending observed for the other TiO_x related PES contributions. This behavior can be understood from the fact that we attribute species 1 to be associated with Ti atoms having electronic states hybridized with Pt states. This conjecture is further supported by the energy relationship of the Ti 2p photoemission spectrum and the Ti 2p X-ray absorption spectrum. Figure 6 shows the results obtained after the 3rd deposition. It is found that the binding energy of the Ti 2p photoemission peak is located close to the photon energy onset of the Ti 2p XAS spectrum. The XAS onset represents the neutral core excited state of lowest energy. If the PES BE is connected to the XAS onset it thus implies that the PES final state is fully screened by charge transfer. Charge transfer screening occurs by virtue of the Ti-Pt hybridization.

According to the atomic structure model presented by Agnoli et al. [15], mixing of Ti and Pt electronic states may occur at certain anticoincidence regions. However, only one Ti atom out of 14 within the first layer is located at an anticoincidence site. This is not compatible with the relative intensity of species 1 found in Figure 3 (b) after deposition 3, which is considerably higher. One possible

explanation is that more than one Ti atom is electronically affected by the anticoincidence site. Another possibility is that our preparation procedure needs to be refined. We did not observe any clear evidence for the x4 periodicity and since the Ti-Pt hybridization is probably connected to the nucleation of TiO_x islands, the exact preparation procedure is likely to be critical. How the high-resolution Ti 2p spectrum depends on the preparation is therefore something that has to be investigated further.

4. Conclusions

In summary, from Ti 2p XAS spectra of a TiO_x film deposited on the Pt(110)-(1x2) surface a structural change from a rutile-like structure when TiO_x coexists with PtO_2 to an anatase-like structure upon completion of a TiO_x bilayer on the Pt surface is observed. A band bending of about 0.8 eV is seen for the TiO_x bilayer islands, an effect that disappears upon completion of the bilayer. The band bending is induced by the PtO_2 structures that are present when the surface is not fully covered by TiO_x. The full TiO_x bilayer displays a band gap 0.2 eV lower than that observed for bulk anatase.

Acknowledgements

This work was supported through the Swedish Science Council (VR), the Knut and Alice Wallenberg foundation (KAW), the Crafoord foundation, NordForsk and the Göran Gustafsson foundation. L.E.W. has been supported through the Strategic Area Materials at Norwegian University of Science and Technology, and I.-H.S. through the Research Council of Norway (Project number 148869/V30). The assistance by the staff at MAX-lab is greatly acknowledged.

References

[1] K. Hashimoto and H. Fujishima, Jpn. J. Appl. Phys. **44**, 8269 (2005).
[2] J. A. Rodriguez, T. Jirsak, G. Liu, J. Hrbek, J. Dvorak, and A. Maiti, J. Am. Chem. Soc. **123**, 9597 (2001).
[3] M. R. Hoffmann, S. T. Martin, W. Y. Choi, and D. W. Bahnemann, Chem. Rev.

95, 69 (1995).
[4] A. S. Zuruzi, A. Kolmakov, N. C. MacDonald, and M. Moskovits, Appl. Phys. Lett. **88**, 102904 (2006).
[5] Y. Zhu, J. Shi, Z. Zhang, C. Zhang, and X. Zhang, Anal. Chem. **74**, 120 (2002).
[6] M. M. Klinger, F. Rahemtulla, C. W. Prince, L. C. Lucas, and J. E. Lemons, Oral. Biol. Med. **9**, 449 (1998).
[7] D. E. MacDonald, N. Deo, B. Markovic, M. Stranick, and P. Somasundaran, Biomaterials **23**, 1269 (2002).
[8] P. Cacciafesta, A. D. L. Humphris, K. D. Jandt, and M. J. Miles, Langmuir **16**, 8167 (2000).
[9] B. O'Regan and M. Grätzel, Nature **353**, 737 (1991).
[10] F. Croce, G. B. Appetecchi, L. Persi, and B. Scrosati, Nature **394**, 456 (1998).
[11] X. Chen and S. S. Mao, Chem. Rev. **107**, 2891 (2007).
[12] D. V. Bavykin, J. M. Friedrich, and F. C. Walsh, Adv. Mater. **18**, 2807 (2006).
[13] Y. Zhang, L. Giordano, G. Pacchioni, A. Vittadini, F. Sedona, P. Finetti, and G. Granozzi, Surf. Sci. **601**, 3488 (2007).
[14] T. Orzali, M. Casarin, G. Granozzi, M. Sambi, and A. Vittadini, Phys. Rev. Lett. **97**, 156101 (2006).
[15] S. Agnoli, T. Orzali, M. Sambi, A. Vittadini, M. Casarin, and G. Granozzi, J. Phys. Chem. C **112**, 20038 (2008).
[16] S. Helveg, W. X. Li, N. C. Bartelt, S. Horch, E. Laegsgaard, B. Hammer, and F. Besenbacher, Phys. Rev. Lett. **98**, 115501 (2007).
[17] R. Nyholm, J. N. Andersen, U. Johansson, B. N. Jensen, and I. Lindau, Nucl. Instrum. Methods Phys. Res., Sect. A **467-468**, 520 (2001).
[18] R. Ruus, A. Kikas, A. Saar, A. Ausmees, E. Nõmmiste, J. Aarik, A. Aidla, T. Uustare, and I. Martinson, Solid State Commun. **104**, 199 (1997).
[19] W. X. Li, L. Österlund, E. K. Vestergaard, R. T. Vang, J. Matthiesen, T. M. Pedersen, E. Lægsgaard, B. Hammer, and F. Besenbacher, Phys. Rev. Lett. **93**, 146104 (2004).
[20] J. G. Wang, W. X. Li, M. Borg, J. Gustafson, A. Mikkelsen, T. M. Pedersen, E. Lundgren, J. Weissenrieder, J. Klikovits, M. Schmid, B. Hammer, and J. N. Andersen, Phys. Rev. Lett. **95**, 256102 (2005).
[21] A. Sandell, B. Sanyal, L. E. Walle, J. H. Richter, S. Plogmaker, P. G. Karlsson, A. Borg, and P. Uvdal, Phys. Rev. B **78**, 075113 (2008).
[22] A. Sandell, P. G. Karlsson, J. H. Richter, J. Blomquist, P. Uvdal, and T. M. Grehk, Appl. Phys. Lett. **88**, 132905 (2006).
[23] This conclusion is valid under the assumption of similar EA of the TiO_x film and the bulk anatase sample.
[24] R. Könenkamp, Phys. Rev. B **61**, 11057 (2000).
[25] *CRC Handbook of Chemistry and Physics: A Ready-Reference Book of Chemical and Physical Data* (CRC Press, 2008).
[26] G. Xiong, R. Shao, T. C. Droubay, A. G. Joly, K. M. Beck, S. A. Chambers, and W. P. Hess, Adv. Funct. Mater. **17**, 2133 (2007).
[27] C. S. Shern, Chin. J. Phys. **30**, 841 (1992).
[28] N. Freyer, M. Kiskinova, G. Pirug, and H. P. Bonzel, Surf. Sci. **166**, 206 (1986).

Figure captions

FIG. 1. Ti 2p X-ray absorption spectra for four different TiO_x coverages on the (1x2) reconstructed Pt(110) surface, as well as for anatase TiO_2(001) and rutile TiO_2(110) single crystals.

FIG. 2. Pt $4f_{7/2}$ spectra measured after deposition 1 to 3. The three curves have been normalized to the same peak height to facilitate the comparison.

FIG. 3. O 1s (a) and Ti $2p_{3/2}$ (b) spectra measured after deposition 1 to 3. The Ti $2p_{3/2}$ spectra have been decomposed into four individual components. Assuming growth of bilayer islands that form a full bilayer after deposition 3, the intensities of the Ti 2p photoemission peaks for deposition 1 and 2 correspond to a surface covered by 20% and 70% of TiO_x, respectively.

FIG. 4. Valence band photoemission spectra and O 1s X-ray absorption spectra on the same energy scale for the second and third TiO_x depositions on Pt(110), as well as for a clean anatase TiO_2(001) bulk sample.

FIG. 5. Schematical illustration of the band bending effect. The figure shows the position of the Fermi level (E_F) relative to the valence band (VB) and the conduction band (CB) for (a) bulk anatase TiO_2, (b) a full TiO_x double layer on Pt(110) and (c) a sub-layer of TiO_x on Pt(110).

FIG. 6. Ti 2p photoemission and X-ray absorption spectra measured after deposition 3, on a common energy scale. The binding energy of species 1 in the Ti 2p PES spectrum is located close to the photon energy onset of the Ti 2p XAS spectrum.

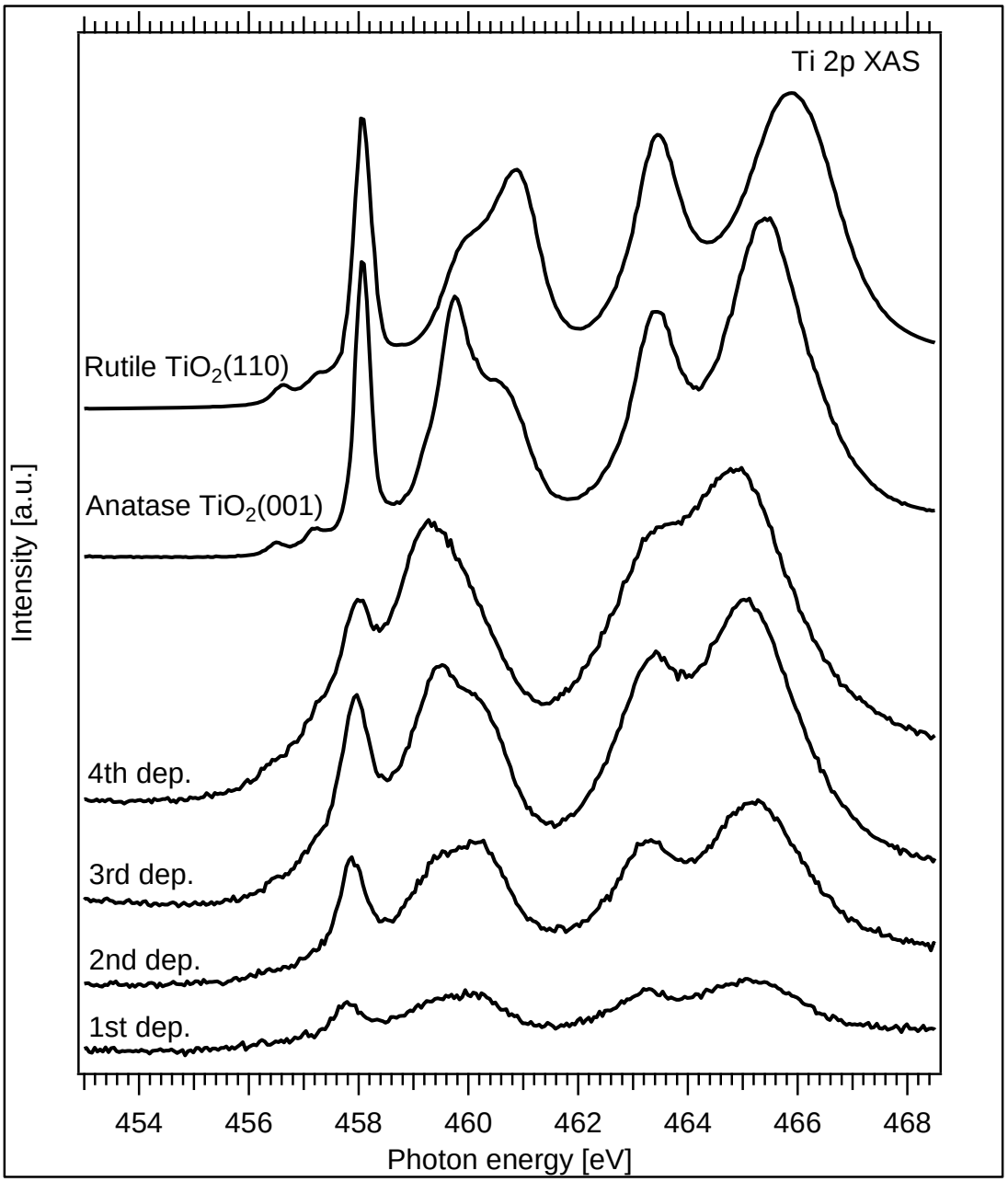

Figure 1

L. E. Walle et al.

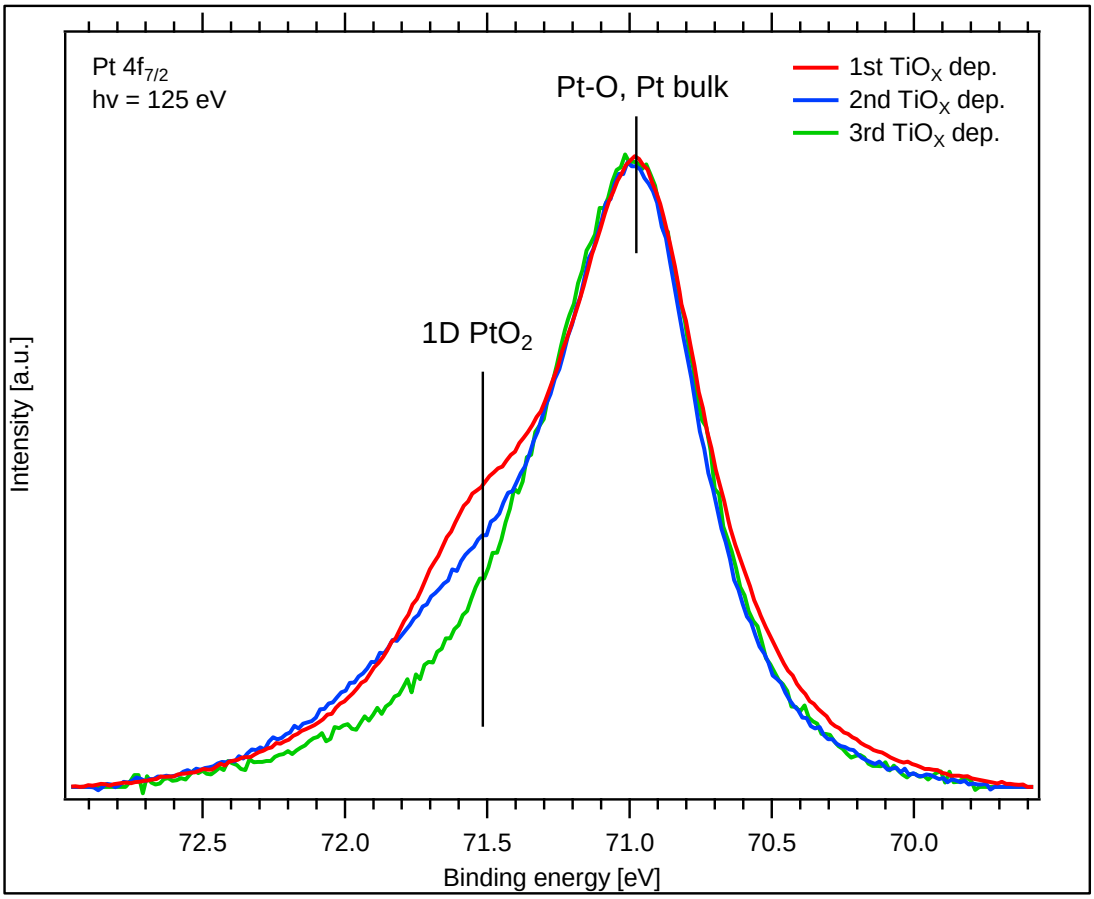

Figure 2

L. E. Walle et al.

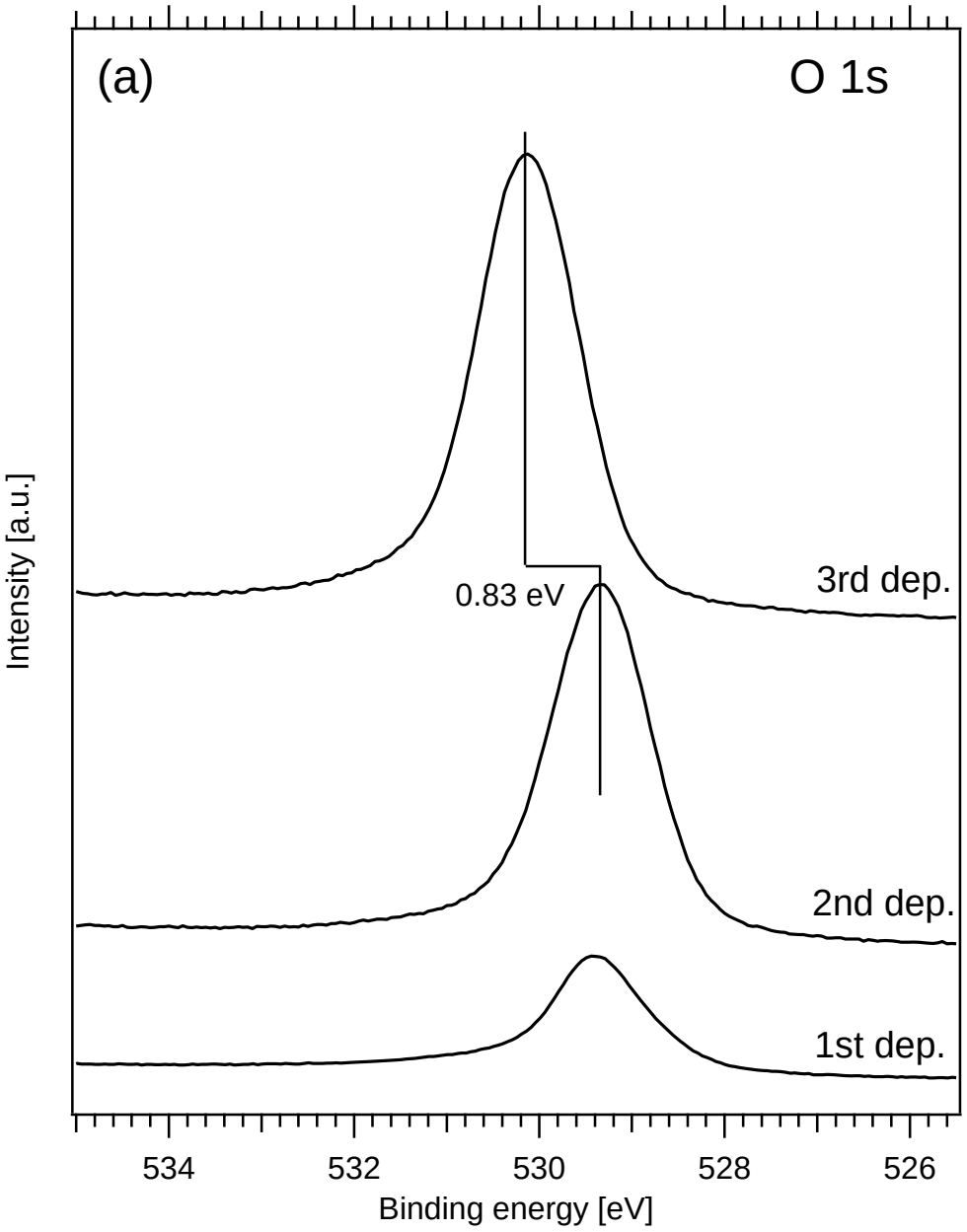

Figure 3a

L. E. Walle et al.

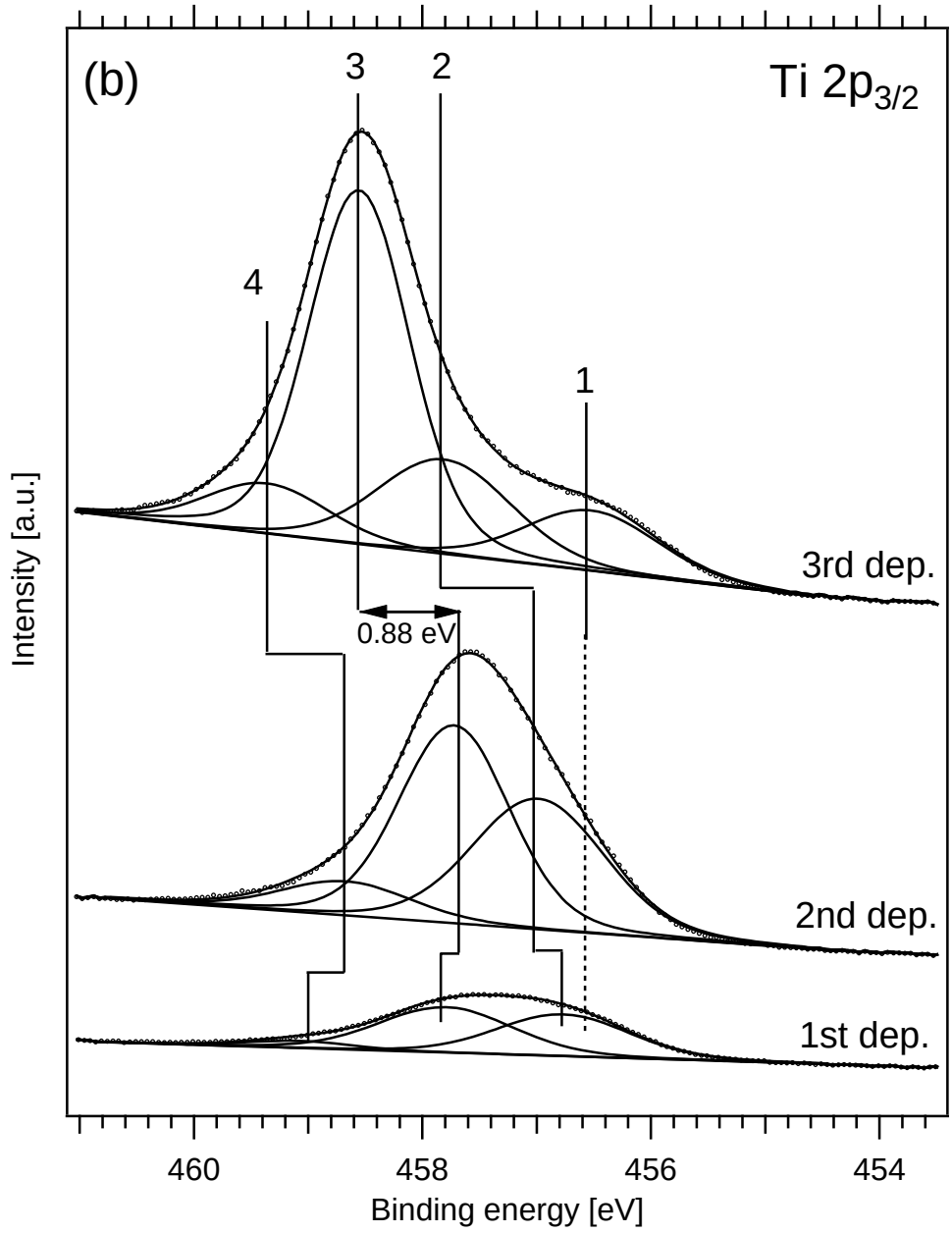

Figure 3b

L. E. Walle et al.

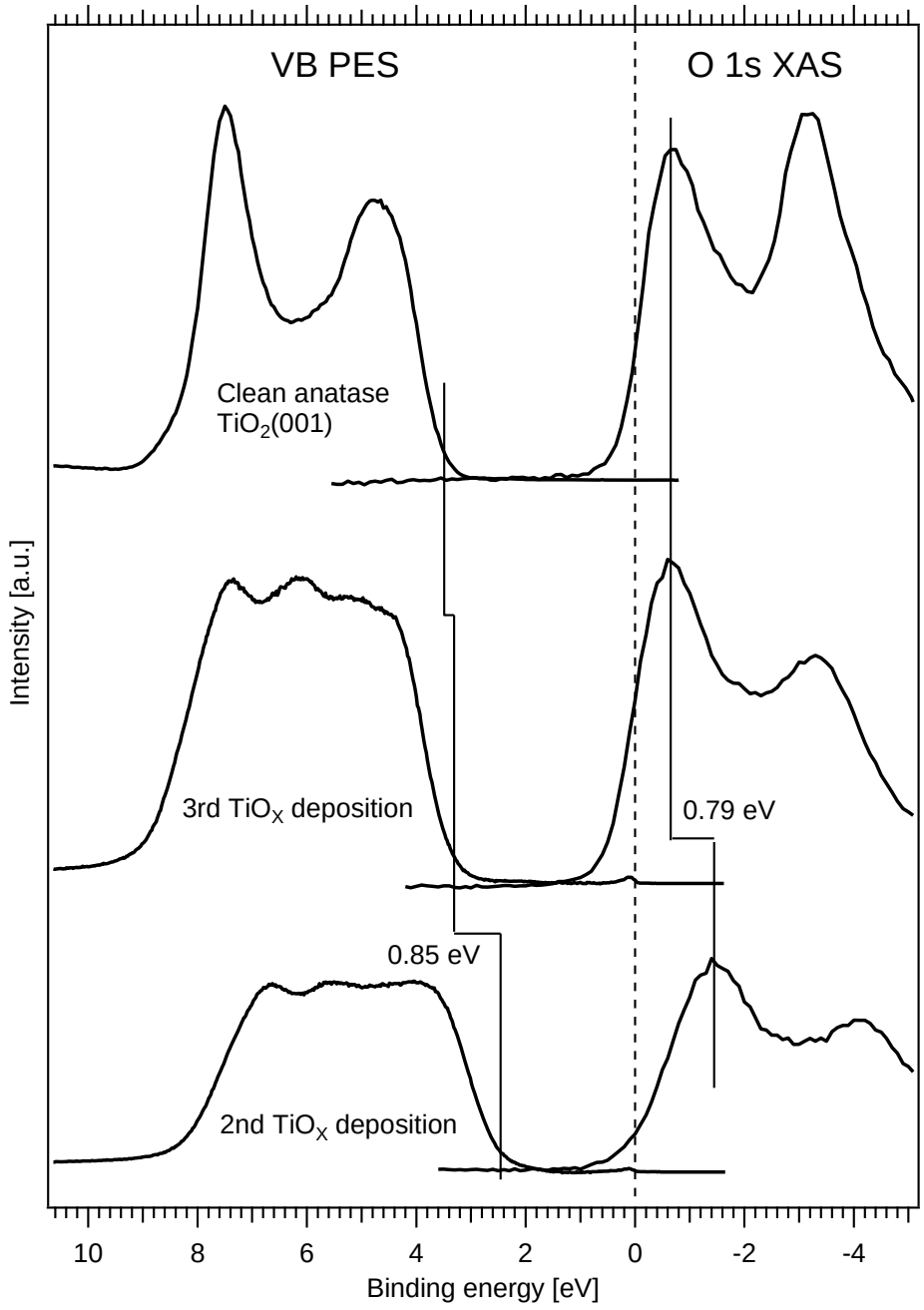

Figure 4

L. E. Walle et al.

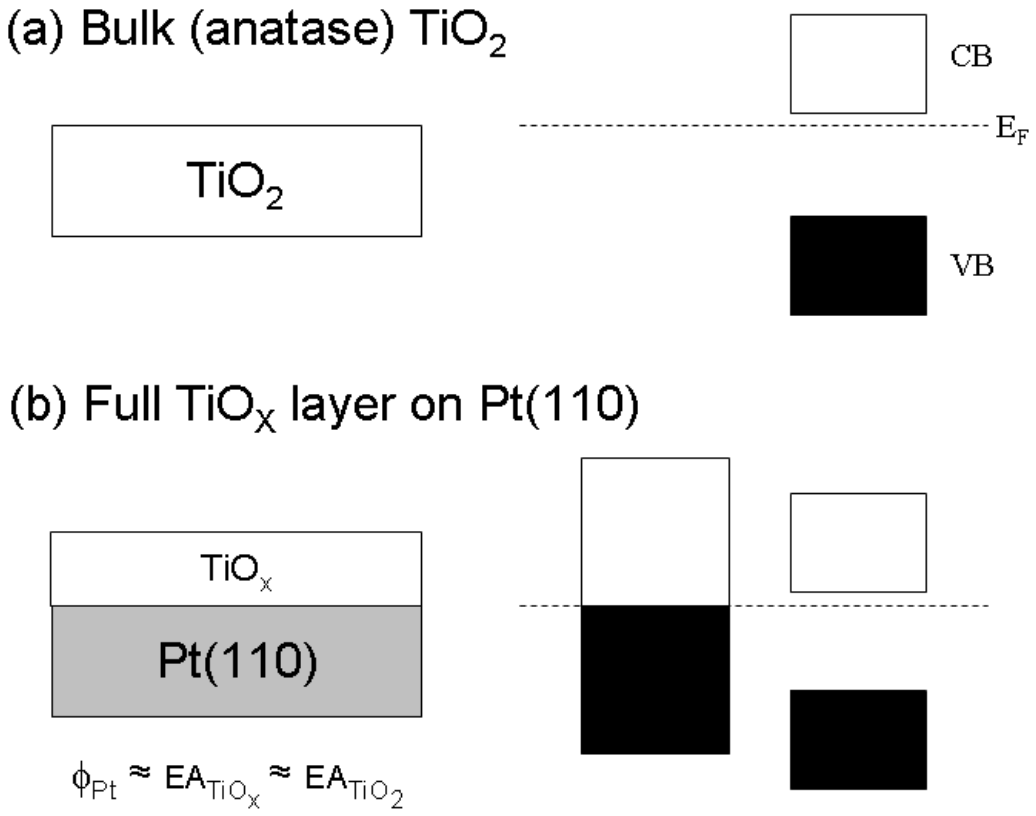

Figure 5

L. E. Walle et al.

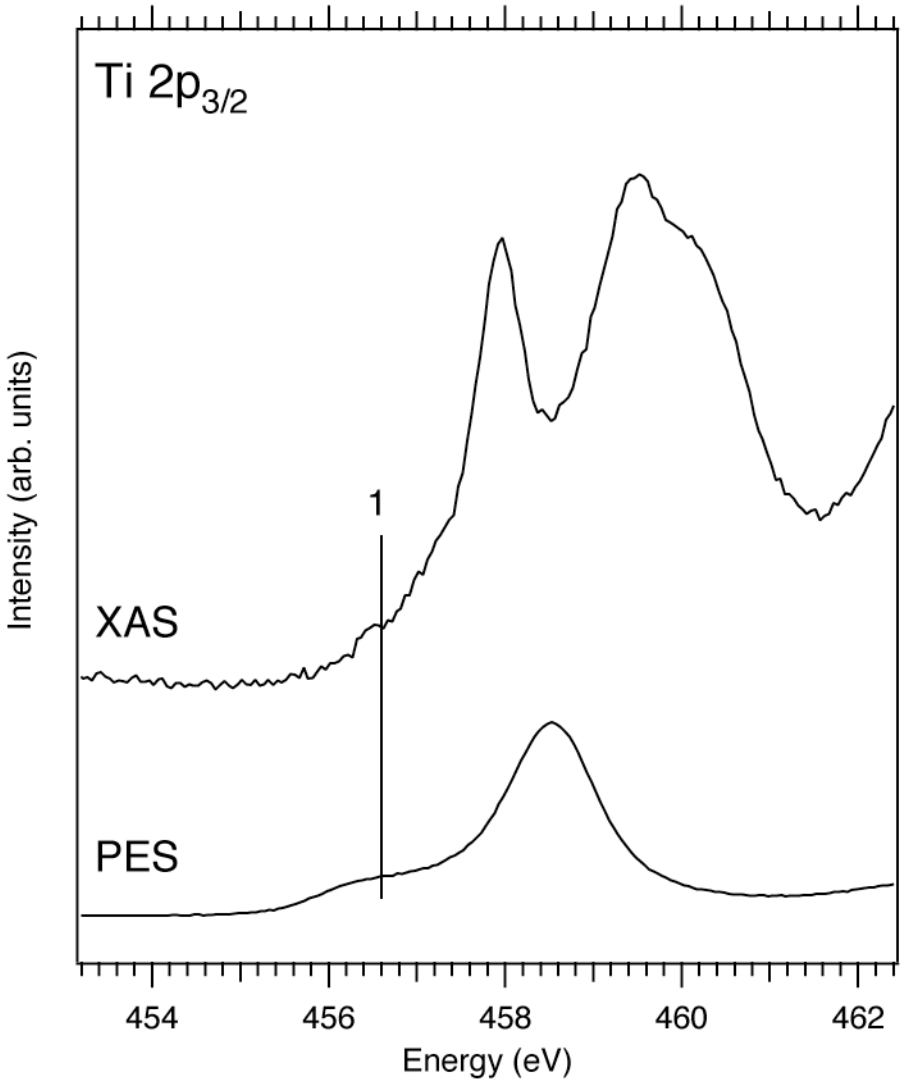

Figure 6

L. E. Walle et al.